PHOTODISSOCIATION DYNAMICS OF HALOGEN OXIDE SPECIES

A Dissertation

by

KRISTIN S. DOOLEY

Submitted to the Office of Graduate Studies of
Texas A&M University
in partial fulfillment of the requirements for the degree of

DOCTOR OF PHILOSOPHY

May 2009

Major Subject: Chemistry

PHOTODISSOCIATION DYNAMICS OF HALOGEN OXIDE SPECIES

A Dissertation

by

KRISTIN S. DOOLEY

Submitted to the Office of Graduate Studies of
Texas A&M University
in partial fulfillment of the requirements for the degree of

DOCTOR OF PHILOSOPHY

Approved by:

Chair of Committee,	Simon W. North
Committee Members,	Sarah Brooks
	Yi-Qin Gao
	David H. Russell
Head of Department,	David H. Russell

May 2009

Major Subject: Chemistry

ABSTRACT

Photodissociation Dynamics of Halogen Oxide Species. (May 2009)

Kristin S. Dooley, B.S., University of Central Arkansas

Chair of Advisory Committee: Dr. Simon W. North

The focus of this dissertation is the study of the photodissociation dynamics of halogen oxide species (XO, X = Cl, Br, I). These radical species are known to be important in stratospheric and tropospheric ozone depletion cycles. They are also useful benchmark systems for the comparison to current theoretical methods where they provide insight into the dynamics occurring beyond the Franck-Condon region. These systems are studied using velocity map ion imaging, a technique that measures velocity and angular information simultaneously. Photofragment species are state-selectively ionized for detection using 2+1 REMPI (Resonance Enhanced Multi-Photon Ionization). The instrumentation employs a molecular beam of the XO radicals formed using pyrolitic and photolytic methods.

The current work involves the measurement of fundamental physical constants of the XO species. The bond dissociation energy of IO is measured. Vibrational level dependent correlated final state branching ratios of the predissociation of the A($^2\Pi_{3/2}$) state of ClO and BrO are reported, and comparison to theoretical methods is discussed.

to Jenna,
my tireless sidekick throughout
the writing of this dissertation

AKNOWLEDGEMENTS

During my graduate career, there have been a number of people whose help, support, and encouragement have been invaluable to my successful completion of this degree. I will pause now to extend my gratitude to many of them.

I would like to start by thanking my advisor, Dr. Simon North for his leadership and guidance throughout this process. His patience as I found my place into the group and learned to produce worthwhile data is much appreciated. Thank you for all your help and advice during these years. You have a distinct talent for inspiring us to try experiments that we never would have dreamed we could accomplish. Thanks are also due to my dissertation committee members whose help and advice are much appreciated.

I cannot fail to mention all of the help I have received over the years from others within the chemistry department. These include the staff members of the glass, metal, and electronics shops. You are all essential to the research that is done in the chemistry department. Also, thank you to the staff in the chemistry graduate student office. You take as much of the complication out of graduate life as is possible. Special thanks are due to Monica who keeps our group running properly. I think we might fall apart without you.

To all of the group members that I have worked with over the years, thank you for all of the friendship and camaraderie you have provided. Getting to know each and every one of you was a blessing and I will always cherish the time we had in the lab together. Erin, you were a great senior student. You had tons of great advice about lab problems, classes, and graduate life in general. Thank you for everything. Kate and Andrea, I feel so fortunate to have had the chance over the past few years to have gotten to know you. We came to Texas A&M at the same time, and we are finishing together. It was a wonderful experience to share with you all the milestones in between. I wish you both the very best as we venture away from here. Buddhadeb, you are a brave soul to join a group of nearly all women. Good luck in your future endeavors.

I would especially like to thank the group members that have worked with me on the velocity-map ion-imaging project. Hahkjoon, you are a talented researcher, and I learned so much by working with you. Most importantly, you taught me to work hard and to often work very late. Justine, I had a blast working with you. We had lots of memorable lab moments like during the power outage and the time you "rolled on the counter" to get the experiment to work. Michael, I wish that we had more time to work together. You are great to work with and you have a ton of potential. I am sure you will have lots of success with the dynamics project in the future.

I have saved the most important thank you's for last. These go to my family. Each one of you has played a critical role in my success and in my survival of graduate school. Thank you for all of your love and encouragement. To Mom and Dad especially, you have played an important role in shaping me into the person I am today. You taught me by your example to put faith and family above everything else, and for that I am eternally grateful. I am so fortunate to have two wonderful families. I don't think it is especially common to find someone you want to marry that comes with a family that you love so much, too. Thank you for making me feel so welcome and loved. And, to Todd, you have had to deal with my day to day stress and frustrations for the past years. You have always listened to my gripes and complaints, keeping me somewhat sane, and you have also been there to celebrate all of the little victories leading up to this finale. My family in its entirety has been with me through all the uphill climbs in my life. A prime example of this is all the help in the form of babysitters I have had while I have worked to finish writing and defend in the last few months. I would not have made it through this experience without you. Thank you all for coming from miles away to help me. I love you all for each and everything that you do and for all that you mean to me. My words here can never be enough.

.

NOMENCLATURE

BBO	beta barium borate
CCD	charge coupled device
KD*P	Potassium Dihydrogen Phosphate
LAS	Laser Analytical Systems
MBL	Marine Boundary Layer
MCP	micro-channel plate
PDL	pulsed dye laser
PMT	photomultiplier tube
ppm	parts per million
ppt	parts per trillion
REMPI	Resonance Enhanced Multi-Photon Ionization
VELMI	Velocity Map Ion Imaging
WEX	Wavelength Extender

TABLE OF CONTENTS

CHAPTER Page

LIST OF FIGURES

FIGURE Page

FIGURE Page

FIGURE Page

LIST OF TABLES

CHAPTER I

INTRODUCTION

Halogen oxides (ClO, BrO, and IO) play an important role in the atmosphere where their photochemistry makes them key players in the chemistry of that region, most notably the chemistry surrounding ozone destruction in the stratosphere, but also in the troposphere and marine boundary layer (MBL). In order to fully understand and correctly model important chemistry in both the troposphere and stratosphere it is imperative to fully characterize the photochemistry and dynamics of the halogen oxide species. Because halogen oxide radicals are small open-shell species, they are also interesting on a purely fundamental level to the molecular dynamics community as they can be used as benchmark systems for the comparison of theory and experiment.

A. Atmospheric Relevance of Halogen Oxides

The structure and composition, and thus the chemistry, of the atmosphere change with increasing altitude. The temperature of the atmosphere as a function of altitude is a valuable parameter since the slope of its profile (shown in Figure 1) changes with increasing altitude. The regions of the atmosphere are most commonly defined by the altitude where this slope change occurs. The temperature generally decreases with increasing altitude in the troposphere due to the irradiative heating of the air by the earth's surface. Because warmer air rises due to its lower density, the warm air at the earth's surface rises causing a persistent vertical mixing to occur in the troposphere. This means that in a matter of a few days pollutants can move from the ground level to the tropopause-the region surrounding the temperature inversion that separates the troposphere from the stratosphere.

This dissertation follows the style of the Journal of Chemical Physics.

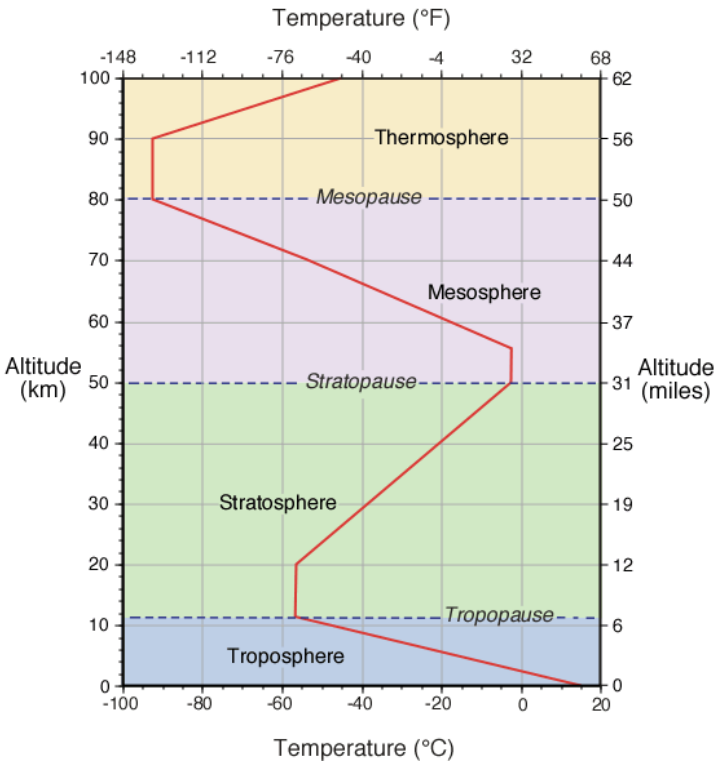

Figure 1: Temperature profile of the atmosphere as a function of height measured from the earth's surface. Regions of the atmosphere are labeled on the figure with approximate altitudes of the division of regions noted with horizontal lines.[1]

The temperature then begins to increase throughout the stratosphere from about -70ºC to -5ºC due to a series of photochemical reactions first hypothesized by Lord Chapman in 1930.[2] This cycle is shown below in Equations 1.1-1.4 involving ozone and molecular oxygen, and is commonly known as the "Chapman cycle."

$$O_2 + h\nu \rightarrow 2\ O, \qquad 1.1$$

$$O_2 + O + M \rightarrow O_3, \qquad 1.2$$

$$O + O_3 \rightarrow 2\ O_2, \qquad 1.3$$

$$O_3 + h\nu \rightarrow O + O_2, \qquad 1.4$$

Wavelengths of sunlight less than ~240 nm are absorbed by molecular oxygen in Equation 1.1. In Equation 1.4, wavelengths of light from 240 nm to 310 nm are

absorbed by ozone. Energy is then passed out of this cycle through a three-body collision in Equation 1.2 to other stratospheric molecules (M), transferring energy to M, thus causing the increase in temperature. Temperature is highest at the highest point in the stratosphere where the most light is absorbed. At lower altitudes, these wavelengths of light have been filtered out of the actinic flux decreasing the effect of these reactions on the observed temperature. This series could contribute to temperatures in other regions of the atmosphere, however at higher altitudes the pressures are too low for the effect of this cycle to be significant and in the troposphere where the pressures are adequate, the necessary wavelengths of light are absent as they have been filtered by the stratosphere.

The chemistry of the troposphere and the chemistry of the stratosphere are somewhat isolated from each other due to the temperature inversion occurring between them. The temperature inversion forms a kind of lid on the troposphere keeping tropospheric air and pollutants from mixing with the stratosphere. While stratospheric chemistry is dominated by chemical cycles surrounding ozone, in the troposphere, chemistry is influenced by the OH oxidation of hydrocarbons. Although halogen species are most commonly thought of as key players in stratospheric chemistry, they can actually also influence the chemistry in the troposphere, especially in the regions of the troposphere directly influenced by seawater known as the marine boundary layer (MBL).

The chemistry of the stratosphere is focused mainly around ozone. The Chapman cycle (Equations 1.1-4) is responsible for the ozone layer which is a region within the stratosphere where the concentration of ozone is at its maximum (from 2 to 8 ppm). This maximum in ozone concentration occurs due to a unique combination of atmospheric pressure and photon density. Here the pressure is sufficient for three-bodied collisions to take place allowing the reaction of atomic oxygen with molecular oxygen to form ozone (Equation 1.2) to occur at a high rate. There is also ample high frequency light at this altitude allowing the photolysis reaction of molecular oxygen via Equation 1.1 to occur. Because of the absorption of ozone, and the concentration of

ozone in this layer, most of the sunlight's shorter wavelengths are filtered preventing the formation of appreciable amounts of ozone by the Chapman cycle at lower altitudes.

The stability of the ozone layer is crucial to life on earth as we know it. Ozone is the only molecule of considerable abundance in earth's atmosphere that has a significant absorption in the UV region. The absorption spectrum of ozone is shown in Figure 2.[3] There are three main sections of the ozone absorption spectrum: the Hartley bands[4,5] in the UV region ($200 < \lambda < 300$ nm), the Huggins bands[6] in the visible region ($300 < \lambda < 360$ nm), and the Chappuis bands[7] that span the visible and infrared regions ($440 < \lambda < 850$ nm). As can be seen in Figure 2, the Hartley bands absorb UV-C and UV-B light keeping it from reaching the troposphere. These wavelengths are destructive to plants, known to damage DNA, and cause malignant skin cancer and eye damage in humans. Figure 3 shows how the intensity of the sun's radiation as a function of wavelength hitting the earth's surface is affected by the presence of the ozone layer. As can be seen from the figure, the ozone layer in the stratosphere protects us from a significant amount of this harmful light. It is for this reason that the fate of the ozone layer and the chemistry surrounding ozone continues to remain a topic of much interest as it must be protected in order to preserve the current state of the planet.

Ozone remains in equilibrium with molecular and atomic oxygen due to the Chapman cycle; however, there is a large discrepancy between the ozone concentration predicted using only the Chapman cycle and the notably lower measured ozone concentration in the stratosphere. Other chemical species, both naturally occurring and man-made, can interrupt this equilibrium and change the steady state concentration of ozone. There has been a significant amount of work done to identify these species and understand their effect on this discrepancy.

One such disruption that depletes ozone occurs by the following catalytic cycle first proposed by Crutzen in 1970:[8]

$$NO + O_3 \rightarrow NO_2 + O_2, \qquad 1.5$$

$$NO_2 + h\nu \rightarrow NO + O, \qquad 1.6$$

$$NO_2 + O \rightarrow NO + O_2. \qquad 1.7$$

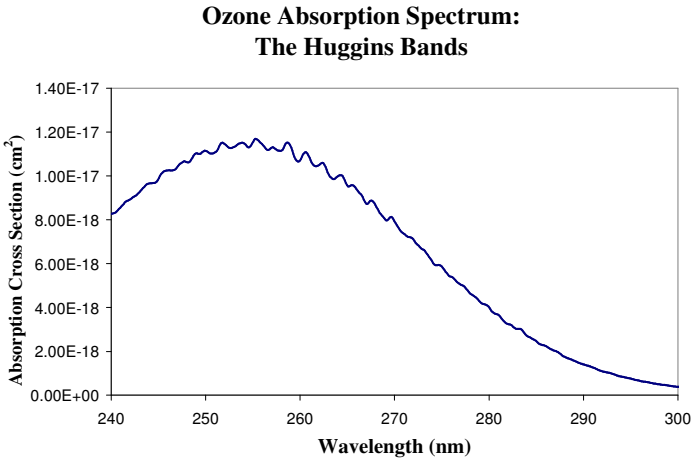

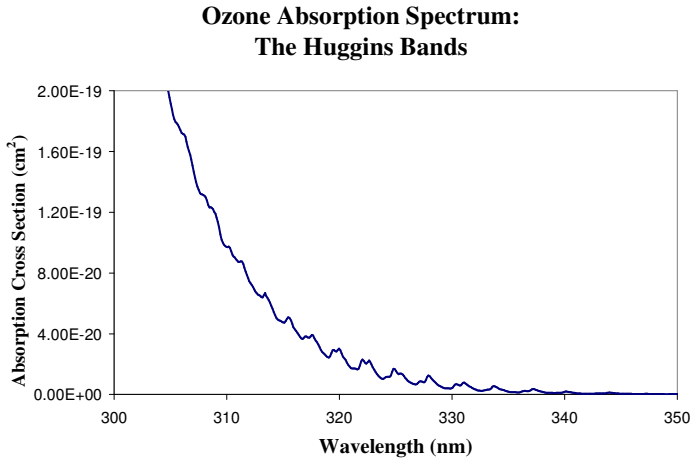

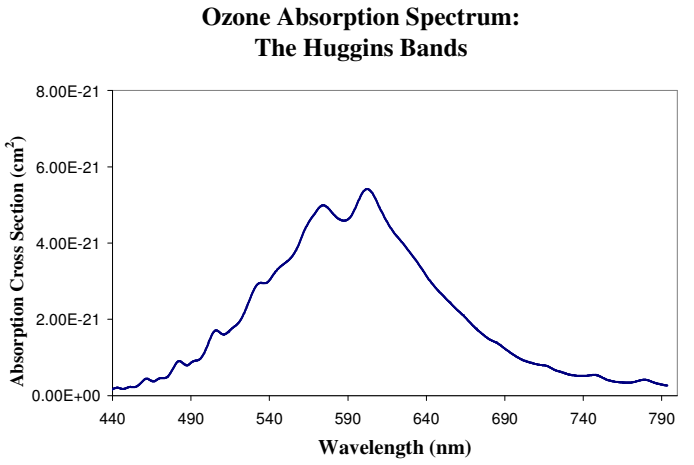

Figure 2: Absorption spectrum of ozone, adapted from Burrows *et al.*[3]

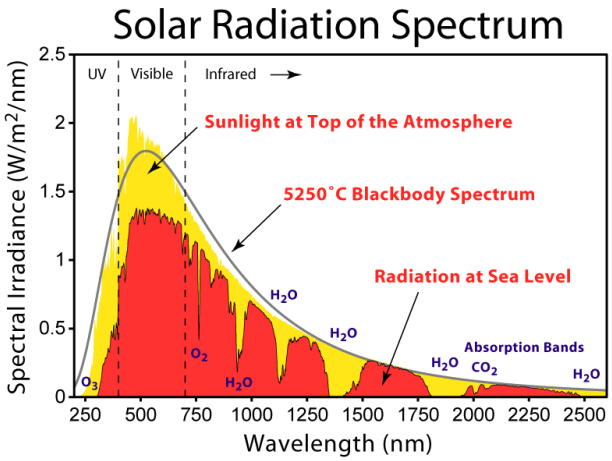

Figure 3: Solar radiation spectrum shown as spectral irradiance (W/m^2) vs. wavelength (nm). The plot shows the calculated irradiance based on a blackbody at 5250 ºC, the actual spectrum of the sun's irradiance (yellow) and the sun's radiation that reaches the earth's surface which shows the effects of absorbing species such as ozone in the atmosphere.[9]

NO can be formed in the stratosphere from reactions of N_2O which is formed at the earth's surface from biological processes but is unreactive in the troposphere. Because of its sufficiently long lifetime, it can travel into the stratosphere where it will be photolyzed via the following reaction[10]:

$$N_2O + h\nu \rightarrow N_2 + O(^1D) \qquad 1.8a$$

$$\rightarrow NO + N(^4S) \qquad 1.8b$$

The quantum yield of Equation 1.8b was studied by Bates and Hays in 1967 and determined to be about 20% which makes this natural source of ozone depletion quite significant. However, this result was later revisited by Greenblatt and Ravishankara in 1990 and determined to be no larger than a modest 1%.[11] Nevertheless, naturally occurring N_2O is still the major source of nitrogen oxide compounds in the stratosphere through via reaction of N_2O with electronically excited atomic oxygen produced when ozone or molecular oxygen photodissociates[12, 13]:

$$N_2O + O(^1D) \rightarrow N_2 + O_2 \qquad 1.9a$$

$$\rightarrow 2\ NO \qquad 1.9b$$

Although natural sources of NO_x are not significant sources of stratospheric ozone depletion, concern was raised that NO_x was being emitted directly into the stratosphere from supersonic transport aircraft (SST).[14] Although this problem was averted in the 1970's as the number of SST's produced and flown were far fewer than expected, this issue has reemerged into the forefront as the possible use of high-speed civil transport (HSCT) aircraft is debated.

Halogens as a source of ozone loss in the stratosphere was first suggested in 1974 by Cicerone and Stolarski.[15] They proposed that if atomic chlorine was present in the stratosphere, it could participate in a catalytic ozone destruction cycle:

$$Cl + O_3 \rightarrow ClO + O_2 \qquad 1.10$$

$$ClO + O \rightarrow Cl + O_2 \qquad 1.11$$

$$\text{Net: } O_3 + O \rightarrow 2\ O_2 \qquad 1.12$$

Other radical species such as Br, I, NO, and OH can replace Cl in this cycle.

Shortly after the mechanism shown in equations 1.10-1.12 was proposed, Molina and Rowland predicted that because of their stability, chlorofluorocarbons (CFC's) should be expected to reach the stratosphere. CFC's were commonly used for purposes such as refrigeration and computer chip production where their low reactivity makes them highly advantageous. Unfortunately, it is this low reactivity that allows them to escape removal in the troposphere. Instead, CFC's dissociate upon absorption of UV radiation leading to the formation of chlorine atoms in the stratosphere. Similarly, halons, molecules like CFC's but also containing bromine, which were used primarily as fire retardants, can releasing atomic bromine into the stratosphere through photodissociation. Because of the obvious correlation of CFC and halon use and ozone concentration decrease, international regulations such as the Montreal Protocol have phased out the use of these molecules. Despite these efforts by the global community, the damage caused by past use of halogen containing compounds will continue due to their extremely long lifetime on the order of decades. According to a study published by the World Meteorological Society in 1995, the chlorine concentrations in the stratosphere peaked around 1997, and, with the current regulations of CFC use in place,

should return to levels seen in 1980 (the concentration level at which ozone depletion due to chlorine became detectable) in the year 2050.[16]

It is currently estimated that more than 85% of the chlorine in the stratosphere is from anthropogenic sources. Other sources of chlorine include the release of methyl chloride by oceans and biomass burning. Besides halons which make up about 40% of the stratospheric bromine budget, 55% of this budget is the result of the other major source of bromine, methyl bromide, which is produced in modest amounts by biological activity but is also heavily used in agriculture as a soil fumigant. Iodine can also participate in catalytic ozone destruction. The most abundant source of stratospheric iodine is naturally occurring methyl iodide.

Once the atomic halogen species enter the stratosphere, they participate in a number of reactions forming reactive intermediate species and reservoir species. These reactions form an intricate web of species with the catalytic ozone destruction reactions proposed by Cicerone and Stolarski in equations 1.10 to 1.12 as the central focus.[15] A simplified halogen reaction cycle is shown in Figure 4 where X represents the halogen species. The catalytic ozone destruction cycle is terminated when the radical intermediate species X and XO react to form relatively stable species via three reactions:

$$X + X \rightarrow X_2 \qquad 1.13$$

$$X + CH_4 \rightarrow HX + CH_3 \qquad 1.14$$

$$XO + NO_2 \rightarrow XONO_2 \qquad 1.15$$

The stability of these halogen reservoir species is just as important as the overall concentration in determining the significance of a particular halogen species in ozone destruction. For example, the total bromine concentration in the stratosphere is on the order of 100 times less than the total chlorine concentration. However because the chlorine reservoir species are much more stable than their bromine counterparts, on a per atom basis, bromine is 100 times more efficient at ozone destruction. This means that chlorine and bromine are roughly equally important factors in ozone destruction despite the lower concentration of bromine. The approximate lifetimes of the relevant reservoir

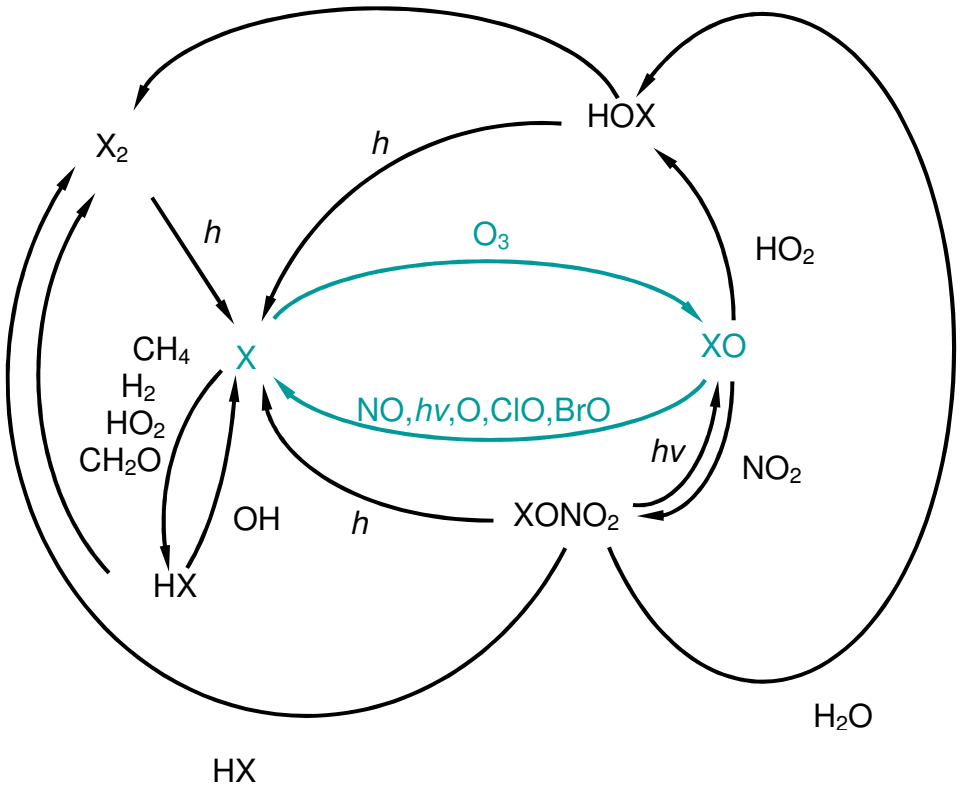

Figure 4: Stratospheric halogen cycle.

species influence the mixing ratios of the halogen atoms, intermediates, and reservoir species as is evident from Figures 5 and 6. Figure 5 shows the mixing ratios of chlorine containing species in the stratosphere. Although the total chlorine mixing ratio is relatively constant throughout the stratosphere, at 3.8 ppbv, the profiles of the individual species change dramatically as a function of altitude. HCl remains the most abundant chlorine species throughout nearly the entire stratosphere as a result of its long lifetime. The total mixing ratio of bromine is 25-30 pptv.[17, 18, 19, 20] Figure 6 shows the altitude profile of the most important bromine species.

Because the lifetime of HBr is much shorter than HCl, HBr is not the most abundant bromine containing species in the stratosphere. In fact, because of the short lifetimes of all bromine reservoir species, the most abundant stratospheric bromine species are atomic bromine and BrO, both active players in the ozone destruction mechanism.

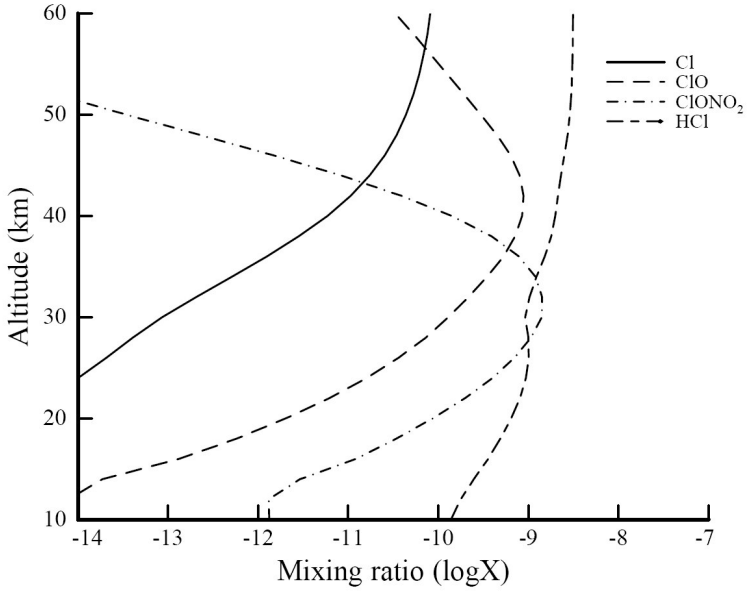

Figure 5: Altitude profile of chlorine containing species in the stratosphere.

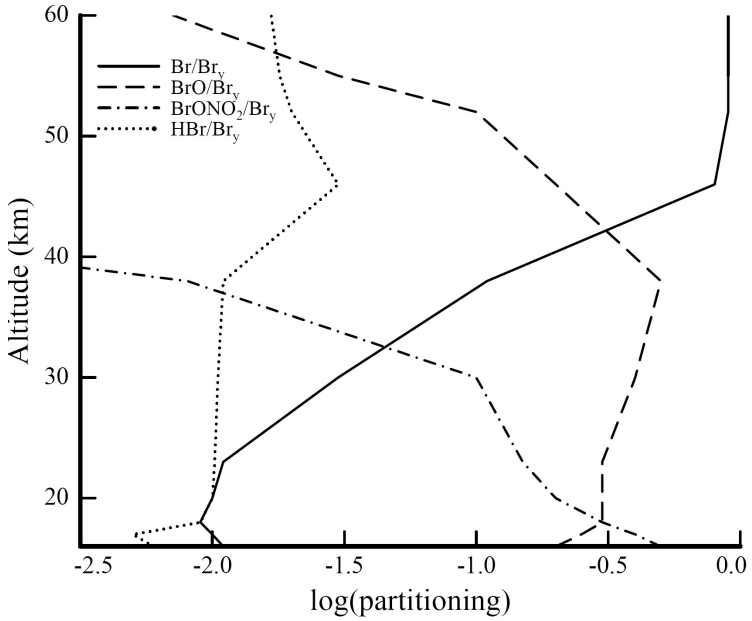

Figure 6: Altitude profile of bromine containing species in the stratosphere.

Fluorine is also present in the stratosphere and can also participate in catalytic ozone destruction. However, because HF is extremely stable with respect to possible reaction pathways shown in Figure 4, fluorine is only a minor contributor to ozone depletion. Conversely, due to the instability and short lifetime of its reservoir species, iodine is more efficient at ozone destruction than bromine or chlorine despite its lower concentration of 0.2 pptv.[21] However, the major sources of iodine (CH_3I and CH_2I_2) are rapidly photolyzed in the troposphere and are then removed from the gas phase by moisture. Because of this, the concentration of iodine is much less than that of chlorine or bromine. It was once thought that because of its low concentration that its contribution like that of fluorine was negligible; however, due to the brief lifetime of HI and other reservoir species, and the interaction of IO in the Br and Cl cycles, Solomon *et al.* propose that iodine could make a major contribution to ozone destruction below about 20 km at a total species concentration of just 1 ppt.[22] A study by Wennberg *et al.*

concluded that the total stratospheric iodine concentration is about 0.2 ppt with an upper limit of 0.3 ppt.[21] Pundt *et al.* also concluded that at altitudes less than 20 km, the iodine concentration is below 0.2 ppt.[23] While this limits the importance of iodine in stratospheric ozone destruction, there are strong meteorological events that can directly introduce troposheric air directly into the stratosphere. This type of event could force a large amount of iodine containing species into the stratosphere before they react in the troposphere. For example, Davis *et al.* observed concentrations of CH_3I of 1 ppt at an altitude of 10-12 km following a typhoon.[24]

Because iodine containing organic species decompose in the troposphere, understanding the tropospheric photodissociation and reaction pathways of iodine containing molecules in this region is important. As mentioned earlier, methyl iodide (CH_3I) is the major source of iodine in the atmosphere, although there are other iodine containing species such as CH_2I_2, $ClCH_2I$, and CH_2IBr. These species occur naturally from biological processes in the ocean. Therefore, iodine chemistry plays an important role especially in the marine boundary layer (MBL). Methyl bromide and methyl chloride are also formed in marine areas, but only methyl iodide is photolyzed by wavelengths of light that reach the troposphere and produce atomic iodine. The iodine atoms react with tropospheric ozone via the same reaction that occurs in the stratosphere shown in Equation 1.10 producing IO. The concentration of IO in a coastal site was directly detected and measured at concentrations up to 6 ppt.[25] IO can oxidize dimethyl sulfide (DMS) to form dimethyl sulfoxide (DMSO), regenerating the iodine atom:

$$IO + CH_3SCH_3 \rightarrow I + CH_3S(O)CH_3 \qquad 1.16$$

It is also known to seed formation of small aerosol particles in the tropospohere.

In summary, halogen oxide species play important roles in both the stratosphere and troposphere where they undergo chemical and photolysis reactions. Understanding the photochemistry and fundamental constants of these molecules, such as the bond dissociation energies, are useful towards further understanding the roles of these species in atmospheric chemistry.

B. The Relevance of Halogen Oxides Studies in Physical Chemistry

When studying the photodissociation of a species, the principle goal is to fully understand and characterize its dynamics as it moves out of the Franck-Condon region, through a barrier if there is one, and into the resulting asymptotic channels.[26] For diatomic species such as those which are the focus of this dissertation, there are a number of questions that molecular dynamics attempts to answer when studying a photodissociation event. Some of these are:

- What are the quantum states of the reactant species and the product fragments?
- Given a quantum state of the reactant species, what are the branching ratios for possible dissociation channels?
- What is the lifetime of the excited molecule before it dissociates?
- What is the dissociation energy of the diatomic molecule? Subsequently, after dissociation, how is the remainder of the energy distributed among the translational and electronic energies of the fragments?
- Does the dissociation occur via one potential, or does the excited state couple to numerous dissociative potentials?
- Do the dissociative potentials couple in the exit channel?

Although this list is not exhaustive, it serves as an example of the types of inquiries made to form a full understanding of a photodissociation event. The velocity map ion imaging technique described in this dissertation is a useful tool for answering or providing unique insight into these questions. The field of photodissociation dynamics has grown immensely since the advent of tunable lasers in 1966 that allow experimentalists to vary the dissociation wavelength providing them with the ability to investigate the wavelength dependence of the measurement.[27, 28] Lasers also open up many useful avenues for detection of the photofragments using techniques that are electronic state selective.[26, 29, 30, 31, 32]

Photodissociation dynamics is a subject that permeates many fields of chemistry such as environmental chemistry, quantum scattering theory, and gas-surface chemistry.[29] For example, the branching ratio of the electronic state of the oxygen

fragment is very important to the chemistry of the troposphere. The oxygen atoms in the ^1D electronic state are the major sources of OH in the troposphere.[33] Experimental photodissociation dynamics also provide insight into the validity of assumptions made in computational methods. For example, transition state theory which is used to calculate the rates of chemical reactions works under the fundamental assumptions that the nuclear and electronic components of the eigenfunctions of a molecule are separable and that there is a rapid redistribution of vibrational energy.[29] The experimental study of the photodissociation dynamics of systems can be compared to computational results to help assess the validity of these assumptions.

In addition to being atmospherically relevant, halogen monoxide species are interesting systems on a fundamental level. These species are excellent benchmark systems for comparing theoretical models to experimental numbers. Being diatomic, halogen monoxide species are able to be fully studied using current theory. Nevertheless, they are challenging for theorists to study, as the halogen species possesses large spin-orbit coupling, and the bound potentials are crossed by a number of repulsive states. Comparison of calculated values to good experimental measurements aids in our understanding of current theoretical models and their ability to correctly predict molecular dynamics.

The spectroscopy of halogen oxide molecules has been studied extensively. The spectra were investigated for their insight into fundamental physical properties long before they were thought of as environmental participants. The absorption spectra of the halogen oxides are qualitatively quite similar with sharp structural features below the dissociation threshold resulting from predissociation of the bound excited state followed by a broad feature beginning at the excited state dissociation threshold and continuing to lower wavelengths. Figure 7 shows plots of the absorption spectra of ClO (a), BrO (b), and IO (c).[34, 35, 36] Although the overall shapes of the spectra are similar, they show major differences as well. For example, in the ClO spectrum, bandhead data from predissociation of vibrational levels are visible extending to $v' = 0$. This allows accurate measurement from only spectroscopic methods of the bond dissociation energy of ClO

using common Birge-Sponer extrapolation methods.[37] The absorption cross sections of BrO diminish as the $v' = 0$ band is approached requiring the use of approximation techniques such as the Birge-Sponer method. An extrapolation becomes quite impossible with IO as only a few vibrational bands can be seen in the spectrum. Very accurate measurements of the bond dissociation energies of these molecules are important when determining the thermodynamics of reactions involving the halogen oxides. There are a number of atmospherically relevant reactions involving BrO or IO that are near thermoneutral. Therefore, accurate measurements of the bond dissociation energies of these radicals (uncertainties of less than a kilocalorie) are necessary for accurate atmospheric modeling.

Photodissociation and predissociation of a diatomic molecule involve the absorption of a photon of light followed by the fragmentation of the molecule into two atoms. Photodissociation in combination with a large barrier to recombination is explained by the impulsive model which assumes that after the photon is absorbed the molecule's bond breaks before a statistical redistribution of the energy has time to occur.[38] During photodissociation, the molecule absorbs a photon of light raising it above the dissociation threshold of its potential into the continuum. Predissociation can occur when the photon of light absorbed is not energetic enough to reach the dissociation threshold. Instead, the molecule is raised to a vibrational level within a bound excited state of the molecule. If the bound excited state is crossed by a repulsive state, the molecule can cross to this curve and dissociate. The halogen oxide species are extremely interesting with respect to predissociation. The diatomic radicals have numerous repulsive potentials that cross the lowest bound excited state. In independent theoretical papers by Orr-Ewing and coworkers and Persico and coworkers, ClO was studied and seen to have 17 repulsive potentials that were capable of predissociating the $A\ ^2\Pi$ state.[39, 40] BrO and IO are also heavily predissociated with very similar potential energy surfaces to that of ClO.

Because they have numerous repulsive potentials and readily predissociate, these molecules are very interesting to the field of molecular dynamics. The spectroscopy of

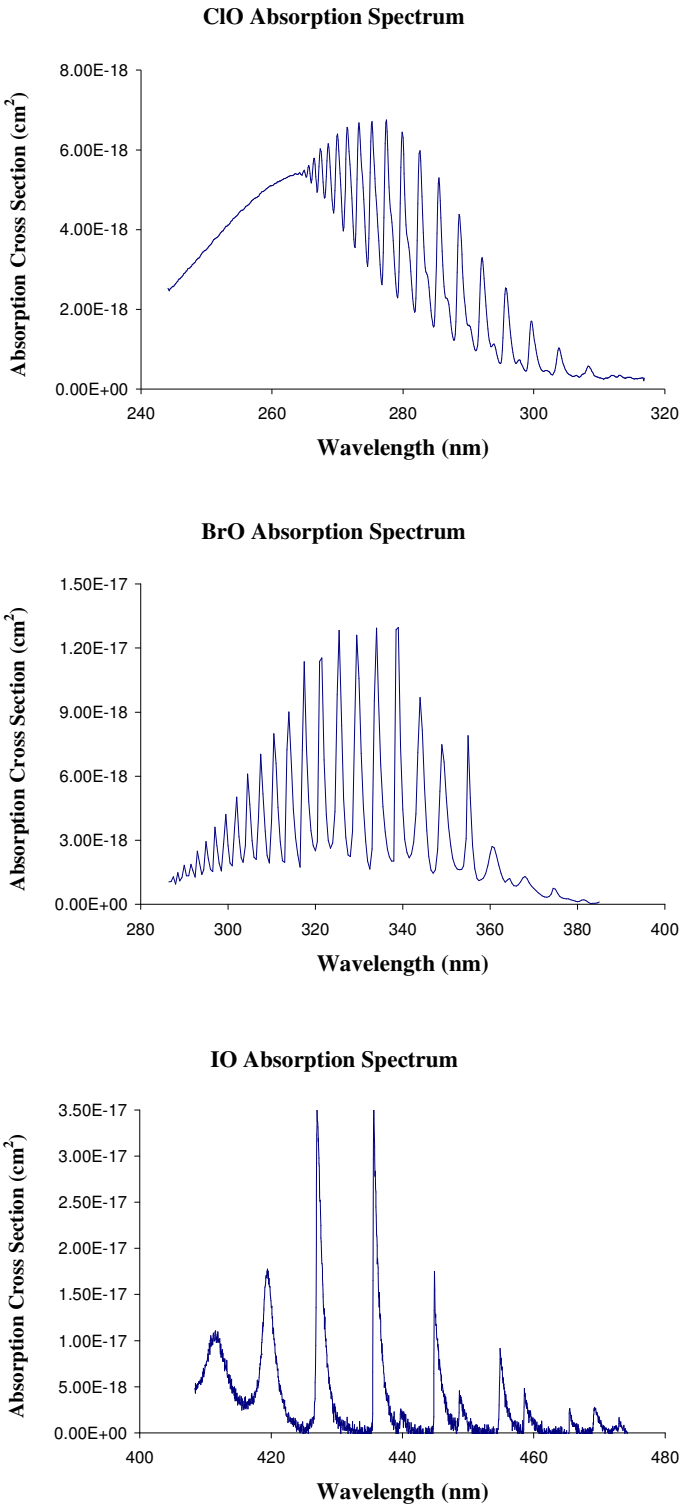

Figure 7: Absorption spectra of halogen oxide species ClO, BrO, and IO, Panels (a), (b), and (c), respectively. Data shown in this figure are the results of References 34, 35, 36.

the XO molecules, especially the ClO molecule, gives insight into the coupling of the repulsive states to the bound excited state. Which states couple, as well as how strongly the states are coupled, can be determined for these molecules from first principles. This information can then be used to calculate the predissociation lifetimes of each state using Fermi's golden rule calculations as was done by Orr-Ewing and coworkers.[39]

From a molecular dynamics standpoint, the halogen oxide systems are extremely important to consider. While measuring the spectroscopy of the halogen oxide molecule provides some insight to the couplings of the potentials in the system within the Franck-Condon region, spectroscopy cannot detect dynamics occurring in the exit channel. Fully correlated final state branching ratios of the systems provide the information that spectroscopy is lacking. The branching can be predicted by using one of two models to explain the transition occurring at a curve crossing. The adiabatic model assumes that the process (in our case the predissociation of the $A(^2\Pi_{3/2})$ state) occurs sufficiently slowly to allow the bound state eigenfunction to change very gradually into an eigenfunction of the unbound state. In this model, the Born-Oppenheimer approximation is assumed, as the nuclear motion must be gradual enough so that the electronic motion can slowly adapt. However, if the molecule experiences a rapid nuclear change, a breakdown of the Born-Oppenheimer approximation may occur. In this instance, the dynamics are described using a diabatic (or non-adiabatic) model. This model is often termed the "sudden" model as the nuclear motion occurs very quickly, not allowing the electronic motion to adapt to the changing nuclear conditions. If this occurs, the electronic structure will not change to an eigenfunction of the final state, instead, a linear combination of initial eigenstates will be seen that add to form the initial probability density.

In the specific case of predissociation, the adiabatic model indicates that as predissociation occurs the electronic eigenstate of the molecule gradually changes to become an eigenstate corresponding to fragments in specific electronic states. Conversely, in the diabatic limit, the fragments produced will be a combination of final states that sum to the initial eigenstate of the bound species. For the case of the

predissociation of a halogen oxide radical species, XO, there are six possible final state outcomes corresponding to three possible states of O, $O(^3P_{J=2,\,1,\,0})$ in correlation with two possible states of X, $X(^2P_{3/2,\,1/2})$. In the adiabatic limit, the eigenstate of the XO species will be allowed to gradually evolve in to an unbound state corresponding to only one of the six possible combinations of $O(^3P_J) + X(^2P_J)$. So, for each dissociative curve that couples to the bound $A(^2\Pi_{3/2})$ state of XO, only one final state of $O(^3P_J) + X(^2P_J)$ will be observed. In the diabatic limit, a linear combination of the six possible final states will occur which would form the eigenstate of the initial XO species. In this case, each dissociative state to which the $A(^2\Pi_{3/2})$ state couples will result in the observation of multiple final states.

C. Advantages and History of Velocity Map Ion Imaging

Photodissociation dynamics is a young field that has grown explosively in the last few decades as experimental methods have begun to advance. As mentioned earlier, much of the advancement can be attributed to the development of tunable lasers.[26, 29, 30, 31, 32] This allowed for new techniques to be developed that allow the user to better characterize the reactant molecule and the product fragments. One such technique is Velocity Map Ion Imaging, which is used in all of the experiments described in this dissertation.

Ion imaging was pioneered by Chandler and Houston in 1987 when they combined a molecular beam time of flight instrument with a position sensitive detector consisting of an MCP/phosphor screen assembly to detect the entire ion cloud produced after the photodissociation of CH_3I.[41] This method was modified by Eppink and Parker who replaced the ion optic meshes which disrupted the ion cloud with an Einzel lens assembly.[42] With this advancement, velocity map ion imaging was originated.

The instrument allows for the detection of the entire ion cloud providing speed as well as angular information with a single measurement. Using this method, it is possible to excite parent molecules to a well-defined internal energy while also detecting the quantum states of the fragments produced. The quantities measured can be described as

scalar or vector quantities. Examples of scalar quantities include the bond dissociation energy of the parent molecule and correlated fine structure branching ratios. Examples of vector quantities include the angular distribution of the fragments providing information about the dissociation process.

D: Introduction to Subsequent Chapters

Understanding photodissociation of halogen oxides is key to understanding the chemistry of the stratosphere and to a lesser degree the troposphere. These molecules are also useful benchmark species to study in order to better understand the fundamental physical behaviors of molecules. They are small enough to be easily studied, but complex enough to be a challenge to theory making them perfect benchmark systems for a better understanding of molecular dynamics. The photodissociation dynamics of the ClO, BrO, and IO species are the central focus of this dissertation. The following chapters will detail the studies done in this work on the halogen oxide radicals.

Experimental details surrounding the velocity map ion imaging instrument used in these studies are provided in Chapter II. Information about the instrument was included in much detail in a previous dissertation[43], and will be more briefly described here. Some improvements and modifications to the original instrument and setup will be explained in more detail. In particular new data collection software and ion optics have been installed. Data analysis using pBASEX as well as BASEX methods are discussed and compared. Radical beam sources used in the production of ClO, BrO, and IO molecular beams are explained. The ClO and BrO sources were described in detail elsewhere and will only be briefly explained here. The photolytic radical source used in producing the IO molecular beam will be described in detail including kinetic simulations used to characterize the source.

In Chapter III, we examine the photodissociation dynamics of expansion-cooled IO at 454.9 nm corresponding to the band head of the v'=1 level of the $A(^2\Pi_{3/2}) \leftarrow X(^2\Pi_{3/2})$. This is the first study to look at IO in a molecular beam. In this experiment, we present a direct measurement of the bond dissociation energy of the IO radical. This

is accomplished by analyzing the speed distributions derived from images of the $I(^2P_{3/2})$ photofragment.

In Chapter IV we study the v'-dependent photodissociation dynamics of the ClO $A(^2\Pi_{3/2})$ state. Experimental final correlated state branching ratios, i.e. $Cl(^2P_J) + O(^3P_J)$ channels, have been measured for v'= 0-6, extending a previous study that focused on the measurement of the v'=6-11 branching ratios. The branching ratios are found to be highly v'-dependent and are non-statistical and inconsistent with adiabatic dissociation dynamics. Using previously reported v'-dependent predissociation rates, the coupling constants between the A $^2\Pi_{3/2}$ state and several dissociative excited state potentials have been optimized, as have the locations of the crossing points. Using the optimized potentials and coupling constants, the branching ratios have been modeled using the diabatic and adiabatic limits. The modeled results are compared to the measured branching ratios and similarities and differences are discussed.

Chapter V is similar in content to Chapter IV. Its focus is the photodissociation dynamics of the $A(^2\Pi_{3/2})$ state of BrO. In this study, the v'-dependent correlated fine structure branching ratios of the $A(^2\Pi_{3/2})$ predissociation for v'=4-18 are measured. The BrO system is thought to be more adiabatic than the ClO system based on the larger spin orbit coupling of bromine which makes it an interesting model for exploring the photodissociation dynamics. Because most of the vibrational bands of the BrO absorption are rotationally unresolved, anisotropy parameter measurements are used to determine predissociation lifetimes for some of the vibrational levels of the $A(^2\Pi_{3/2})$. A bond dissociation energy of BrO was recently measured using velocity map ion imaging. Using the extensive amount of data collected here, we provide a second look at this measurement.

Finally, we end with a Summary in Chapter VI which explores the significance of this work to the molecular dynamics and atmospheric communities. Insight into the significance of the work presented here will be discussed. A look toward future experimental directions will also be addressed.

CHAPTER II
EXPERIMENTAL DETAILS

A. Ion Imaging Apparatus

The velocity map ion imaging system employed in the studies described in this dissertation is based on the work of Chandler and Houston and Eppink and Parker described in the Introduction.[41, 42] The instrument consists of a stainless steel differentially pumped vacuum chamber with a position sensitive detector assembly. The cross-sectional view of the vacuum chamber is shown in Figure 8.

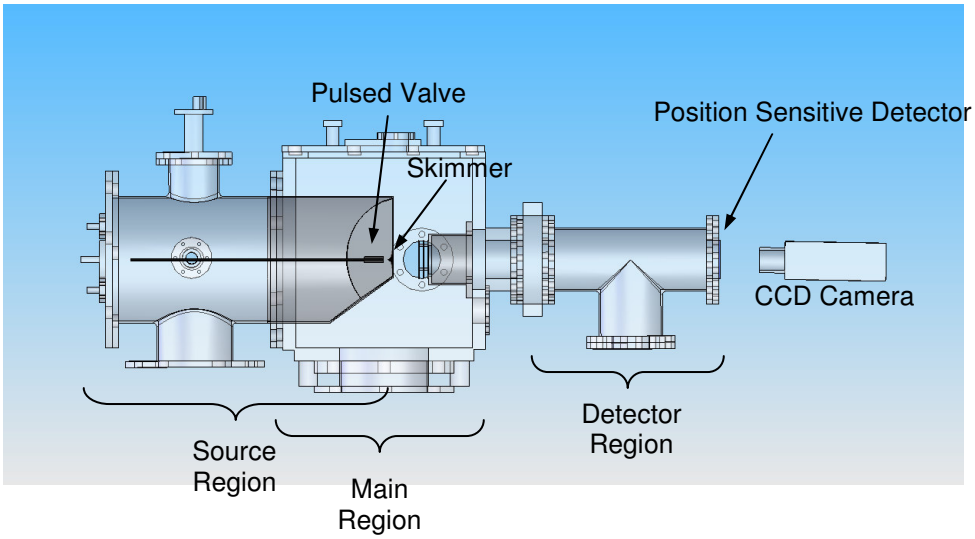

Figure 8: Cross-sectional view of the velocity map ion imaging vacuum chamber described in the text.

It is a differentially pumped vacuum chamber comprised of three regions. The source region is where gas samples are introduced into the chamber using a solenoid pulsed valve (Series 9, Parker Hannifin) or, for the radical beams studied in this work, custom-built pulsed valve assemblies that will be described in full detail in Sections I, J,

and K of this chapter. The gas sample undergoes a free jet expansion into the source region where it is collimated by a stainless steel conical skimmer with an orifice diameter of 0.8 mm into the main chamber region. The main chamber region houses the ion optics used for expanding and focusing the photofragment ion spheres and accelerating them onto the detector. The photodissociation of the molecules and subsequent ionization of the fragment of interest occur via laser beams focused between the first and second ion optic located in this region. The detector region is separated from the main region by a gate valve and consists of a field free time of flight tube which allows for the expansion of the ion cloud as well as mass separation. At the end of the flight tube is the MCP plate/phosphor screen position sensitive detector assembly.

The source and main chamber regions are differentially pumped using 6 inch diffusion pumps (Varian) backed by Welch 1410 mechanical pumps. The detector region is pumped using a turbo pump to avoid oil contamination of the MCP plates. The mechanical gate valve between the main and detector regions allows the detector region to remain under vacuum at all times providing protection to the detector, while the source and main chamber are only pumped down when during the experiment. Typical pressures in the regions are 9×10^{-7} torr for the source region, 5×10^{-7} torr for the main region, and 3×10^{-8} torr in the detector region when there is no gas load. Under typical operating conditions when the pulsed valve is running at 10 Hz with an opening time of 500 μs, pressures are near 5×10^{-5} torr in the source region and 5×10^{-6} torr in the main region.

The ion optics assembly used in this instrument consists of four mesh-free ion optics as opposed to the three used in traditional velocity map ion imaging as introduced by Eppink and Parker.[44] The ion optics assembly is explained in full detail in Section C of this chapter.

The position sensitive detector consists of a 40 mm diameter dual chevron matched set of MCPs with a 10 μm channel diameter and a channel length to diameter ratio of 60:1 (Burle, Part Number 31332). The dual MCP assembly is placed directly in front of a P47 phosphor screen with a lifetime of a few nanoseconds.

B. Newton Sphere Analysis

The purpose of molecular reaction dynamics is to fully understand simple two body chemical events such as bimolecular reactions, inelastic scattering, photoionization, and photodissociation.[45] With the development of experimental techniques such as tunable lasers, molecular beams, and position sensitive detectors, molecular reaction dynamics has become a central field in physical chemistry. Measurement of the asymptotic properties of the reactants and products, one can elucidate details about the actual event itself. A better understanding of these events allows for the critical evaluations of assumptions and models used in calculating reaction rate constants such as the separability of nuclear and electronic motion and rapid vibrational energy redistribution.[46]

Such studies require accurate characterization of both the reactant species and product species. These measurements are of two types, scalar quantities and vector quantities. Scalar properties include the translational and internal energy states of the products, and correlations of these quantities. Vector quantities include the relative recoil velocity and the angular momentum vectors of the products and, in dissociation reactions, the transition dipole moment of the reactant and correlations of these.[47]

In the case of a molecule, AB, undergoing photodissociation to fragments A and B, the magnitudes of the fragment velocity are directly related to the kinetic energy release. By energy conservation, the total translational energy of the fragments is the energy remaining after the bond dissociation energy and the internal energies of the fragments have been subtracted from the energy of the photon used to dissociate AB and the internal energy of the parent molecule.

The velocity of each fragment is given by linear momentum conservation:

$$v(A) = \sqrt{2\frac{m_B}{m_A m_{AB}} E_{trans}} \qquad (2.1a)$$

$$v(B) = \sqrt{2\frac{m_A}{m_B m_{AB}}E_{trans}} \qquad (2.1b)$$

where m_A and m_B are the masses of the fragments respectively, m_{AB} is the mass of the parent molecule AB, and E_{trans} is the total translational energy as described above.

The angular direction of the recoil vector is determined by the photodissociation process, the transition dipole moment of the parent molecule and the photon polarization. Molecules whose transition dipole moment (μ) is aligned with the laser polarization will preferentially absorb the photons. If the lifetime of the molecule after it absorbs the photon is much shorter than a rotational period (~1 ps) the velocity vectors will correlate to the dipole moment. In the simple case of a diatomic, this transition is called parallel if the dipole moment lies along the bond axis and perpendicular if the dipole moment lies perpendicular to the bond axis. The distribution of intensities can be described as a function of θ only since there is cylindrical symmetry about the z-axis. This distribution for a one-photon transition is given by Equation 2.2,

$$I(\theta) = \frac{1}{4\pi}(1 + \beta P_2(\cos(\theta)) \qquad (2.2)$$

where β is the anisotropy parameter, and $P_2(\cos\theta)$ is the second Legendre polynomial.[48] In the case of prompt diatomic dissociation parallel transitions, β=2, and for perpendicular transitions, β = -1. If β = 0, the distribution is isotropic. In the case of prompt dissociation, mixed absorption will lead to an intermediate value of β. In the case of predissociation, the lifetime of the excited state molecule may be on the order of the rotational lifetime of the parent molecule, so the lifetime of this state with respect to the rotational lifetime can be determined using β.[45]

C. Experimental Setup

The experimental setup includes pulsed laser light sources for photodissociation of a parent molecule and electronic state selective ionization of the photofragment of interest. The lasers intersect the molecular beam at a perpendicular angle between the first two ion optics, a space known as the interaction region. A schematic diagram of the general experimental setup used in these experiments is shown in Figure 9.

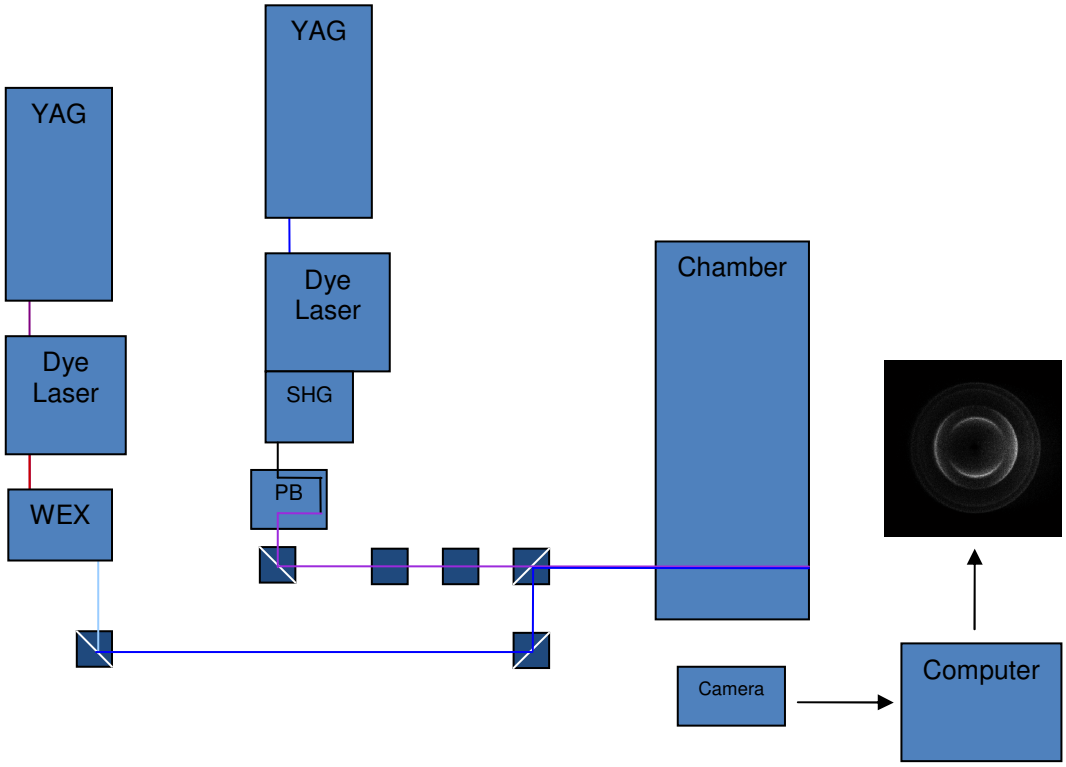

Figure 9: Block diagram of the experimental setup used for the experiments described in this dissertation. Solid lines represent laser propagation. SHG: Second Harmonic Generation. PB: Pellin-Broca prisms.

Two 10 Hz laser systems were employed in these experiments. The photodissociation laser system consists of a pulsed dye laser (Spectra-Physics PDL-1) pumped by the 532 nm output of a Nd: Yttrium Aluminum Garnet (YAG) laser (Spectra Physics GCR 150-10). The dye output is frequency doubled using the appropriate potassium dihydrogen phosphate (KDP) doubling crystal or frequency mixed using the 1064 nm fundamental of the Nd:YAG when needed to achieve the desired photodissociation wavelength. Frequency doubling and mixing are done using a Spectra Physics WEX-1 (wavelength extender). The photodissociationn beam is vertically polarized using a double fresnel rhomb followed by a polarizer. The ionization laser system consists of a pulsed dye laser (LAS LDL 2051) pumped by the 355 nm output of

an Nd:YAG (Spectra Physics 150-10) whose output is frequency doubled using a BBO (beta barium borate) crystal. The doubled light is used to ionize the appropriate atomic photofragment in a specific electronic state using 2+1 REMPI (Resonance Enhanced Multi-Photon Ionization). More detail about the 2+1 REMPI technique will be supplied in Section C of this chapter. The doubled and fundamental outputs of this laser system are separated using a series of four pellin broca prisms. The four pellin broca prisms compensate for the changing refraction angle of the light as the wavelength allowing us to scan the wavelength of the ionization laser in order to image different electronic states without compromising the overlap of the photodissociation and ionization laser beams.

Typical output powers for the Nd:YAG lasers are: 330 mJ/pulse for the 532 nm output of the photodissociation system and 200 mJ/pulse for the 355 nm output from the ionization system. The power of the fundamental output of the dye lasers depends not only on the power of the pump laser, but depends strongly on the dye efficiency curve of the dye being used. The dye Coumarin-450 (C-450) is commonly used in the ionization dye laser, and typically gives about 20 mJ/pulse of fundamental output. Doubling by the BBO usually yields about 0.8 to 1.0 mJ/pulse which is significantly less than the 10% efficiency expected from a BBO crystal. Although these powers are sufficient for the experiment, it is believed that with more careful alignment of the BBO, the doubled output power could be improved. Under the current experimental conditions, the output power of this system after the set of pellin broca prisms needs to be only about 0.2 mJ/pulse or higher to have ample 2+1 REMPI signal.

Using Rhodamine 590, the normal power output of the PDL-1 is about 60 mJ/pulse of fundamental output at the peak of the dye efficiency curve. Doubled output from the WEX-1 typically has powers of about 5% to 10% of the fundamental output power. Frequency mixing of the doubled dye output with the Nd:YAG fundamental (1064 nm) by the WEX-1 usually yields less than 5% of the fundamental power. We have found that powers as low as about 0.3 mJ/pulse after the polarization optics are sufficient for the photodissociation laser.

The wavelengths of the fundamental dye emission of both laser systems are calibrated using a neon-copper cathode opto-galvanic (OG) lamp. The grating of the LDL 2051 dye laser is controlled by a computer interface (Wavescan OG) which allows the dye laser output wavelength to be selected, calibrated, and scanned. Wavescan OG also controls the angle of the BBO crystal insuring that the doubled power is optimized by adjusting the crystal angle as the fundamental wavelength is changed. The fundamental output of the LDL 2051 dye laser is calibrated using an OG lamp that is housed inside the laser. A fraction of light from the oscillator shines into the lamp using a fiber optic. The wavelength of the fundamental dye output of the PDL-1 is controlled by either a PDL stepper motor controller or by manually turning a dial on the laser itself. The dial has an analog counter box with conversion factors allowing the grating order and approximate wavelength needed to be calculated. Calibration is done manually with an OG lamp giving a more specific counter number to wavelength conversion formula.

The photodissociation and ionization beams are combined using an appropriate dichroic mirror which allows the ionization wavelength to pass through the back while reflecting the photodissociation laser light. The beams are then passed through a lens, focusing them into the interaction region within the chamber. The focal point of the lens is wavelength dependent, but is about 20 cm, and can be adjusted using a horizontal adjustment stage. The lens is adjusted to maximize the signal while minimizing the noise which can occur due to a tightly focused beam which can ionize non-resonant species if the photon density is too high. There is also some trade-off between a tighter focus of the photodissociation beam or the ionization beam in the interaction region caused by the wavelength dependence of the focal point; again, adjustments are made during the experiment to maximize signal and minimize noise. This adjustment is very dependent on the relative laser powers as there is a need to avoid multi-photon processes by the dissociation laser and dissociation by the ionization laser.

The molecular beam is made by seeding a few percent of a sample gas in 1 atm of He. The gas mix is introduced into the chamber through a solenoid pulsed valve (Series 9, Parker Hannifin). Currently, only Teflon poppets are used in the pulsed

valves. Although they wear more quickly than the Kel-F poppets, they seal more easily and produce a stronger molecular beam in this application. The radical beams used in this study are produced using custom made fittings for the commercially available pulsed valve. These are explained in full detail in later sections of this chapter. The valve assembly is mounted at a distance of about 1 cm from the skimmer (orifice diameter: 0.8 mm). This ensures that the gas sample entering the main chamber is at terminal velocity. Placing the assembly the correct distance from the skimmer is accomplished by flowing high pressure helium (~30 psi) through an open pulsed valve as the assembly is slowly slid along its mount towards the skimmer. By listening to the helium flow coming through to the Main Chamber side of the skimmer, optimal positioning of the pulsed valve assembly can be obtained. The helium flow sounds loudest and has a uniform pitch when the pulsed valve assembly is placed at the proper distance from the skimmer.

The laser delay is adjusted so that it crosses the molecular beam at the proper time to give maximum signal. This timing is especially critical in the experiments described in this work due to the fact that the halogen oxide radicals studied are produced within the chamber by a reaction of two molecules or by decomposition of a precursor molecule. This causes the variations in composition of the molecular beam at different times, and optimum timing with respect to the molecular beam must be found where concentrations and conditions of the reactants are best for producing the most halogen oxide species of interest. After photodissociation of the halogen oxide species, the atomic photofragment of interest is ionized using a 2 + 1 REMPI transition. The ionization laser is timed to reach the interaction region 15 to 20 ns after the dissociation laser. This interval gives the dissociation sufficient time to take place while still ionizing the fast moving fragments traveling perpendicular to the laser propagation from escaping the interaction region.

The ionized photofragments are then accelerated and focused onto a position sensitive detector consisting of a set of dual chevron MCP plates and a phosphor screen. The accelerated ions are projected onto the grounded front MCP plate with an electron

gain of ~10^6 or ~10^7 electrons which are accelerated onto the phosphor screen by a large potential energy difference. In order to achieve this potential energy difference, the phosphor screen is held at a constant 5000 V. The second MCP plate's voltage is alternated between 2200 V and 1600 V. The MCP voltage is supplied through a DEI high voltage pulse driver. In order for phosphor screen to flash brightly enough to be detected by the CCD camera and not be discarded as camera noise, the gain voltage of the MCP plates should be no less than 1850 V. Pulsing the voltage of the MCP between 2200 V and 1600 V allows for mass selection while reducing the shock to the MCP of a full voltage drop.

A CCD (charge-coupled device) camera (Mintron MS-2821 E/C) is placed directly behind the phosphor screen. The focus of the camera on the phosphor screen is extremely critical to the success of data collection. Proper focus is achieved by adjusting the camera position and focus while the instrument is running. Adjustment of the camera focus is made while observing a real time monitor of the camera image such that each ion event is as bright and sharp as possible. A photomultiplier tube (PMT) is placed off-axis behind the phosphor screen to collect the overall intensity of the signal. This signal is sent to an SRS (Stanford Research Systems) boxcar averager unit that allows collection of a mass spectrum and aids in maximizing signal intensity through proper laser and MCP pulse timing. The PMT signal is also sent to the computer interface of the LDL 2051 where the software Wavescan OG collects the intensity as it scans the laser wavelength so that 2 + 1 REMPI intensities can be recorded. The CCD camera and the PMT are housed inside a black plexiglass enclosure to minimize stray light from interfering with signal collection.

The camera image is collected using a National Instruments frame grabber (PCI-1405) and associated computer software interface. The data collection software used (IMACQ) was developed by Suits and co-workers.[49] Image reconstruction is done using both BASEX (BAsis Set EXpansion) and pBASEX softwares.[50, 51] The advantages of each of these methods will be discussed in a later section of this chapter. The camera signal is also sent to two black and white monitors so that instantaneous images of the

signal can be seen while laser alignment and timings are adjusted which is a great assistance during signal optimization.

Proper timing of all of the components of the experiment is critical to its success. The CCD camera runs at 30 Hz, and provides master-clock for the rest of the experiment. The camera provides an external trigger for a pulse generator (BNC) which, in turn triggers the opening of the pulsed valve(s), the gate for the MCP pulse driver (DEI), and a separate pulse generator (SRS) that triggers the lamps and Q-switches of both lasers. Widths and delays of all of these components are essential to having proper signal. The pulsed valves are usually operated using a pulse width of 180 ns, although pulse widths of up to 800 μs are not uncommon. The pulse width of the MCP gate is usually set to 500 μs, which is narrow enough to discriminate against unwanted masses yet wide enough to ensure that all events from a given mass are counted.

D. Ionization of Photofragment Atoms Using 2 + 1 REMPI

Photofragment atoms are detected using 2 + 1 REMPI (Resonance Enhanced MultiPhoton Ionization). This technique requires that each photofragment atom absorb three photons of light in order to be ionized. Two photons of the same frequency are simultaneously absorbed by the photofragment to reach a resonant excited state. This resonant state is sufficiently long lived to allow a third photon of the same frequency to be absorbed to ionize the fragment. As an example of this process, ionization of oxygen atoms using 2 + 1 REMPI is shown in Figure 10.

This detection method is invaluable to ion imaging for a number of reasons. Firstly, the ionization potentials of the atoms studied in this work have ionization potentials larger than 10 eV which are too large for single photon ionization process using the current laser systems. Secondly, and more importantly, 2 + 1 REMPI transitions are state-selective processes, meaning that only fragments in a specific quantum state are detected. This means that not only can the mass of the photofragment be selected using the MCP gating and time of flight tube, but fragments of a specific internal energy can be selectively ionized as well by simply tuning the ionization laser

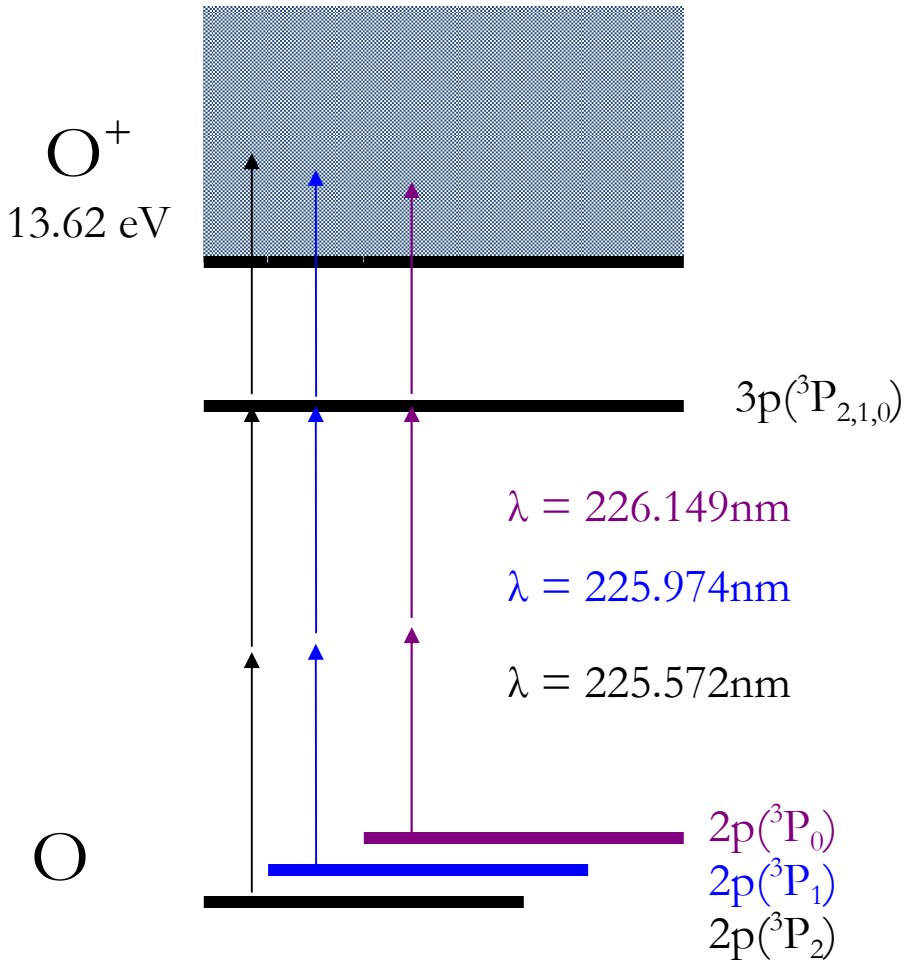

Figure 10: Schematic energy diagram of the 2+1 REMPI transition of O(^3P_J). The diagram shows the absorption of two photons of light by the oxygen atom, raising it to a resonant intermediate energy level. The atom then absorbs one more photon of the same frequency light to eject an electron forming an O+ species.

the wavelength specific to the electronic state that is desired. This highlights one of the key advantages of using velocity map ion imaging with 2+1 REMPI detection. This method allows us to obtain correlated information about the photodissociation process. Because of the state selectivity of 2+1 REMPI detection, the electronic state of the detected fragment is known. In addition, the internal energy of the unseen fragment is also measured as a result of the measured speed distribution of the detected fragment. The 2 + 1 REMPI transitions of atomic species studied in this work are given in Table 1.

Table 1: 2+1 REMPI transitions of atomic species of interest in this study. The table includes the original electronic state of the fragment being detected, the intermediate resonant state reached by absorbing two photons of the wavelength of light listed.

Atomic Species	Electronic State	Intermediate State	Wavelength (nm)	Reference
O	$^3P_2$	3p $^3P_{2,1,0}$	225.572	52
	$^3P_1$	3p $^3P_{2,1,0}$	225.974	52
	$^3P_0$	3p $^3P_{2,1,0}$	226.149	52
Cl	$^2P_{3/2}$	4p $^2D^0_{3/2}$	235.336	53
	$^2P_{1/2}$	4p $^2P^0_{3/2}$	235.205	53
Br	$^2P_{3/2}$	5p $^4P^0_{3/2}$	266.650	54
	$^2P_{1/2}$	5p $^3S^0_{3/2}$	266.713	54
I	$^2P_{3/2}$	6p $^2D_{5/2}$	304.67	55
	$^2P_{1/2}$	6p $^4D_{1/2}$	304.02	55

The measured 2 + 1 REMPI transitions of oxygen arising from the predissociation of the $v' = 2$ transition of ClO at 307.9 nm are shown in Figure 11. The intensities of the peaks can be integrated and used to determine the branching ratios of the oxygen states for this transition. Because the 2 + 1 REMPI process requires the absorption of two photons in order to reach a resonant electronic state, the two photon transition probabilities for the specific transitions must be included in order for branching ratios calculated from the transition intensities to be accurate. The two photon transition probabilities for the three oxygen spin orbit states (^3P_J) at transitions near 226 nm are identical allowing them to be ignored in the branching ratio measurements of BrO and ClO done in this work.[52] In contrast the transition probabilities for the halogens are unequal and the 2+1 REMPI signals must be corrected.

Photodissociation results in photofragments released over a range of angles forming a Newton sphere. The frequency of light from the ionization laser must be adjusted for fragments that are moving toward or away from the direction of laser

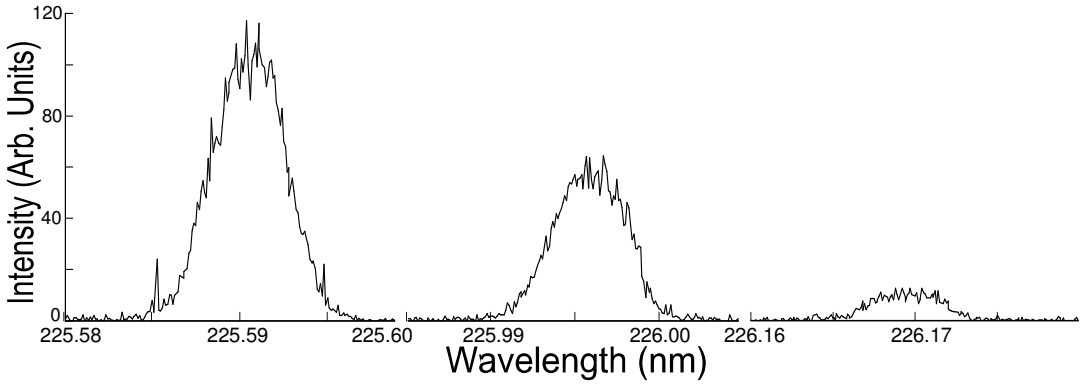

Figure 11: $O(^3P_J)$ 2 + 1 REMPI transition intensities for the photodissociation of ClO at 299.5 nm. From these intensities, the branching ratios of the ClO dissociation into the three oxygen states can be determined.

propagation due to the Doppler effect. The amount of adjustment is given by the following equation:

$$\nu = \nu_0 (1 \pm \frac{u}{c}) \tag{2.3}$$

where ν is the adjusted frequency, ν_0 is the 2 + 1 REMPI transition of a fragment with zero velocity in the direction of laser propagation, u is the projection of fragment velocity along the direction of laser propagation, and c is the speed of light. In order to ionize all of the fast-moving fragments, the Doppler Effect is non-trivial. For example, the $O(^3P_2)$ fragment in the case of ClO photodissociation near 300 nm is traveling greater than 3000 m/s. If the fragment is traveling either directly toward or away from the laser propagation, the 2+1 REMPI transition for this fragment will shift by about 0.003 nm. Although this seems relatively small, it is about 0.5 cm^{-1} which is on the same order as common bandwidths of doubled dye lasers. To ensure detection of fragments moving in any direction, the 2+1 REMPI ionization laser used must either have a broad enough bandwidth to ensure all of the fragments are ionized at once, or must be scanned over the Doppler profile while the image data is collected. For images

that illustrate this effect, see reference 43. The advantage of using a broad bandwidth laser is evident as it allows the entire image to be collected at once. However, one disadvantage is that the laser power is distributed over a larger wavelength range meaning laser powers are sometimes too low for two photon processes to occur readily as the probability of the transition decreases quadratically with laser power.

The LAS laser system used in the experiments described here has a bandwidth of ~0.1 cm^{-1}, and the while the PDL has a bandwidth of ~1 cm^{-1} or more. In the ClO and BrO experiments described in this dissertation, the narrow band LDL 2051 is used for ionization. The Doppler effect is compensated for by scanning the laser wavelength across the transition. In the IO experiment, the PDL-1 is used to ionize the I($^2P_{3/2}$), and because of the larger bandwidth of this laser and the slow speed of the iodine fragment, no scanning was necessary.

E. Ion Optics

Two-dimensional ion imaging was pioneered by Chandler and Houston in 1988.[56] They used a position sensitive detector allowing visualization of the photodissociation event while obtaining the speed and angular distribution in one measurement. Although this novel technique could collect all angular and speed information with one experiment, the images collected using this instrument were blurred due to fine meshes used in the ion optic assembly. These meshes blurred the velocity distributions by slightly deflecting the ions, and also significantly lowered the signal intensity by only transmitting ~60% of the beam through each mesh. However, the most significant problem with the meshes was that the photofragment ion was projected onto the detector at a position that was dependent of where the fragment was formed. Because of the finite size of the photodissociation laser beam and molecular beam, dissociation events occurred at various positions which caused the photofragments to be projected to different positions on the detector. Because the relative size of the interaction region is a few millimeters and the detector size is generally about 20 millimeters, the velocity resolution using this technique was limited to about 10%. This

low kinetic energy resolution caused imaging to be less favorable in some instances than time of flight methods.[42]

Eppink and Parker modified the ion optic assembly used in the ion imaging by replacing the meshes with an Einzel lens assembly of electrostatic stainless steel disks with open electrodes.[57] The Einzel lens assembly exploits the full potential of ion imaging by project all photofragment ions with the same velocity vector to the same position on the detector regardless of the origin of the dissociation. The advance in the ion optics warranted adding "velocity map" to the term ion imaging. This improvement made velocity map ion imaging a more useful quantitative tool to the molecular dynamics community as it effectively increased the velocity resolution. In the original velocity map ion imaging paper of Eppink and Parker, trajectory simulations showed a blurring of about 0.4 mm in each dimension using a 2.12 mm ion source (equivalent to an interaction region) and a 20 mm radius, limiting the velocity resolution to about 2%. The velocity map ion imaging system used in the experiments described here consistently provide us with a velocity resolution of 3%.

Recently, Suits and coworkers proposed a modification of the Einzel lens assembly that allows for the stretching of the ion cloud along the flight axis.[58] Although other groups have also explored experimental methods to allow for the imaging of only the center slice of the image through various techniques, the dc-slicing technique of Suits and coworkers provides all of the advantages of image slicing without some of the negative results of other methods such as image blurring and difficult implementation.[58,59,60,61,62] Using the DC-slicing technique, the ion cloud can be stretched temporally to about 300 ns, so that it is possible through gating the detector to select only the center 50 or 60 ns of the ion cloud. The resulting image is the center slice which is the equivalent to the result of the reconstruction methods. It boasts an improvement of the velocity resolution to below 0.2% using the same initial conditions for a trajectory simulation as that of Eppink and Parker that produced a 2% velocity resolution using the traditional ion optics. Another advantage of the slicing is that it circumvents the need for mathematical image reconstruction methods, eliminating both

the noise from inversion methods as well as the need for cylindrical symmetry in the data.

The velocity map ion imaging instrument used in the experiments described here has been recently modified to include a set of four Einzel lenses so that image slicing using DC-slicing is possible. The ion optics assembly consists of 4 stainless steel plates (7.6 cm outer diameter, .16 cm thick) with center bores cut in each. Diameters of the center bore of each ion optic, in order beginning with the optic nearest the source region are: 6 mm, 12 mm, 32 mm, and 40 mm. The cross sectional view and full dimensions of the ion optics are shown in Figure 12. The ion optics are assembled on 0-80 stainless steel threaded rod that is insulated from the optics using a vespel ceramic tube. Vespel spacers of varying lengths are used to achieve the desired spacings between the ion optics of 29 mm, 21 mm, and 14 mm in order beginning with the space nearest the source region. Voltages applied to the first three ion optics vary depending on the type of ion being imaged, and the desired size of the image. The ion optic nearest the detector is always grounded. Optimum focusing of the ion cloud was found to be achieved when the voltages of the second and third ion optic are given voltages of approximately 0.88 and 0.78 of the ion optic closest to the source. Specific voltages used during each experiment are discussed in subsequent chapters. The assembly is mounted in the main chamber region such that the ion optics are perfectly parallel to the detector and centered exactly around the molecular beam.

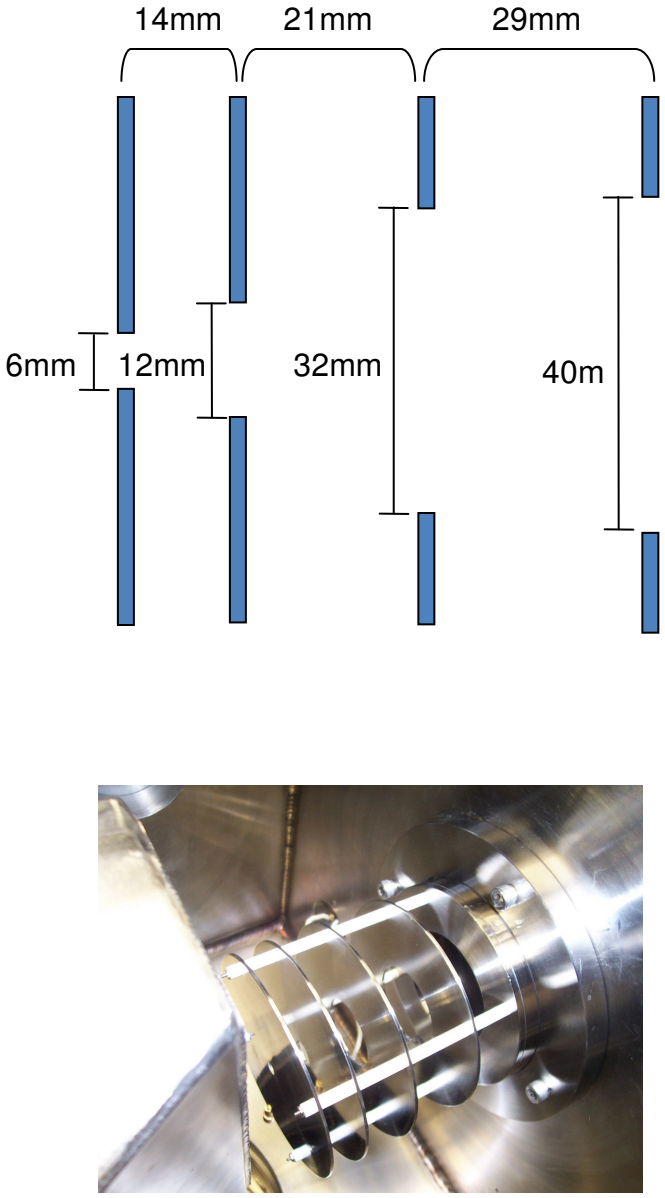

Figure 12: Cross-sectional view and photograph of the ion optics assembly used in the experiments described in this dissertation. Top image shows the cross sectional view of ion optic assembly. Shown with dimensions (in mm) of spacings. Lower image shows a picture of the ion optics assembled in the main region of the imaging chamber.

Simion 7 software was used to simulate the ion trajectories of these ion optics to demonstrate their focusing and temporal stretching of the ion cloud.[63] The simulation results are shown in Figure 13 using the 303 nm photodissociation of ClO with imaging of the Cl fragment as an example of the abilities of the ion optics assembly. The ions in the simulations originate halfway between the first two ion optics. The ions begin their trajectories from three points along the direction of laser propagation by expanding in all directions, typical of a photodissociation event. Image (a) in Figure 13 shows the ability of the ion optics assembly to focus ions of the same velocity to a certain point on the detector regardless of the starting position of the ion clouds. Images (b) and (c) show the spread of the ion cloud along the axis of the molecular beam at positions within the ion optics and later, just before the ion cloud strikes the detector. A third image (d) is used to show the velocity of the ion cloud by showing the distance traveled by the ion cloud in a given amount of time (5 μs). Using the velocity derived from (d), the temporal spread of the ion cloud in Images (b) and (c) can be calculated. The minimum temporal stretch of the ion cloud for dc-slicing to be useful is 300 ns. Below this, the MCP voltage gate is not short enough to slice the center of the image and will blur the speed distribution.

The new ion optic assembly was tested by imaging the $Cl(^2P_{3/2})$ fragment of ClO photodissociation at 235 nm. Although slicing was observed, this technique was not used in the current study for several reasons. Firstly, this technique discards many events from each ion cloud. This loss of signal cannot be afforded during experiments such as the photodissociation of IO where signal is already low and not stable for periods of time long enough to allow long averaging times. It was noted above that image slicing is only possible when the fragment ion is heavy enough to allow significant stretching of the ion cloud. In the case of the BrO and ClO experiments performed, the oxygen fragment is too light for adequate stretching given the size of the detector used in the instrument. Although the full potential of the new ion optic assembly was not taken advantage of in these experiments, adding an extra focusing lens seems to have improved the focus of the images collected.

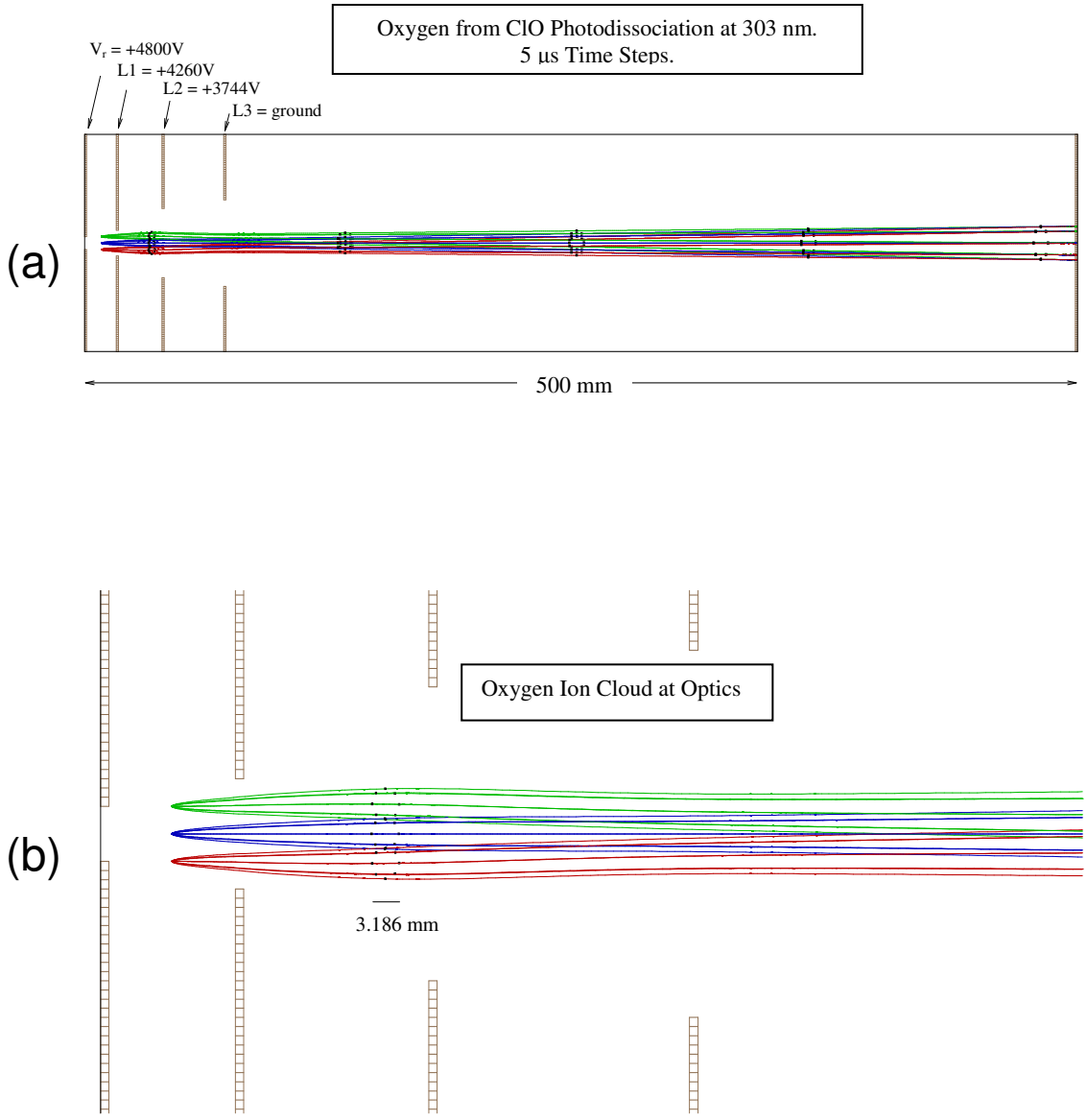

Figure 13: Simion 7 simulations of the ion optic assembly. Top image (a) shows the full simulation length from the interaction region to the detector. Voltages used in this simulation are listed above the ion optic. Image (a) demonstrates the velocity focusing ability of the ion optic assembly. Center images, (b) and (c), show the ion cloud near the interaction region (b), and near the detector (c). The dimensions of the ion clouds along the axis of propagation are shown below the ion clouds in mm. The lower image (d) shows the distance traveled by the ion cloud in 5 µs.

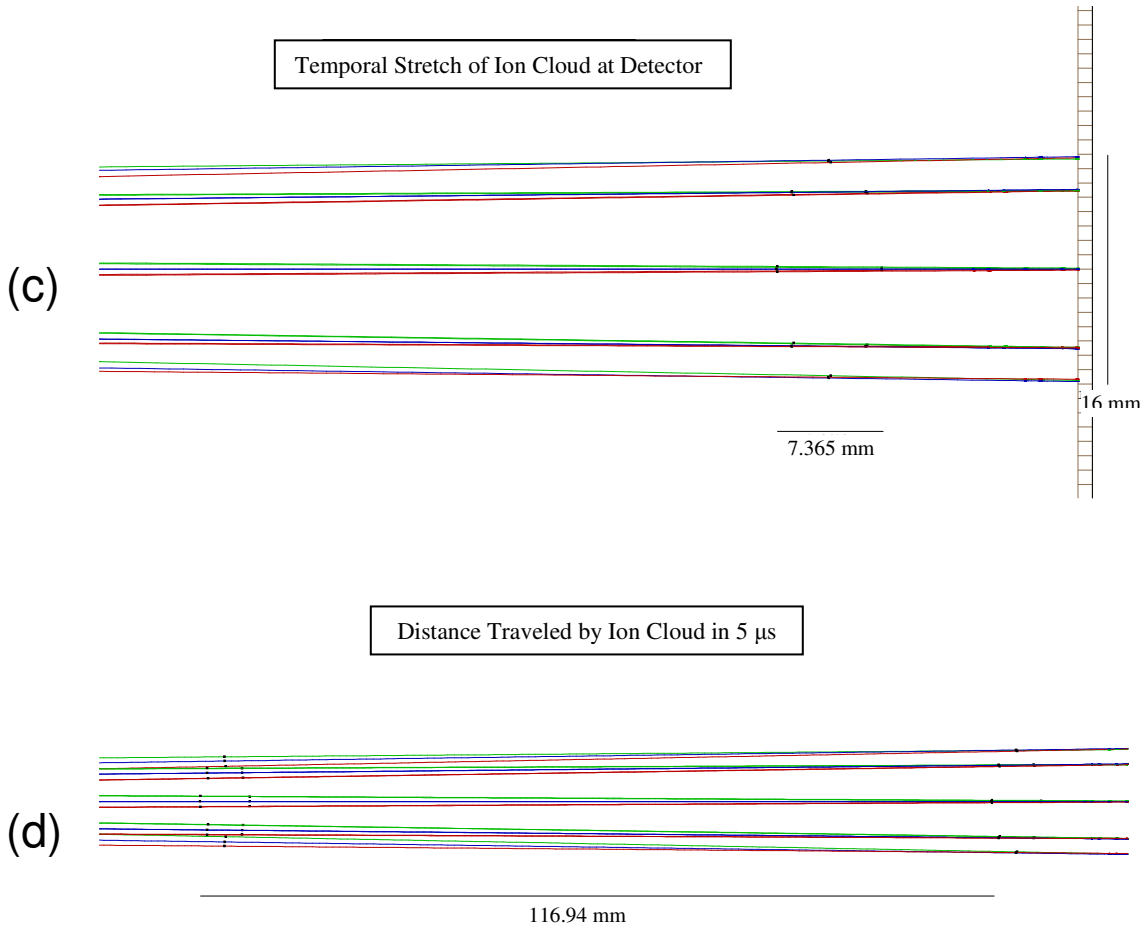

Figure 13: (Continued.)

F. Data Acquisition

The CCD camera collects images of the phosphor screen at a rate of 30 Hz. Because the rest of the instrumentation functions at only 10 Hz, a maximum of one out of every three camera images collected by the computer interface will contain image data. In order to maximize the number of frames containing data, the CCD camera serves as a trigger for the rest of the instrumentation. Digital pulse generators triggered by the CCD camera establish proper timing of the pulsed valves, the MCP gate pulse, as well as the lasers.

Although the Einzel lens assembly provides much better focusing of the image than the original meshes, the images collected from this instrument still has noise due to the relatively large spot generated when the phosphor screen flashes. The ion event spot is roughly 5 x 5 pixels, although the spot size will increase if the MCP voltage is increased and is dependent on the camera focus and the chip dimensions. The large spot generated by each event causes the raw image to be blurred and the velocity information to be broadened significantly. Centroiding is an event counting technique that effectively enhances the image resolution when the ion count rates are low. Centroiding first sets a threshold to discriminate against events and noise. This is achieved by defining a threshold pixel intensity below which the event is disregarded. For those events above the threshold intensity, the pixel of local maximum intensity is found in both the X and Y directions defining a "centroid" position. The computer then places one count on that pixel. Centroiding effectively enhances the resolution dramatically by reducing the ion spot size and also effectively removes essentially all noise events from the collected image.[64]

Although centroiding can be a useful tool in ion imaging, some conditions should be met to ensure optimal use. First, care should be taken that the threshold value is sufficiently high to reject noise while remaining low enough to count all events from true signal. Second, low enough count rates are required such that there are not overlapping events with each laser shot. This is because overlapping events are

recognized as single event when using centroiding, causing distorted speed and angular distributions.

A technique developed by Arthur Suits and coworkers called megapixel imaging further increases the resolution of the image to sub-pixel resolution by building somewhat on the idea of centroiding.[49] In theory, the ion spot has a Gaussian distribution of intensity, so it should be ideal to fit each ion spot with a Gaussian distribution to determine the origin of the spot. This is unrealistic for several reasons. Firstly, the ion spot should cover very few pixels (at most seven) which is too few to ensure a proper Gaussian fit. Secondly, fitting the intensity of each ion spot with a Gaussian is too calculation intensive to be functional during real-time data collection. Lastly, some spots may not have a Gaussian distribution of intensity. Some spots are seen to have a Boltzman-like distribution of intensity. As a result, the center-of-mass of each ion spot is found and the ion count is placed at this point. This calculation provides the same position as the center of a Gaussian distribution but is more practical as it is much less computationally intensive and is useful even when the spots do not have a Gaussian distribution of intensity. The resolution achieved by centroiding is the resolution of the camera, or 480 by 480 pixels in our case. Using the software provided by Suits and coworkers, each pixel is divided into a number of subpixels (up tp 100) chosen by the user. For each center of mass thet lies within each subpixel, the subpixel receives an ion count, Using this method, the user is able increase the resolution of the camera up to 10x10 times its original resolution of the camera. Suits and co-workers found that a 5x5 increase in resolution was sufficient, producing a velocity resolution of 0.1%.[49]

Real-time image data collected by the CCD camera is sent to a frame grabber (National Instruments PCI-1405) which is interfaced to an image accumulating software called IMACQ, an image collection interface written by the group of Arthur Suits. IMACQ allows the user to set a low threshold such that small signals due to noise will be rejected during image counting, and a high threshold so that overlapping events are also rejected.

IMACQ allows the user to save the image data in up to three ways: as a raw image with no event counting method, as a centroided image, and as a binary file of the center of mass data for each ion spot. The centroid image is saved as a .tiff file making it easy to convert using ImageJ[65], an open source general image viewer, for use in BASEX or pBASEX. The megapixel file is a binary file and must be read into the IMAN program also available from Suits *et al.* to convert the file to a megapixel image of numerous resolutions of the user's choice, up to 5 times the resolution of the camera.

For the studies discussed in this dissertation, only centroided data is used for the speed distributions, anisotropy parameter data, and image reconstruction. The reason for this is that the main drawback to collecting a megapixel image is the large amount of time it takes to collect a satisfactory image is very long. Although using this technique is very desirable, it is unrealistic for our work with radical species as the molecular beam can become unstable during the course of image collection.

G. Data Analysis

Because the detector is 2D, the images that are collected are a 2D projection of a 3D Newton sphere. A schematic of this is shown in Figure 14. For this reason, the information needed to obtain proper velocity and angular information is contained within the center slice of the Newton sphere. There are two methods of obtaining this center slice. The first method involves selecting only the center slice using experimental techniques. One such technique was introduced by Tonokura and Suzuki using laser sheet ionization to selectively ionize photofragments along the center of the Newton sphere.[59] Another slicing technique was pioneered by Suits and coworkers and was explained in detail in Section D of this chapter which utilizes four ion optics to stretch the Newton sphere temporally so that only the center slice is imaged.[58] When experimental methods are not used or are not feasible, analytical methods must be used to recover the center slice of the Newton sphere. To this end, mathematical inversion methods must be used to reconstruct the 3D data so that accurate velocity and angular distributions can be obtained.

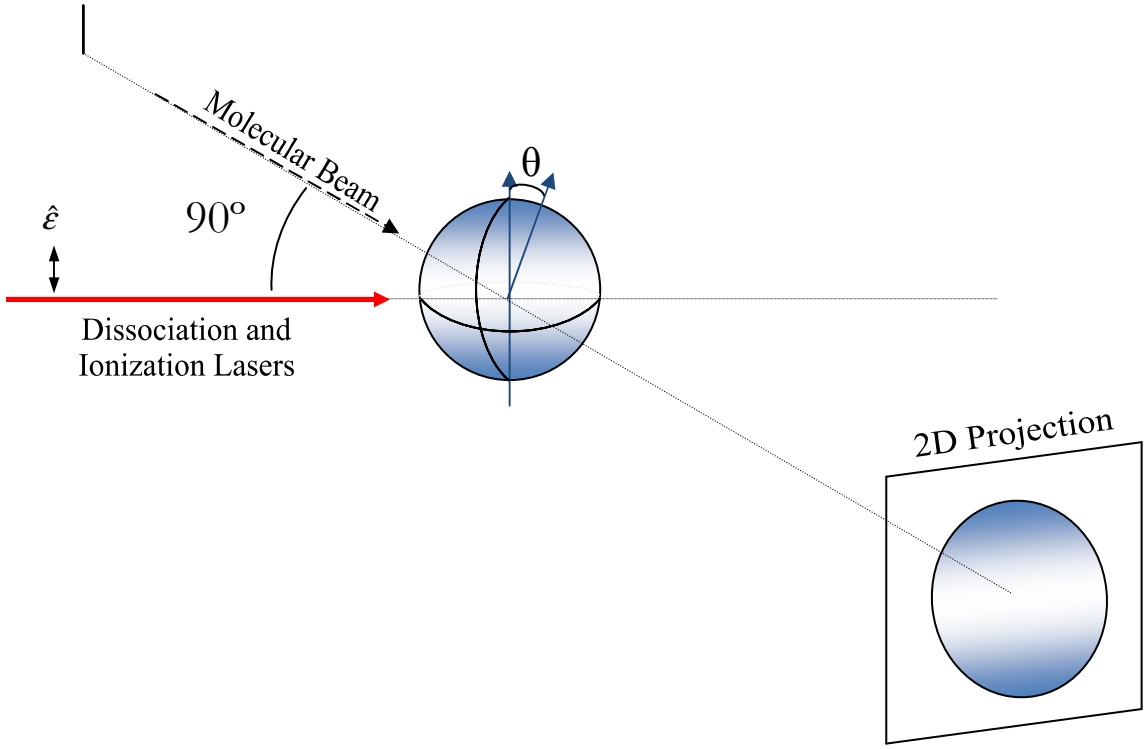

Figure 14: Schematic diagram of the detection of a 2D projection of a 3D Newton sphere.

Because experimental methods to extract only the center of the Newton spheres were not used in the experiments that follow in this dissertation, analytical methods were used to reconstruct all of the data shown in Chapters III-V. Fortunately, because the dissociation laser is vertically polarized, there is cylindrical symmetry in the Newton sphere making common mathematical reconstruction techniques possible through forward convolution methods. Currently, we use two inversion methods to analyze the imaging data collected from the ion imaging instrument called BASEX (BAsis Set EXpansion) and pBASEX (polar BAsis Set EXpansion). The two reconstruction methods will be explained further, and a comparison of the advantages of these methods will follow.

BASEX is a commercially available program which was developed by Reisler and coworkers.[66] The reconstruction begins by building a 2D projection from a basis set of functions that are analytical projections of well-behaved functions similar to Gaussian functions. The expansion coefficients found by building this projection provide the information needed to construct the 3D velocity distribution. Because the 2D projection of the Newton sphere has cylindrical symmetry, it can be described using an Abel integral:

$$P(x,z) = 2\int_{|x|}^{\infty} \frac{rI(r,z)}{\sqrt{(r^2 - x^2)}} dr \qquad (2.4)$$

where the z-axis lies along the symmetry axis (laser polarization vector), the x-axis lies also in the plane of the detector perpendicular to the z-axis and r is the result of converting to polar coordinates ($r^2 = x^2 + y^2$). In this equation, I(r,z) is the intensity of the signal as a function of r (the distance from the center of the image) and z, or the original 3D intensity distribution which is depicted in the schematic in Figure 15.

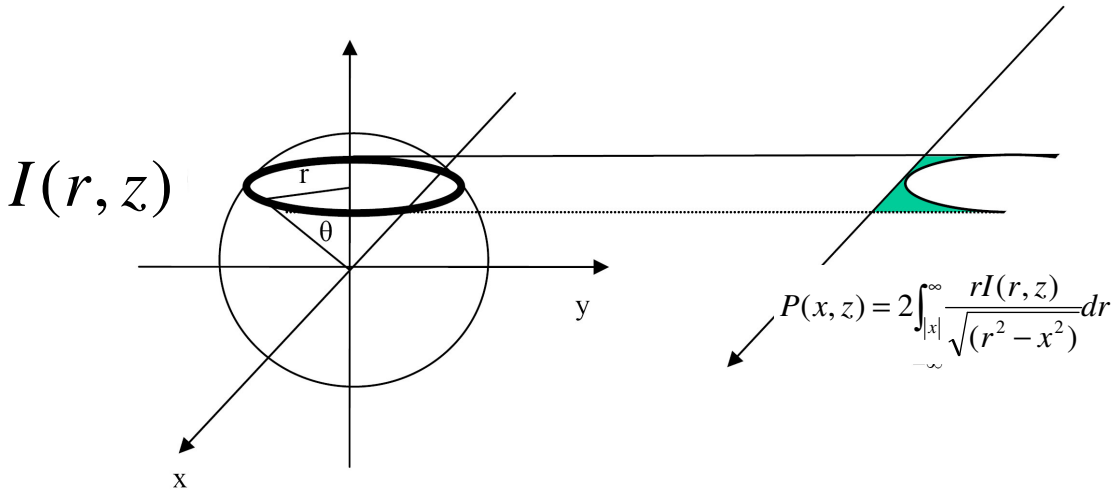

Figure 15: Schematic diagram of the 3D intensity (I(r,z)) being projected into 2D. Each slice of the 3D Newton Sphere is projected as a line. Figure adapted from Reference 43.

However, because the experiment bins the data into discrete pixels, we can write the projection as a function **P**.

$$\mathbf{P}_{ij} = 2\int h(x-x_i, z-z_j)dxdz\int_{|x|}^{\infty}\frac{rI(r,z)}{\sqrt{(r^2-x^2)}}dr \qquad (2.5)$$

Assume a set of basis functions and their corresponding projection, **G**.

$$\mathbf{G}_{kij} = 2\int h(x-x_i, z-z_j)dxdz\int_{|x|}^{\infty}\frac{rf_k(r,z)}{\sqrt{(r^2-x^2)}}dr \qquad (2.6)$$

where h(x,z) is an instrumental function. The idea is now to make an expansion of this function in terms of a basis of known projection functions. Next, the 3D velocity distribution I(r,z) can be written as a function of the basis set:

$$I(r,z) = \sum_{k=0}^{K-1} C_k f_k(r,z) \qquad (2.7)$$

And the 2D projection (data) can be written:

$$\mathbf{P}_{ij=}\sum_{k=0}^{K-1} C_k \mathbf{G}_{kij} \text{ or } \mathbf{P} = \mathbf{CG} \qquad (2.8)$$

From here, matrix algebra will allow for solving **C**. Finally, the reconstructed speed distribution can be obtained.

Once fit, the basis set analytically calculates the original 3D Newton sphere from the data. Finally, a 2D slice is then taken from the center of the 3D calculation for velocity and angular distribution calculations.[66]

A more recent 2D image inversion method called pBASEX was introduced in 2004 by Garcia, Nahon, and Powis.[67] The goal of pBASEX is essentially the same as that of BASEX: to reconstruct a 3D Newton sphere from a 2D projection by fitting the projection with a set of basis functions with a known inverse Abel integral. The inversion method is based on the same algorithm as BASEX, the main difference being the choice of a polar coordinate system rather than the Cartesian coordinate system used by BASEX.[66] Polar basis sets are advantageous as photoionization processes have polar symmetry, so pBASEX should better optimize velocity and angular information while minimizing CPU time and noise.

Briefly, the energy distribution of the photofragments can be described using a discrete number of Gaussian functions with a given width (σ) using the expression:

$$F(R,\theta) = \sum_{k=0}^{k=k_{\max}} \sum_{l=0}^{l=l_{\max}} c_{k,l} f_{k,l}(R,\theta) \ , \qquad (2.9a)$$

$$\text{with } f_{k,l}(R,\theta) = e^{-(R-R_k)^2/\sigma} P_l(\cos\theta) \, , \qquad (2.9b)$$

where θ is the angle measured with respect to the polarized direction of linearly polarized light or propagation direction for circularly or unpolarized light, P_l is the Legendre polynomial of order l, and R_k is the center of the k^{th} Gaussian. Because the image data will always be Cartesian due to the matrix of pixels in the camera image, the value of σ should be set to about one pixel width to correct for this. The image data can then be converted from Cartesian coordinates to polar coordinates.

When linearly polarized light is used, the odd Legendre terms will disappear from Equation 2.9b , considerably lowering the number of basis functions pBASEX uses to invert the image as compared to the number used by BASEX, thus significantly reducing the computing time of the method. If there exists cylindrical symmetry in the image, the Abel integral:

$$P(R',\theta') = 2\int_{|x|}^{\infty} \frac{rF(R,\theta)}{\sqrt{r^2 - x^2}} dr \qquad (2.10)$$

relates the projected image, $P(R',\theta')$, to the original image, $F(R,\theta)$. The basis functions, having analytic inverse Abel solutions, can then be selected so that a linear expansion of the selected basis functions can be used to describe the projected image through the expression,

$$P(R',\theta') = \sum_k \sum_l c_{k,l} g_{k,l}(R',\theta') \qquad (2.11)$$

where $g_{k,l}(R',\theta')$ is the projection of a particular basis function, and $c_{k,l}$ is that function's coefficient.

Currently, we use both BASEX and pBASEX to analyze the images collected in these experiments. The BASEX software used is commercially available.[66] The

software for pBASEX was obtained from Dr. Lionel Poisson who has implemented the pBASEX code using LABVIEW. His contact information is provided in Note 9.[68] We continue to use both of these methods as they both offer different advantages.

Although the methods of reconstruction are similar for pBASEX and BASEX, the most notable difference in the methods is the difference seen in the reconstructed images. A reconstructed image using BASEX accumulates noise toward a central band running vertically through the image. The method pBASEX collects noise towards the center point of the image. As an example, Figure 16 shows a raw, centroided image, the image after it has been reconstructed using BASEX, and the image after reconstruction with pBASEX. The advantage of pBASEX in the reconstructed image is clear from looking at these images. The reconstruction by BASEX posseses a significant amount of noise along the vertical centerline of the image. The reconstruction by pBASEX is much more desirable as the noise generated by the method is minimal and is centered around the centerpoint where there is no speed element from the data. It is also more visually pleasing and provides a clear visual of the angular distribution of the data that is lost in the BASEX reconstruction.

Although a significant advantage was seen by Garcia, Nahon, and Powis in the speed distributions of images collected with unpolarized light, little difference was seen in the speed distributions when the photofragments originated from linearly polarized light.[67] Figure 17 shows the speed distributions of the data shown in Figure 16 analyzed using BASEX and pBASEX. Our experience with these methods reinforces this similarity as can be seen in Figure 17. The two reconstruction methods produce very similar speed distributions with comparable amounts of noise.

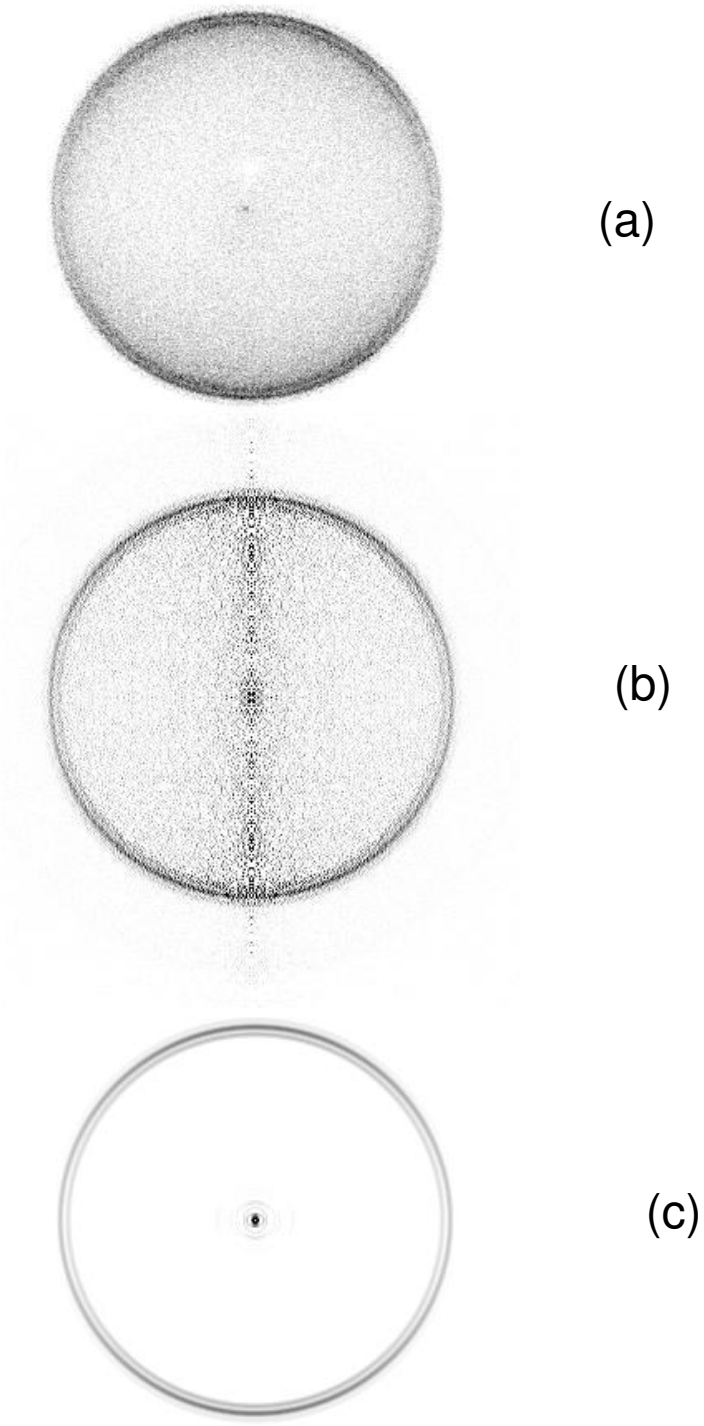

Figure 16: Centroided raw image data (a) and reconstructions using BASEX (b) and pBASEX (c). Example data shown are O(3P2) images taken from the photodissociation of ClO at 291.7 nm corresponding to the v'=6 band.

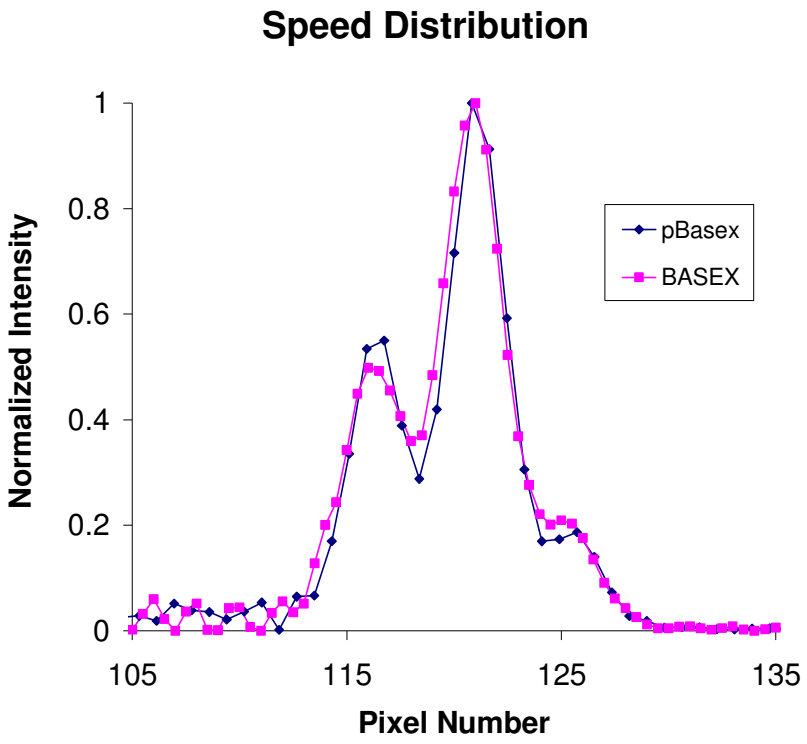

Figure 17: Speed distributions of data shown in Figure 16 from BASEX (red trace) and pBASEX (blue trace) methods.

The anisotropy parameter (β) was calculated for the $Cl(^2P_{3/2})$ fragment data shown in Figure 16 and are seen to be 0.53 and 0.54 for BASEX and pBASEX, respectively. The anisotropy parameters obtained by BASEX and pBASEX methods were examined by Garcia, Nahon, and Powis and are seen to be nearly identical .[67] As can be seen from Table 2.2, the resulting anisotropy parameters obtained from the two methods are similar in our case as well. From experience with these two programs, the BASEX program has a clear advantage over the pBASEX code as it is much easier to use and for this reason is more convenient.

Because the results are very similar, we choose to use BASEX for most of our analysis as it is simpler to use than the pBASEX LABVIEW code. The pBASEX

method does have a clear advantage when the reconstructed images are needed as pBASEX reconstruction produces minimal noise, and the noise is relegated to near the center point of the image.

H. Sources of Velocity Broadening

For velocity map ion imaging to be used as a quantitative technique, some sources of blurring in the images must be avoided or corrected. Two major sources of image blurring have been addressed earlier in this chapter. The first was the blurring due to the finite interaction region which is corrected by using an Einzel lens assembly rather than electrostatic meshes to guide the ions onto the detector. The second was the large spot that each event makes on the detector that spreads the image intensity over many pixels. This is corrected using event counting methods such as centroiding or megapixeling the data. Other sources of blurring are addressed briefly in this section. While the effects of these sources are minor under most circumstances, they can be significant enough to have an effect on the overall errors associated with the data. One instance where slight blurring effects become important is when multiple velocity features are very close to each other, even minimal blurring could cause these features to be unresolved or even overlooked. Imaging the O fragment from the photodissociation of ClO is a good example of this as the velocity features arising from the two spin-orbit states of Cl are quite close. Another prime example of needing to reduce even the slightest source of blurring occurs when measuring the bond dissociation energy of a diatomic species such as IO. In this instance, any blurring of the image causes broadened velocity distributions which, in turn, lead to increased error in the measured bond dissociation energy for the diatomic species.

One cause of image blurring is the space charge effect which occurs when there are too many ions made with each laser shot. It can become a significant effect as ions of any mass/charge ratio can disrupt the imaged ions, even ions of a different and undetected mass. Space charge effects can lead to oval shaped images as the image will be distorted along the axis of highest ion density. This effect can also broaden the rings,

lowering the image resolution, if there are too many ions focused to the same point on the detector. A good rule of thumb is that the formation of ~100 ions with each laser shot is enough to cause this effect to be large enough to be detected. For example, assume the interaction region is a sphere with a diameter of 200 μm, with 100 ions formed by the laser shot that are equally spaced. Using Coulomb's law for charged particles under these conditions, an oxygen fragment ion traveling at 3000 m/s will be repelled about 5 m/s in 10 μs (approximately the time it takes to reach the end of the time of flight tube). This corresponds to a $\Delta v/v$ of about 0.2% which is relatively small compared to other sources of velocity distribution broadening. However, if the number of ions is increased to 1000, $\Delta v/v$ becomes a nontrivial 0.7%.

Corrections for this problem are rather simple. Using a focused laser beam causes the photon density to be very large across a small area, leading to many ions being formed there. Defocusing the laser at the interaction region even by a very small amount can dramatically reduce this effect. Lowering the signal intensity by reducing the percentage of sample in the molecular beam or by shortening the pulsed valve opening time is also an option that eliminates space charge effects.

Ionization using 2 + 1 REMPI, can lead to some broadening of the speed distribution through ion recoil. REMPI ionizes a photofragment (A) through the reaction shown below where A is the photofragment being ionized by 2 + 1 REMPI and n=3.

$$A + n h\nu \rightarrow A^+ + e^- + KE_{Total} \qquad (2.12)$$

The energy absorbed by A from the three photons will ionize A, and provide some amount of extra kinetic energy to the ion and electron formed. This total kinetic energy (KE_{Total}) will provide A^+ and e^- with a velocities based on the conservation of momentum. Although the masses of the ion and the electron are significantly different, it cannot always be assumed that the small amount of energy partitioned to the ion can be ignored. The effect of ion recoil from the REMPI process is dependent on the fragment mass, the total excess energy available from the ionization process, and the speed of the fragment from the dissociation step. For example, oxygen atoms are ionized by a 2+1 REMPI transition near 226 nm which provides 2.9 eV of excess energy

above the ionization potential for oxygen of 13.6 eV. While most of this energy is partitioned to the ejected electron due to its small mass, the energy partitioned to the oxygen atom corresponds to a velocity of 20 m/s. The affect of this added velocity depends on the velocity of the oxygen fragment from the dissociation process. For ClO at near 300 m/s, the added velocity results in an experimental error of about 0.6%. If the effect of the ion recoil is such that it cannot be ignored, the only solution is to lower the amount of excess energy placed in the system from the ionization process. One way this can be accomplished is to use two-color REMPI where the resonant state is reached through absorbing photons of one color, and then one photon of another color is absorbed to ionize the fragment. The wavelength of light used to ionize can be chosen so that its energy is enough to barely clear the ionization energy threshold of A, ensuring that KE_{Total} is minimized.

Another cause of slight image blurring which leads to uncertainty in the velocity distribution is the bandwidth of the photodissociation laser. This broadening is very minor for dye laser systems with a bandwidth of about 1 cm^{-1}. For this bandwidth, the velocity resolution is 0.003% at 300 nm. The laser bandwidth is the minimum achievable broadening of the velocity distribution of this instrument.

I. Synthesis of Cl_2O and Production of ClO Radical Beam

Because Cl_2O is a highly reactive and unstable species, it requires careful laboratory synthesis under vacuum. Cl_2O is synthesized under vacuum by the following reaction by the method of Cady.[69] A schematic of the vacuum synthesis of Cl_2O is shown in Figure 18. Cl_2O is formed via the reaction of liquid Cl_2 with powdered HgO shown in Equation 2.11:

$$2Cl_2(l) + HgO(s) \rightarrow Cl_2O(l) + HgCl_2(s) \qquad (2.13)$$

The mercuric oxide (HgO) must be baked in a vacuum oven at 100 - 120°C for at least 4 hours to insure that it is dry. The reaction will not proceed if any moisture is allowed inside the reaction vessel. It is also crucial to use yellow mercuric oxide as it is a finer powder than the red. Small glass beads are added to the reaction vessel to increase the

surface area producing much greater product yield. Cl_2 (Aldrich 99%) is used directly from the cylinder without further purification. The Cl_2 is trapped in an evacuated glass tube cooled with liquid nitrogen. The trap is then warmed in a dry ice/acetone bath to melt the Cl_2. The Cl_2 is then transferred into the evacuated reaction vessel containing mercuric oxide by holding the reaction vessel at the nitrogen temperatures. The reaction vessel is then held in a dry ice/acetone bath for at least eight hours to allow the reaction to proceed, although our experience indicates that the yield is greater if the reaction is allowed to proceed for longer times up to a week. Cl_2O and unreacted Cl_2 are removed from the reaction vessel through vacuum extraction into a trap held in liquid nitrogen. It should be noted that liquid Cl_2O is dark brown while liquid Cl_2 in yellow providing a clear indication of the success of the reaction.

Excess HgO is used so that as much Cl_2 as possible is consumed in the reaction making purification of the Cl_2O much easier. Although Cl_2 contamination was not a concern for the ClO experiments shown in this dissertation because only the oxygen photofragment was imaged, Cl_2 can be easily removed from the Cl_2O using vacuum distillation if pure Cl_2O is required. Although contamination of the Cl_2O sample was not a major concern, excessive Cl_2 in the sample causes problems getting a strong molecular beam of Cl_2O because of the much larger vapor pressure of Cl_2 compared to that of Cl_2O at -78°C (about 10 times higher).

The molecular beam of ClO was formed by the flash pyrolysis of a Cl_2O/He mixture. The Cl_2O was kept at -78ºC to provide an approximately 5% mix in 1 atm of He. The Cl_2O/He sample was introduced into the instrument through a commercially

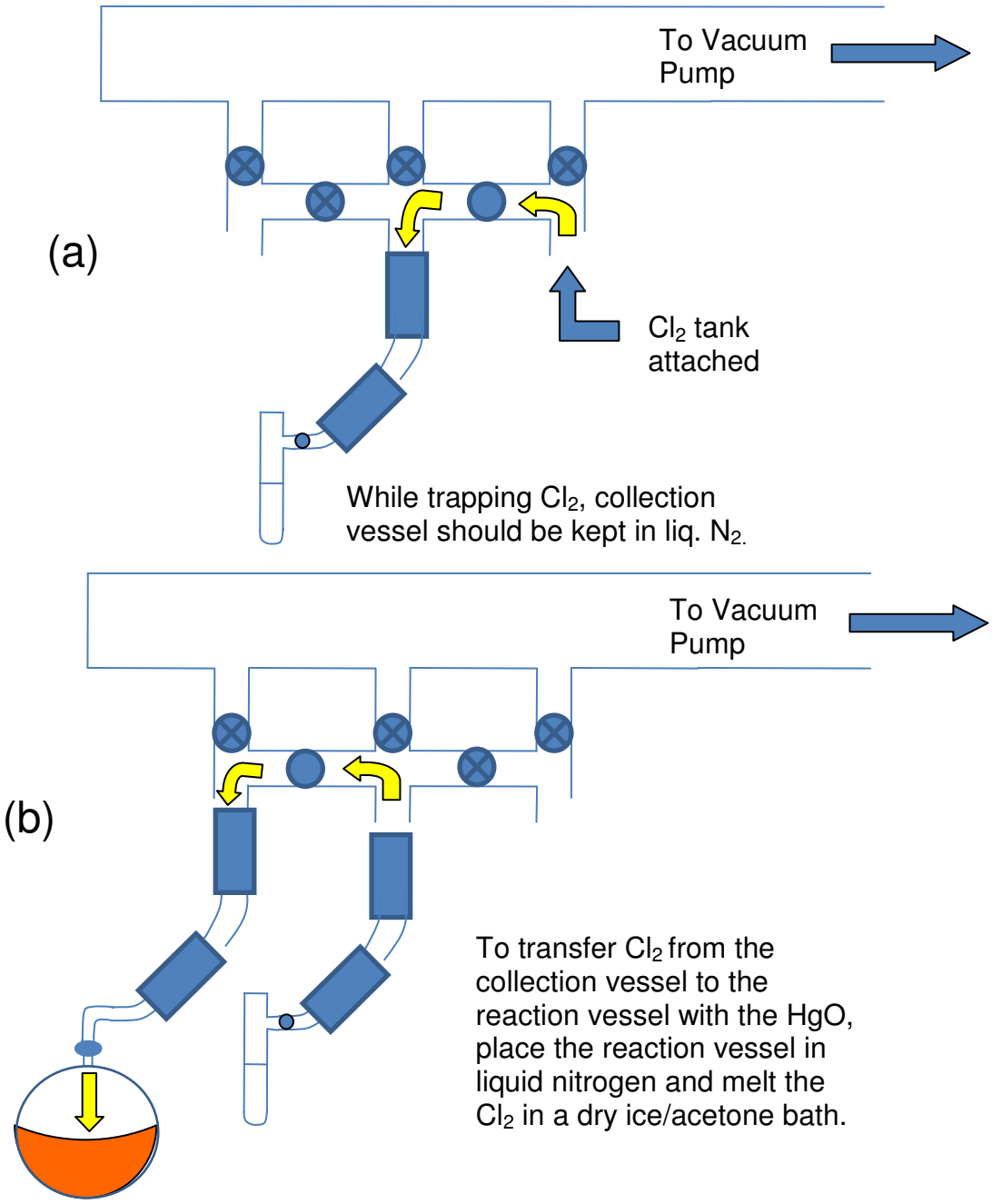

Figure 18: Schematic diagram of Cl_2O synthesis. Panel (a) shows the method of collecting Cl_2 for the reaction by trapping it in a glass vessel kept in liquid N_2. Panel (b) shows the transferring of the Cl_2 from the collection vessel to the round bottom flask that contains HgO and glass beads.

available pulsed valve (Parker Hannifin Series 9) fit with a pyrolytic nozzle assembly. The pulsed valve with the pyrolytic assembly is shown in Figure 19. The active region of the nozzle assembly consisted of a 3 cm long alumina tube wrapped in nickel-chromium alloy wire allowing the tube to be resistively heated to approximately 800 K. The nozzle is then covered in a high temperature ceramic paste (Wale) to ensure even heating throughout the nozzle. This is done by applying a DC current of 4A across a 24 AWG nickel-chromium wire. The endcap and front plate of the assembly are cooled by flowing cold water (~5°C) through the copper tubing that surrounds them. The cooled endcap serves to protect the pulsed valve from the heat of the pyrolysis tube. The cooled front plate modestly cools the molecular beam as it passes through the center bore before expanding into the chamber. We observe ClO rotational temperatures of approximately 100 K following expansion.

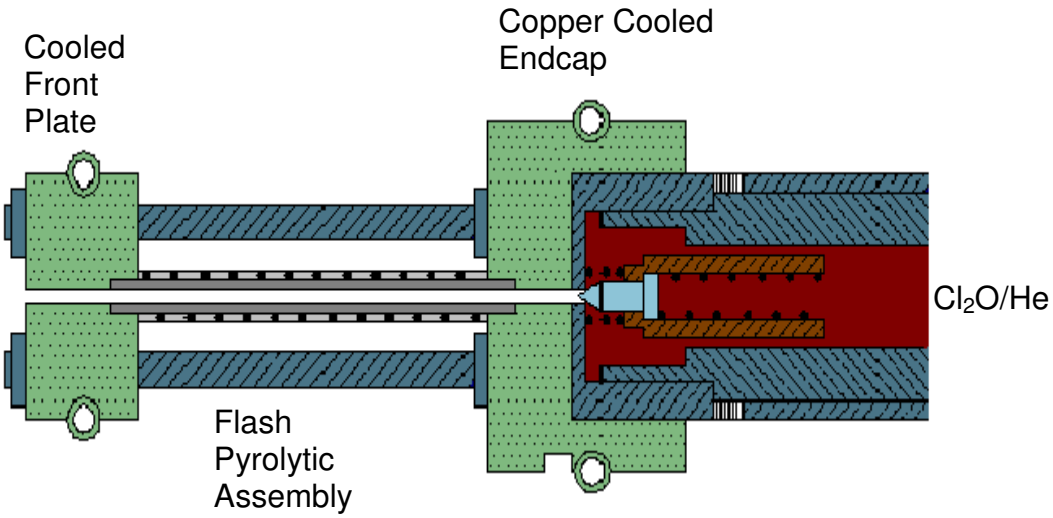

Figure 19: Cross-sectional view of the pyrolytic assembly used to produce a radical beam of ClO through the decomposition of Cl_2O.

J. Production of BrO Radical Beam

The BrO radical molecular beam was generated using a flash pyrolysis technique that uses two pulsed valves and a heated nozzle to react O_3 and gaseous Br_2. Camden *et al.* reported a late-mixing pulsed nozzle to allow the co-expansion into vacuum of two reactive species.[70] Our dual-pulsed valve flash pyrolytic nozzle expands on this idea, combining the dual pulsed valve assembly for late-mixing of reactants with a heated end nozzle to act as a flash kinetic reactor. A similar design has been used by Reisler and co-workers to study CH_2OH radicals; however, their design utilizes a photolytic end nozzle instead of a pyrolytic nozzle as is described here.[71] The products of the reaction are then expanded into vacuum before further reactions can take place. The nozzle assembly will be described briefly here as full design details of the dual-pulsed valve flash pyrolytic assembly used in this experiment can be found in a paper by Kim *et al.* [72]

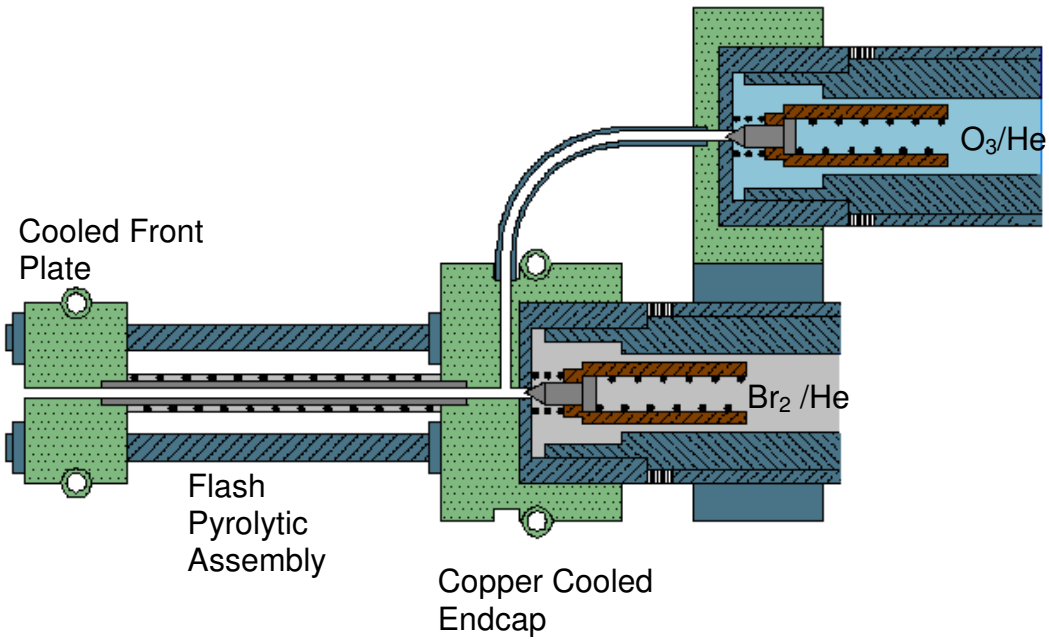

Figure 20: Cross-sectional view of the dual-pulsed valve pyrolytic nozzle assembly used in the production of the BrO radical molecular beam.

The design of the dual pulsed valve assembly is shown in Figure 20. It employs two commercially available pulsed valves (Series 9, Parker Hannifin) attached to a custom built nozzle assembly. Each pulsed valve is seated into its own endcap and secured with screws. The lower endcap is water cooled to protect the pulsed valve from the heat of the pyrolysis nozzle by flowing cold (5°C) water through copper tubing surrounding the endcap. A stainless steel tube connects the upper endcap to a channel cut into the lower endcap. This channel is intersected by a perpendicular channel that extends from the lower pulsed valve allowing the gases to mix before exiting the endcap. The mixed gases then pass into the heated region of the nozzle. The heated nozzle is constructed from an alumina tube (1.0mm I. D., 2.4mm O. D., Scientific Instrument Services, Inc.) wrapped in 24 AWG nickel-chromium wire. The heated region is then covered in a high temperature ceramic paste (Wale) to ensure uniform heating. The optimal length of the nozzle was found to be about 2 cm for the heated region. The alumina nozzle is seated into the front of the lower endcap on one side and into a cooled front plate on the other. The cooled front plate serves to modestly cool the beam before expansion. It also holds the alumina tube straight making certain that the beam is directed correctly into the skimmer.

A strong beam of BrO is dependent on both proper nozzle temperature as well as correct reactant concentrations. The reactant concentrations are controlled using their vapor pressures. In the case of BrO, the reactants used are Br_2 and O_3. The suitable vapor pressure (30 torr) of Br_2 is achieved by holding it in a bubbler at -35°C using a dry ice/acetone slurry. The O_3 is trapped over silica gel (3-6 mm, Fluka) in a bubbler held at -78°C using a dry ice/acetone bath. The bubbler is then warmed to -45°C to attain the correct vapor pressure of O_3 (30 torr). Both gas samples are combined with 760 torr of He, using a single He line split to go into each sample at the same pressure. This is important because any deviation of the total pressures from each line can lead to back flowing of one of the samples into the other which is not only a problem because it will hinder the molecular beam but also because with two reactive species, it could potentially be dangerous.

The nozzle used for BrO production is much shorter than the one used in the ClO experiments. This is because the rate constants of reactions that consume BrO are rather high at the temperatures needed to produce BrO from the O_3/Br_2 reaction. From our kinetic simulations we see that a maximum number density of BrO is achieved using high nozzle temperatures near 700 K and very short residence times of only a few microseconds. By noting where the maximum BrO signal is seen, the proper nozzle temperature is achieved using 24 gauge nickel-chromium wire heated using a DC current of 4.5 A, 8 V.

K. Production of IO Radical Beam

The dual pulsed valve pyrolytic nozzle assembly used in the production of the BrO molecular beam was tried unsuccessfully in the production of an IO beam. Kinetic simulations using various sources of iodine atoms (I_2, CH_3I, CF_3I, and IBr) reacting with ozone were done and showed only modest success at producing IO radicals. The maximum concentrations of the IO produced from these reactions was sufficient for detection by the velocity map ion imaging instrument; however, the IO radical was very short-lived in these simulations. For this reason, we attempted to use very high temperature nozzles that were very short. We hoped that the high temperature would increase the rate constants of the IO production reactions sufficiently, while the short nozzle would have a short enough resident time for the IO radicals to escape recombination reactions. Numerous nozzles of various sizes were tested, each at a variety of temperatures. The 24 gauge nickel-chromium wire cannot survive DC currents above 5 A for more than a few minutes, which limited the temperature of the nozzle. From the kinetic simulations, we chose to try using I_2 and CF_3I as possible iodine atom sources. Unfortunately, no combination of nozzle length and temperature with either iodine atom source produced an IO radical molecular beam.

Because we were unable to produce an IO radical molecular beam using a pyrolytic nozzle, we chose to try a photolytic reaction instead. I_2 was chosen as an ideal photolytic precursor for producing iodine atoms. I_2 is also very easy to work with as it is

a solid at room temperature and can be easily and safely transferred into a bubbler for use in the experiment. It is also an ideal choice because two iodine atoms are released with each photolysis, and there are no unwanted radicals produced that could interfere with the production of IO. A mixture of I_2 and O_3 in Helium, each introduced from separate solenoid valves, was irradiated in a quartz tube (0.1 cm I.D.) by the 248 nm output of an excimer laser (GAM Laser, EX10). It is important to note that based on the relative cross sections at 248 nm, it is photolysis of ozone which initiates the reactions with only minor contribution from I_2 photolysis. The resulting bimolecular reactions generate IO during the transit time to the nozzle exit.

New kinetic simulations were done assuming the use of I_2 and O_3 as reactants in the photolysis tube. In these simulations we assume an initial concentration of iodine and oxygen atoms based on the Excimer laser power, wavelength of laser output, the I_2 and O_3 vapor pressures used (~2 torr for I_2 and ~30 torr for O_3), and the absorption cross sections of the species at 248 nm. For our simulations we assume an initial concentration of iodine atoms of 5.57×10^{14} molecules/cm^3 and an initial concentration of oxygen atoms of 1.06×10^{17} molecules/cm^3. Using these simulations, it was seen that the maximum IO concentration was achieved when the bubbler of O_3 trapped over silica gel was held at -45°C, giving a vapor pressure of about 30 torr. Figure 21 shows the concentrations of IO as a function of time using these optimal conditions. The simulations are done using reactions and rate constants shown in Table 2. The residence time of the reacting species inside the quartz tube before expansion into vacuum is about 10 μs. At this time, the simulation shows the IO concentration to be about 5.0×10^{15} molecules/cm^3.

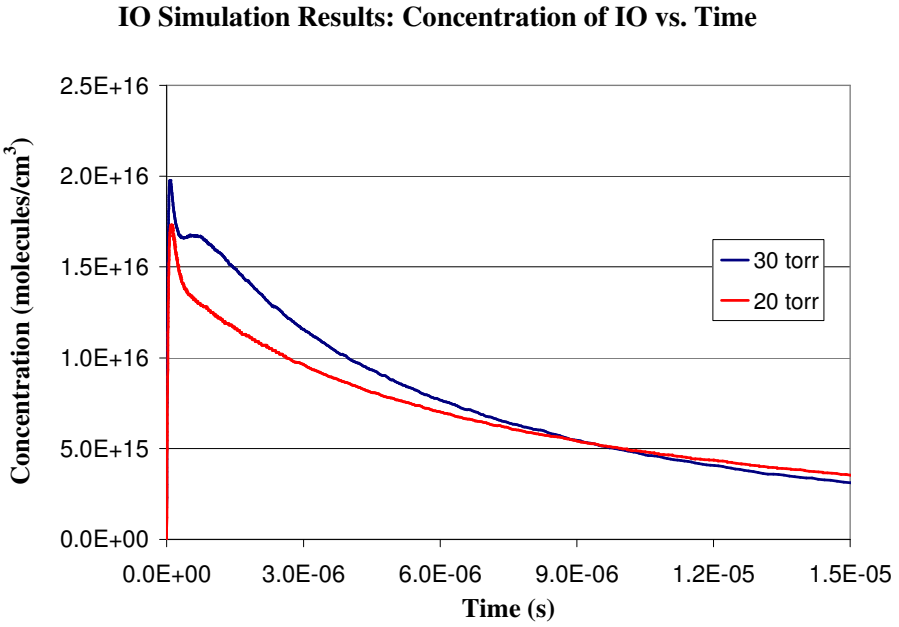

Figure 21: Kinetic simulation data for the concentrations of I, O, and IO species as a function of time assuming T = 298K, and the initial concentrations of I and O are 5.57 x 10^{14} molecules/cm^3 and 1.06 x 10^{17} molecules/cm^3, respectively. These are found to be the optimal conditions for producing the maximum amount of IO.

Table 2: Reactions and rate constants used in kinetic simulations for the production of the IO radical. Units for Rxn Order 2 and 3 are: cm^3/molecule·s, and cm^6/$molecule^2$·s, respectively.

	Reaction	Rxn Order	Rate Constant at 298K	Reference
1	$CF_3I + O \rightarrow CF_3 + IO$	2	6.51×10^{-12}	73
2	$CF_3I + CF_3 \rightarrow C_2F_6 + I$	2	3.01×10^{-16}	74
3	$CF_3I + I \rightarrow CF_3 + I_2$	2	3.39×10^{-11}	75
4	$I_2 + O \rightarrow I + IO$	2	1.2×10^{-10}	76
5	$O_3 + I \rightarrow O_2 + IO$	2	1.28×10^{-12}	76
6	$IO + O \rightarrow O_2 + I$	2	1.4×10^{-10}	77
7	$IO + IO \rightarrow IO_2 + I$	2	3.8×10^{-11}	77
8	$IO + IO \rightarrow O_2 + I + I$	2	5.2×10^{-11}	78
9	$IO + IO \rightarrow O_2 + I_2$	2	5.0×10^{-12}	79
10	$O_3 + IO \rightarrow 2O_2 + I$	2	1.2×10^{-15}	80
11	$O_3 + IO \rightarrow O_2 + IO_2$	2	2.3×10^{-16}	80
12	$I + I \rightarrow I_2$	3	1.9×10^{-32}	81

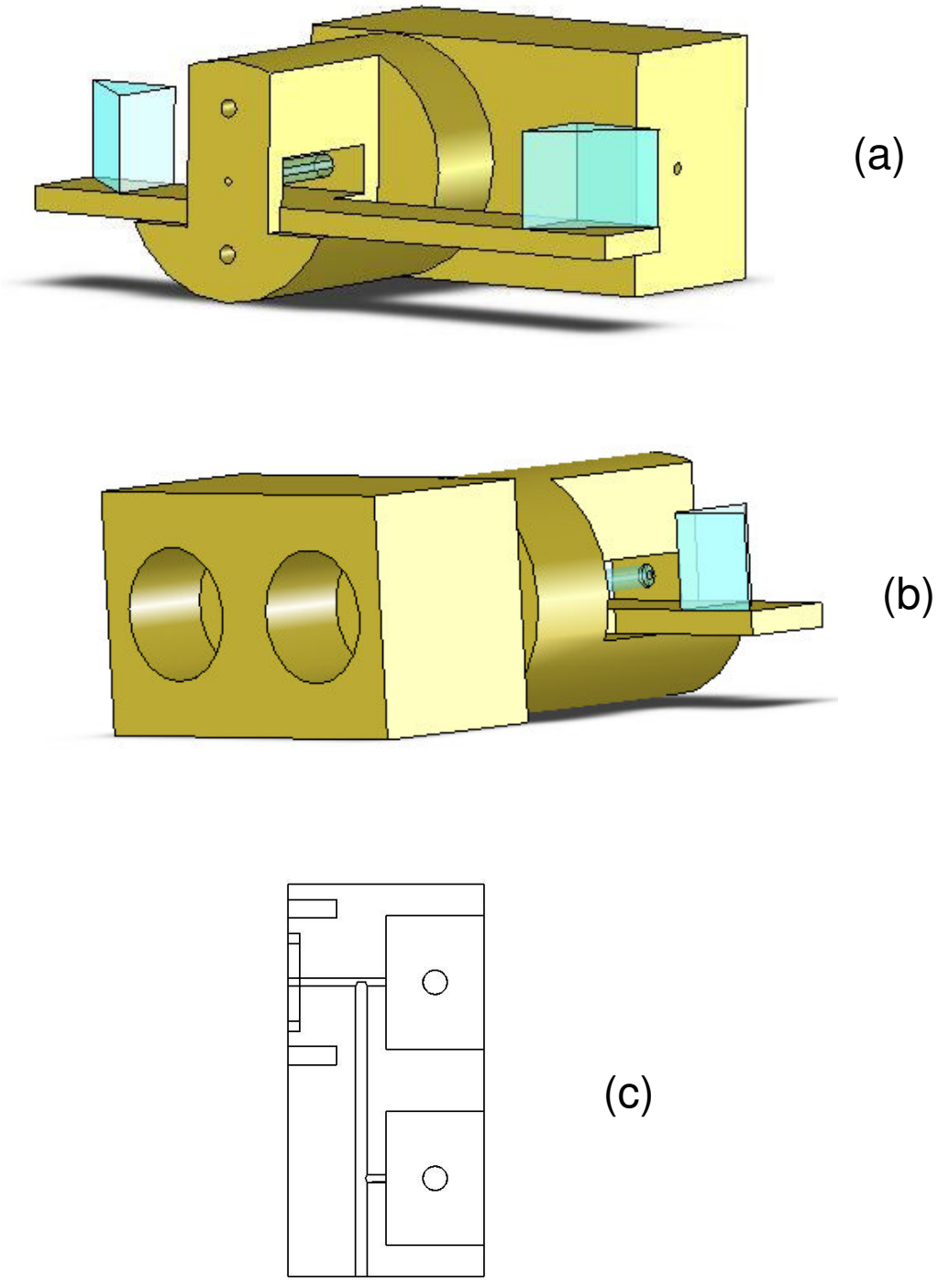

Figure 22: Front (a) and back (b) views of the dual-pulsed valve photolytic nozzle used in the production of the IO radical molecular beam. Cross-sectional view (c) of the channels cut in the block that holds the pulsed valves.

The basic design of the new pulsed valve assembly is similar to that used to produce the BrO radical molecular beam. The design of this dual pulsed valve assembly is shown in Figure 22. The pulsed valves are seated in a solid brass block with 1 mm diameter channels bored to provide a mixing region for the reactive species. The channels can be seen in the cross-section view in Figure 22. The long vertical channel was constructed by first drilling a 2 mm bore from the top of the brass block connecting the two short channels from each pulsed valve opening. The end of the long channel is then filled and sealed up to the point of the first horizontal channel. After mixing, the gases expand into a 1 mm I. D., 3 mm O. D. quartz tube. Because of the design of the vacuum chamber, the excimer laser beam enters from behind the pulsed valve assembly. For this reason, we use one 90° quartz prism to direct the beam through the quartz tube. The other prism is used to direct the light back out of the chamber to aid in alignment through the quartz tube. The rapid self-reaction of IO radicals requires short transit times which can be achieved by irradiation close to the exit of the quartz nozzle.

Figure 23 shows images taken that show that the ring associated with IO is only present when both O_3 and I_2 are present, the 248 nm photolysis laser is on to initiate the reaction. In panels (d) and (e), it is also shown that the IO ring is also only present when the 455 nm photolysis and the 303 nm ionization beams are present. It was also noted that there was no signal or IO ring when the ionization laser is moved off-resonance, although there is not a panel in Figure 23 depicting this. The panels in Figure 23 were taken sequentially. Panel (a) shows that when all the lasers and pulsed valves are on, the image shows rings associated with I_2 photodissoiation and with IO photodissociation. Panel (b) shows an image with no O_3, although the O_3 pulsed valve is still allowed to open, introducing pure helium into the nozzle. Panel (c) shows the result of the excimer being turned off, O_3 and I_2 are present, and both the 304 nm and 455 nm lasers are firing. Panel (d) shows the image when only the 455 nm light is absent. Only the center spot from entrained iodine atoma and a very weak ring associated with I_2 photodissociation at 303 nm is seen in this image. Panel (e) was collected with only the 303 nm laser off. As expected, there is no signal observed. Panel (f) was collected after the series of panels

described to show that when everything is turned back on, the IO ring reappears. In between the collection of each panel, the presence of the IO ring was observed before moving on to the next settings.

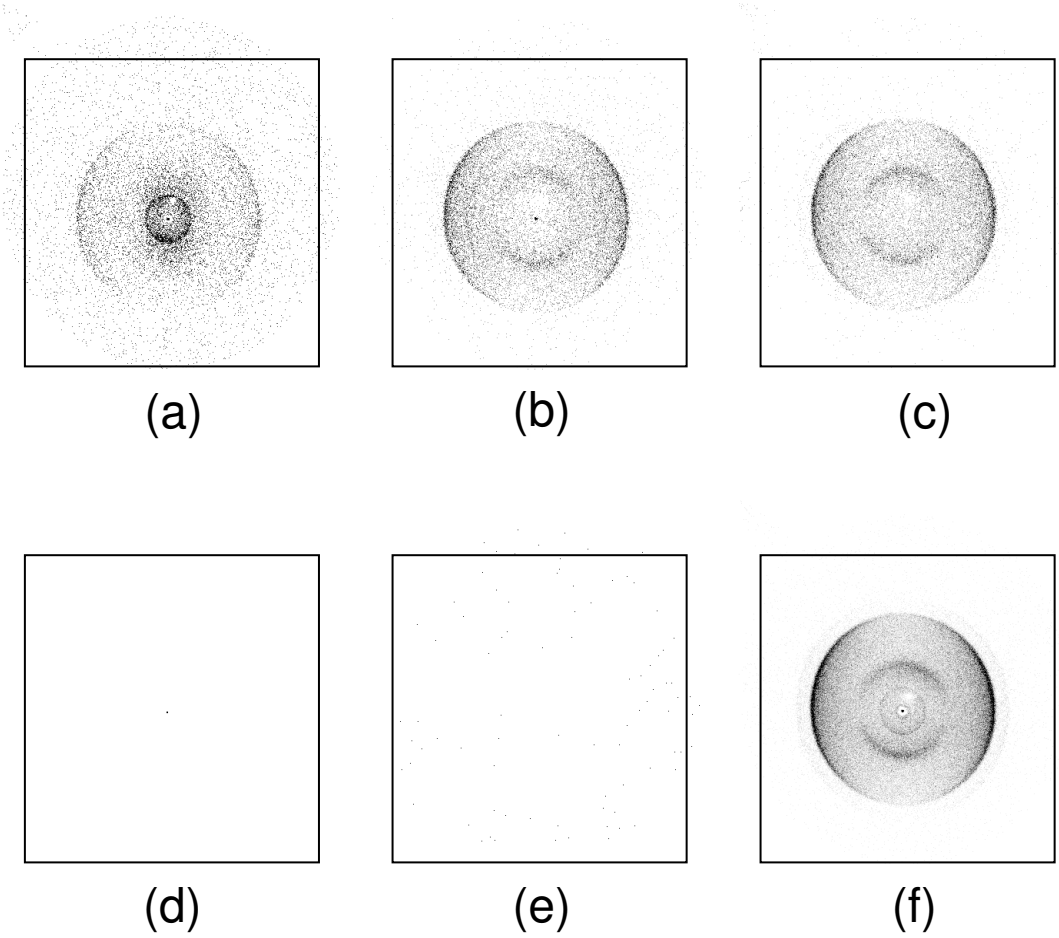

Figure 23: Images showing IO beam production. Panel (a) shows an image with all lasers and pulsed valves on, showing the IO feature. In all subsequent panels, O_3 and I_2 pulsed valves are on, and all lasers (248 nm, 303 nm, and 455 nm) are on except what is noted. Panel (b) was collected with O_3 off. Panel (c) was collected with 248 nm laser off. Panel (d) shows an image with the 455 nm laser off. Panel (e) was collected with the 303 nm laser off. Panel(f) shows an image with all lasers and pulsed valves on.

CHAPTER III

DIRECT DETERMINATION OF THE BOND DISSOCIATION ENERGY OF IO*

A. Introduction

The thermochemistry of IO, surprisingly, has been the subject of some controversy. The need for a reliable IO bond dissociation energy (BDE) is the result of IO reactions that are close to thermoneutral. For example, the IO + BrO reaction has 4 thermodynamically accessible channels[82]:

IO + BrO	→ Br + OIO	$\Delta H \leq 0$ kcal/mol	(3.1)
	→ Br + I + O_2	$\Delta H = -4.1 \pm 2.6$ kcal/mol	(3.2)
	→ I + OBrO	$\Delta H = 5.5 \pm 8.6$ kcal/mol	(3.3)
	→ IBr + O_2	$\Delta H = -46.5 \pm 2.6$ kcal/mol	(3.4)

By comparison, the thermochemistry of the other halogen oxides, ClO and BrO, can be derived from Birge-Sponer[83] extrapolation using the vibronic levels of the bound A $^2\Pi_{3/2}$ state.[84] Since only the lowest 6 vibrational levels are clearly resolved in the IO A $^2\Pi_{3/2}$ - X $^2\Pi_{3/2}$ absorption spectrum, due to strong perturbations induced by spin-orbit coupling to low lying repulsive electronic states[85], there is considerable uncertainty associated with a Birge-Sponer extrapolation. Predissociation of the (1-0) band of the A $^2\Pi_{3/2}$ state provides a rigorous upper bound to the ground state bond dissociation (BDE) of <62.8 kcal/mol. Birge-Sponer extrapolation of the lowest 6 vibrational levels in the A $^2\Pi_{3/2}$ state by Vaidya and co-workers yielded a BDE of 43.8±4.6 kcal/mol.[86] Subsequent studies using a similar spectroscopic analysis have reported comparable values.[84,87,88]

---

* Reproduced in part from "Ion imaging study of IO radical photodissociation: Accurate bond dissociation energy determination" K. S. Dooley, J. N. Geidosch, and S. W. North, *Chem. Phys. Letts.*, **457**, 303 (2008). Copyright 2008 Elsevier.

Phillips and Sugden measured IO emission as a function of temperature in an I_2 seeded H_2/O_2 flame.[89] The results were interpreted in terms of the equilibrium reaction,

$$I + O + M \leftrightarrow IO + M \qquad (3.5)$$

and on the basis of variation of the equilibrium constant with temperature the authors deduced a much higher IO BDE value of 57±6 kcal/mol. Molecular beam scattering measurements of the $O(^3P) + ICl \rightarrow IO + Cl$ reaction yielded a value of 53±3 kcal/mol based on statistical modeling of the product kinetic energy distribution.[90] Subsequent molecular beam studies by Buss *et al*. recommended a slightly larger value of 55±2 kcal/mol.[91,92] Recently, Peterson *et al*. reported an IO BDE of 54.2±0.6 kcal/mol based on high-level *ab initio* calculations using both direct methods and employing ionization energies and ion cycles.[93] The authors also reported an experimental value derived from the measured $ClO + IO \rightarrow OClO + I$ reaction enthalpy[94] and an improved value for the OCl-O BDE[95] yielding an IO BDE of 55.3±0.5 kcal/mol in reasonable agreement with calculations. There has also been a recent paper by Kaltsoyannis and Plane that report quantum chemical calculations on various atmospherically relevant iodine containing species including IO.[96] A summary of the previous measurements and calculations of the bond dissociation energy can be found in Table 3.

Table 3: IO bond dissociation energy determinations from past measurements.

Study	Method	BDE (kcal/mol)
Gaydon (1948)	Birge-Sponer Extrapolation	46±5
Huber and Herzberg (1979)	Birge-Sponer Extrapolation	43
Radlein et. al. (1975)	Cross Molecular Beam Study of ICl + O → IO + Cl	53
Reddy et al (1989)	Fitting 5 vibrational lines (bad)	58.64±.3
Ruscic and Berkowitz (1994)	Mean of Radlein and Gaydon	50±5
IUPAC (2000)	Based on kinetic data for IO ClO reaction by Bedjanian (1997)	57.4
Peterson and coworkers (2005)	Theory	54.31±1
Kim et. al. (2006)	Calculated based on ΔfH(BrO) and kinetic data for I + BrO → IO + Br	55.8±1

Velocity-map ion imaging is a powerful method for the direct determination of accurate bond dissociation energies.[97,98,99] Wrede *et al*. have shown that for jet-cooled closed-shell species, spectroscopic accuracy is possible in the case of IBr. We have recently reported BDE values for the ClO and BrO radicals of 63.45±0.06 kcal/mol and 55.9±0.1 kcal/mole respectively using photodissociation ion imaging.[100] In this chapter, the study of halogen oxide photodissociation dynamics is extended to include IO which, to our knowledge, has not been investigated using the molecular beam method.

B. Experimental Details

Experiments were performed using a velocity-map ion-imaging apparatus that has been described in detail in Chapter II. The dissociation beam at 454.9 nm,

corresponding to the bandhead of the 1-0 transition, was generated using the Exciton dye Coumarin 450 in the LAS laser system. No frequency doubling was needed. The probe beam was generated by using the PDL laser operating on the dye Rhodamine 640 followed by frequency doubling. No scanning of the Doppler profile of the REMPI transition was needed due to the broad bandwidth of the laser and the slow velocity of the iodine fragments. The iodine atoms I($^2P_{3/2}$) were probed using 2+1 REMPI transitions at 304.67 nm ($5p\ ^2P_{3/2} \rightarrow 6p\ ^2D_{5/2}$).[101] The IO molecular beam was produced using the dual pulsed valve photolytic assembly described in Section J of Chapter II. Ion optic voltages in order starting at the optic closest to the skimmer are: 2000 V, 1784V, and 1560V.

C. Results and Discussion

The photodissociation of IO at 454.9, corresponding to the A $^2\Pi_{3/2}$ - X $^2\Pi_{3/2}$ (1-0) bandhead region, was selected for two reasons. Firstly, the (v′,0) bands with v′=0-5 of the A $^2\Pi_{3/2}$ - X $^2\Pi_{3/2}$ transition have been studied using cavity ring-down spectroscopy and the (1-0) band was shown to be strongly predissociated.[102] Newman *et al.* determined a predissociation lifetime of 0.88 ps implying that the photofragment angular distribution should be highly anisotropic near the bandhead.[103] In addition, the (1-0) band represents a compromise between the higher cross section of the (4-0) band and the increased sensitivity to the available energy closer to threshold.

The upper panel in Figure 24 shows a typical image (left) and reconstruction (right) arising from the photodissociation laser at 454.9 nm and the probe laser at 304.6 nm *with the 248 nm source laser off*. Only features consistent with I_2 photodissociation at 454.9 nm and 304.6 nm are observed in the image. The lower panel in Figure 24 shows raw and reconstructed I($^2P_{3/2}$) images *with the 248 nm source laser on*. An additional ring, corresponding to 454.9 nm photodissociation of IO to yield the I($^2P_{3/2}$) + O(^3P_J) channel is clearly observed. The feature was not observed with either the probe or photodissociation laser blocked, either pulsed valve off, or with the probe laser tuned off-resonance. In addition, the appearance of the IO signal is sensitive to the

photodissociation wavelength. At shorter photodissociation wavelengths, beyond the bandhead, the signal is lost while at longer wavelengths the anisotropy is first observed to decrease significantly before the signal is finally lost. A similar effect has been recently reported, and its origin discussed, in the case ClO photodissociation.[103]
Figure 25 shows the speed distribution (closed circles) derived from the images shown in the lower panel of Figure 24. The upper panel shows an expanded region from 900 m/s to 1200 m/s. The two features in the speed distribution are associated with I_2 photodissociation.[104,105] The peak at 948 m/s is due to I_2 photodissociation at 454.9 nm to give $I(^2P_{3/2}) + I(^2P_{3/2})$ fragments. We also observe the minor $I(^2P_{3/2}) + I(^2P_{1/2})$ channel which is not shown but can be seen in the raw and reconstructed images. The peak at 1100 m/s is due to I_2 photodissociation at the probe wavelength of 304.67 nm to give $I(^2P_{3/2}) + I(^2P_{1/2})$.[106] The FWHM of these peaks correspond to a $\Delta v/v \sim 0.03$ which is close to the instrumental resolution and these two peaks provide an accurate pixel-speed calibration of the images. The lower panel shows an expanded region to highlight the feature, centered at 240 m/s, due to IO photodissociation at 454.9 nm. The FWHM of the feature associated with the $I(^2P_{3/2}) + O(^3P_J)$ channel arising from IO photodissociation at 454.9 nm is approximately 24 m/s and is the result of several factors. The additional kinetic energy imparted to the iodine atom due to the ionization process is 3.4 m/s.[45] It is also difficult to resolve spin-orbit states of the coincident oxygen atoms. The effect of the unresolved oxygen fine-structure distribution will be discussed below.

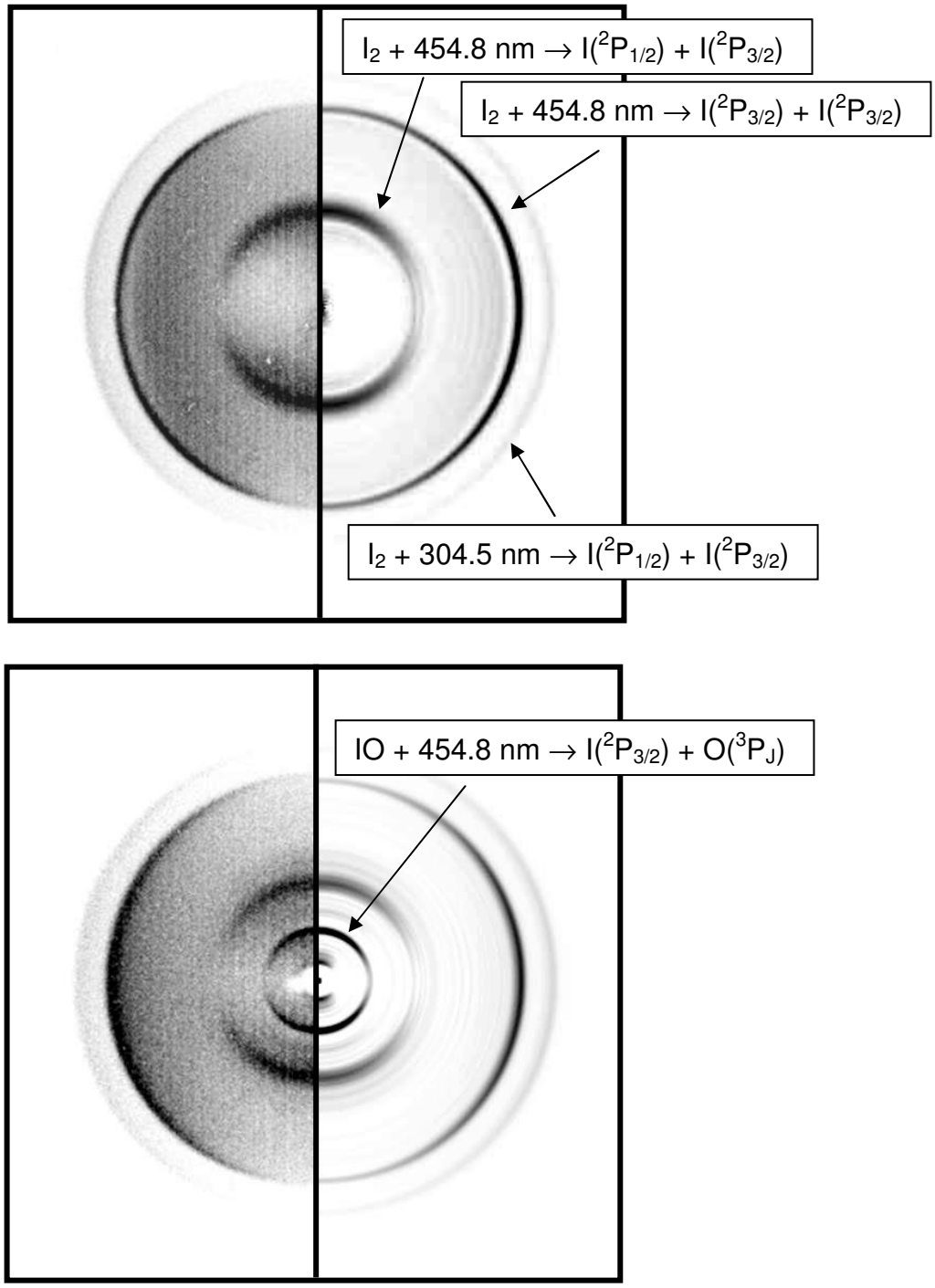

Figure 24: Labeled raw and reconstructed images of the $I(^2P_{3/2})$ fragment. Upper panel: raw $I(^2P_{3/2})$ ion image (left) and reconstruction (right) collected with the source laser off. Lower panel: raw $I(^2P_{3/2})$ ion image (left) and reconstruction (right) collected with the source laser on.

In Figure 25 the solid lines represent the forward-convolution simulation based on energy conservation,

$$h\nu + E_{v,J,e}^{IO} - D_0^0(IO) = E_{trans}^{total} + E_e^I + E_e^O \ , \qquad (3.6)$$

where $h\nu$ is the energy of the dissociation photon, $D_0^0(IO)$ is the bond energy of IO, E_e^I and E_e^O are the spin-orbit energies of I and O, and $E_{v,J,e}^{IO}$ is the initial internal energy of the IO radical.

An assumed statistical distribution of oxygen fine-structure states, *i.e.* $O(^3P_2)$: $O(^3P_1)$: $O(^3P_0)$ = 0.625:0.375:0.125, provides a reasonable forward-convolution fit to the observed width of the speed distribution. We adjust a single value for the bond dissociation energy to provide the best forward-convolution fit to the $I(^2P_{3/2})$ + $O(^3P_J)$ channel shown as the solid line in the lower panel of Figure 25. We find a value of 54.9 kcal/mol for the IO BDE provides the best fit to the data. The width of each spin-orbit feature was fixed as the instrumental response function broadened by the additional kinetic energy imparted from the ionization process. Our assumption of a statistical distribution of oxygen fine structure states is consistent with previous measurements of the ClO and BrO oxygen spin orbit state distributions. If no $O(^3P_2)$ fragments were formed in the dissociation the BDE would be overestimated by approximately 0.4 kcal/mol. Iterative adjustment of the spin-orbit branching ratios to obtain the best fit provided only marginal improvement. In all cases the best fits required a dominant contribution from the $O(^3P_2)$ and lesser contributions from $O(^3P_1)$ and $O(^3P_0)$ states. Fits employing only a single oxygen spin state were markedly worse.

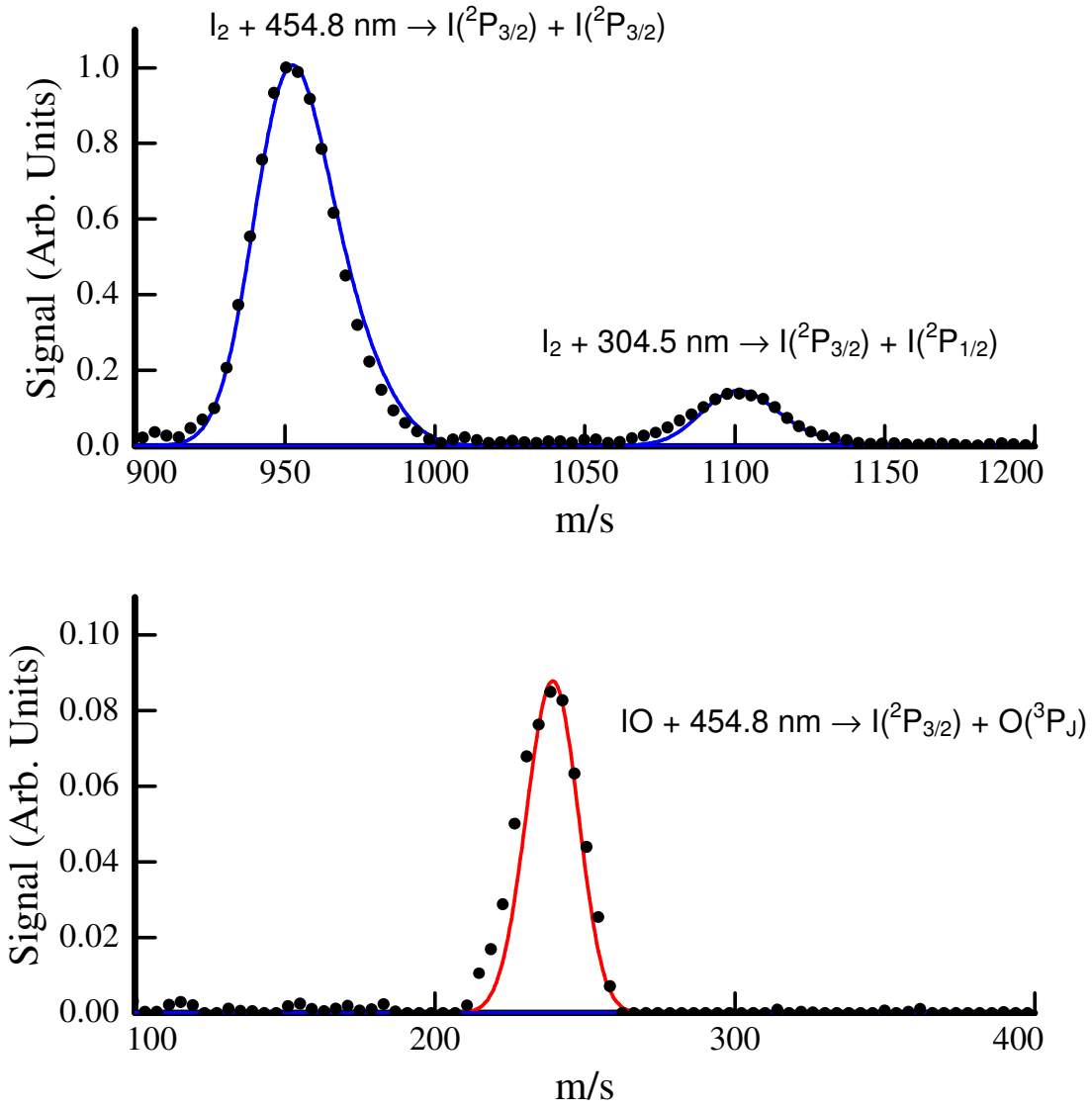

Figure 25: Speed distributions derived from $I(^2P_{3/2})$ images with the source laser on (closed circles). For clarity the relevant regions of the speed distribution are expanded and the identities of the peaks are clearly labeled. The solid lines are forward-convolution fits to the speed distribution.

In the following section, we address possible sources of experimental error arising from uncertainties in IO internal energy, wavelength calibration, the pixel to speed scaling, and ionization process. We conclude that these represent minor effects in the present experiment and do not alter the reported value or error bounds. Given the resolved nature of the bound-bound transitions in the excitation step, the role of spin-orbit or vibrationally excited IO photodissociation is minimal. In addition, such initial internal energy would be resolved in the speed distribution and is not observed. Since we excite near the rotational bandhead we estimate that the parent rotational energy is <0.1 kcal/mol. Any error in the photon energy of the dissociation laser has a direct effect on the derived bond dissociation energy. The dissociation wavelength was calibrated using a Cu-Ne hollow cathode lamp. An unlikely error of 0.1 nm in the wavelength would only change the derived bond energy of IO by ±0.02 kcal/mol. The pixel to speed scaling factor, which is critical in providing speeds from the measured images was determined accurately by fitting the data arising from I_2 photodissociation at two wavelengths using the accurate bond dissociation energy for I_2.[107] We believe that any uncertainty caused by scaling factor is less than 0.6% leading to errors of only 1.5 m/s in the speed of I fragments associated with IO photodissociation and, therefore, a negligible difference in derived BDE. Although the I($^2P_{3/2}$) fragment speeds are affected by excess kinetic energy imparted to the cation during the 2+1 REMPI process, this effect will not change the peak positions, but would only contribute to the observed width of the peaks. Given the sources of errors and the sensitivity of the measurement to the A $^2\Pi_{3/2}$ threshold we believe a conservative estimate of the uncertainty in the bond dissociation energy is $54.9\ ^{+0.2}_{-0.4}$ kcal/mol. This value is within the error bounds of previous IO flame studies (57 ± 6 kcal/mol)[89] and molecular beam studies (53 ± 3 kcal/mol and 55 ± 2 kcal/mol)[90, 91, 92] and in excellent agreement with a more recent calculated value by Peterson of 55.2 ± 0.5 kcal/mol.[108]

The photofragment angular distribution was fit according to[109]

$$I(\theta) = \frac{1}{4\pi}[1 + \beta P_2(\cos\theta)], \qquad (3.7)$$

where β is the spatial anisotropy parameter which is +2 for a purely parallel transition ($\Delta\Omega$=0) and –1 for a purely perpendicular transition ($\Delta\Omega$=±1), $P_2(\cos\theta)$ is the second Legendre polynomial, and θ is the angle between the fragment recoil direction and laser polarization direction. Using pBASEX, we find a best-fit anisotropy parameter of 1.8 ± 0.1 for the I($^2P_{3/2}$) + O(^3P_J) channel. This value is consistent with the parallel $^2\Pi_{3/2} - X\ ^2\Pi_{3/2}$. In a recent article, Kim *et. al.* studied the change in the photofragment anisotropy as a function of excitation wavelength within vibrational bands of ClO. [103] The observation of stronger anisotropy near the bandhead and more isotropic distributions for higher rotational levels was described using the treatment of Mukamel and Jortner.[110] Because the measurement anisotropy parameter for IO photodissociation in the present experiments is nearly limiting, we conclude that we are exciting near the bandhead of the 1-0 vibrational transition. This provides further confirmation of the dissociation wavelength, and increases our confidence that we are observing only the lower rotational states of IO.

D. Summary

We have studied the wavelength-dependent photodissociation dynamics of expansion-cooled IO radical using velocity map ion imaging. This study represents the first reported molecular beam study of the IO radical. Based on the measured photofragment speed distribution following excitation at 454.9 nm we have directly determined the ground state bond energy of IO to be $D_0^0(IO) = 54.9\ ^{+0.2}_{-0.4}$ kcal/mol. Using thermochemical constants of I and O ($\Delta H_f^{0K}(O) = 58.98 \pm 0.02$, $\Delta H_f^{298K}(O) = 59.55 \pm 0.02$, $\Delta H_f^{0K}(I) = 25.61 \pm 0.01$, $\Delta H_f^{298K}(I) = 25.52 \pm 0.01$, all values given are in kcal/mol)[111], our determined $D_0^0(IO)$ corresponds to a 298 K heat of formation of $\Delta H_f^{298}(IO) = 29.2\ ^{+0.4}_{-0.2}$ kcal/mol. This measurement reduces the uncertainty of this value and hence other thermodynamic values that rely on the IO heat of formation. We are

confident that this study will aid in the improvement of atmospheric modeling particularly in the marine boundary layer where IO is especially relevant.

Kim *et al.* recently studied the photodissociation of BrO and measured the bond dissociation energy. Given the value for the heat of formation of BrO at 298K ($\Delta_f H^\circ(BrO) = 29.5 \pm 0.1$ kcal/mol) determined in that work and the forward and reverse rate constants determined by Bedjanian *et al*[112, 113] for the reaction

$$Br + IO \underset{k_r}{\overset{k_f}{\leftrightarrow}} BrO + I \qquad (3.8)$$

$\Delta_f H^\circ(IO)$ at 298K was calculated to be 29.5 kcal/mol, which is within the error bounds of the value determined in the current work.

CHAPTER IV

PREDISSOCIATION DYNAMICS OF ClO

A. Introduction

It is well established that halogen oxides are important intermediates in the catalytic destruction of stratospheric ozone.[114, 115, 116] These species are also ideal benchmark systems for open-shelled photodissociation dynamics, particularly the comparison of experiment and theory, for several reasons; their electronic spectroscopy is well studied, both atomic fragments can be probed using state-selective ionization, and diatomic molecules are amenable to interrogation using high-level *ab initio* theory. A recent study of the state-selected photodissociation of OH ($A\ ^2\Sigma^+$) highlights the progress in describing such systems.[117,118]

The electronic spectroscopy of ClO, in particular transitions between the bound $X\ ^2\Pi_{3/2}$ and $A\ ^2\Pi_{3/2}$ states, has been well studied.[119,120,121,122,123] Vibronic transitions to bound levels of the $A\ ^2\Pi_{3/2}$ state are responsible for resolved bands at wavelengths between 316 nm and the dissociation threshold at 263.01±.01 nm. At wavelengths shorter than 263 nm the spectrum is characterized by a broad continuum that terminates near 220 nm, a manifestation of the continuity of the Franck-Condon intensity involving the $A\ ^2\Pi_{3/2}$ state .

There have been two recent *ab initio* investigations of the ClO excited state potentials. Lane *et al.* employed large Dunning basis sets and the complete active space self-consistent field (CASSCF) method to calculate the ground and excited state potentials of ClO.[124] In an independent study, Toniolo *et al.* used a multiconfigurational SCF plus CI method to calculate the ClO excited states. [125] A focus of both studies was to gain an understanding the origin modeling of the vibrational-dependent predissociation rates of the $A\ ^2\Pi$ state. Because it is a small, open-shelled species, it makes accurate theoretical calculations challenging, but possible. For example, one challenging aspect is that there are 17 calculated unbound electronic states that cross the

A $^2\Pi_\Omega$ and couples it to the X $^2\Pi_\Omega$ state products $Cl(^2P_J) + O(^3P_J)$. [126] Figure 26 shows a schematic of the potential energy surfaces of ClO. Below the $O(^1D_2)$ threshold, the $A(^2\Pi_{3/2})$ state will predissociate via one of the repulsive states that crosses it leading to dissociation to one of six possible asymptotic states.

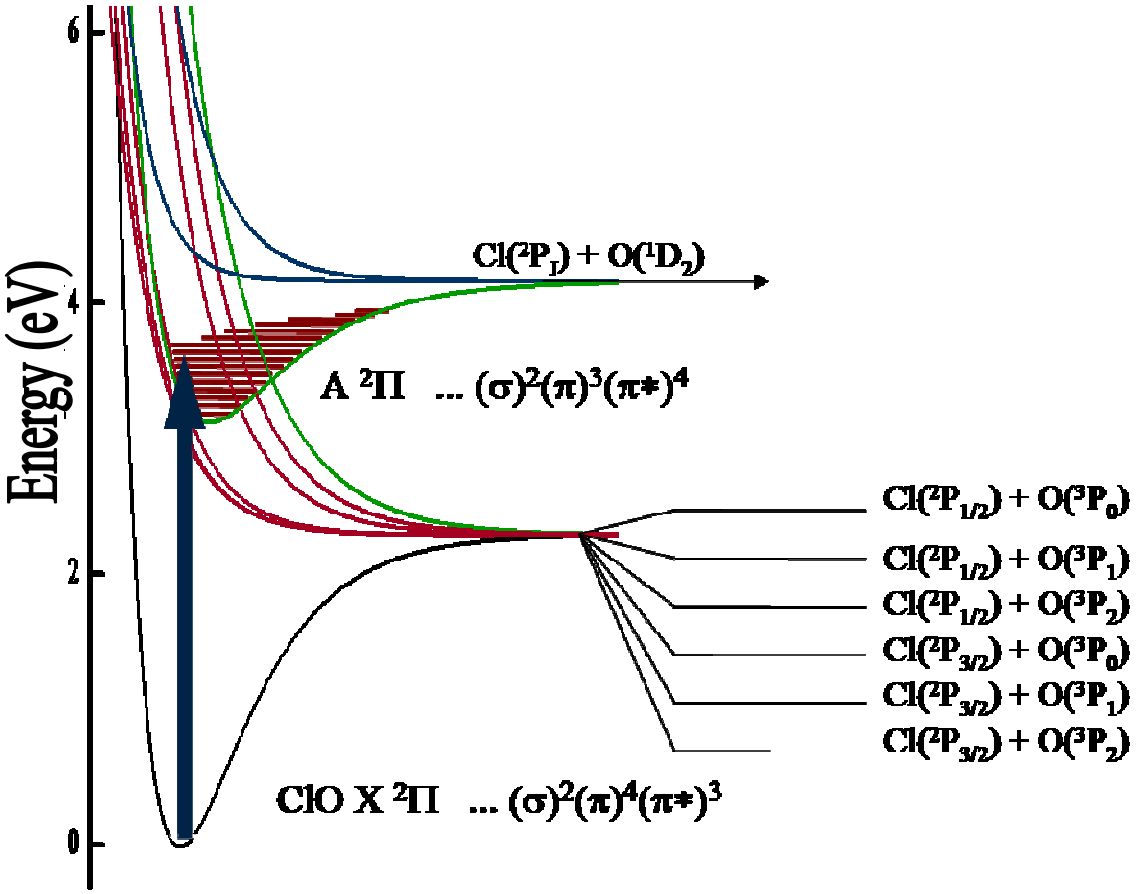

Figure 26: Schematic diagram of the predissociation of ClO.

There have been several recent experimental studies of ClO photodissociation in the continuum region,[127,128,129] near the O(^{1}D) threshold,[129,130,131] and below the O(^{1}D) threshold.[129,132] Most of these studies focused on assessing the relative importance of the O(^{1}D) and O(^{3}P) product channels. Below the dissociation threshold of the $A\ ^2\Pi_{3/2}$ state, there are six correlated fine-structure states that are energetically accessible:

$$ClO(X\ ^2\Pi_{3/2}) \rightarrow ClO(A\ ^2\Pi_{3/2}) \rightarrow Cl(^2P_{3/2}) + O(^3P_2) \quad (4.1)$$

$$\rightarrow Cl(^2P_{3/2}) + O(^3P_1) \quad (4.2)$$

$$\rightarrow Cl(^2P_{3/2}) + O(^3P_0) \quad (4.3)$$

$$\rightarrow Cl(^2P_{1/2}) + O(^3P_2) \quad (4.4)$$

$$\rightarrow Cl(^2P_{1/2}) + O(^3P_1) \quad (4.5)$$

$$\rightarrow Cl(^2P_{1/2}) + O(^3P_0) \quad (4.6)$$

Recently Kim *et al.* examined the v′-dependent predissociation of ClO below the O(^{1}D) threshold and reported product state branching ratios.[132] Although fine-structure distributions averaged over the coincident fragment state provide considerable insight, the correlated fine-structure distributions are often far more revealing. The observed correlated branching ratios measured by Kim *et al*. were non-statistical and highly dependent on the initial $A\ ^2\Pi_{3/2}$ vibrational state (v′=6-11). Figure 27 is an illustration of the correlated state branching ratios of the 11-0 band. The numbers inside the boxes indicate the branching for each individual channel, while the bars along the edges show the overall branching across an atomic state. The image on the right is simulated data in the case that the dynamics are statistical. The image on the right is the measured data for the 11-0 band. The measured branching appears statistical at the state averaged level but is highly structured at the correlated level. An advantage of ion imaging is that we are able to measure the correlated branching ratios which show that the dynamics are not in fact statistical.

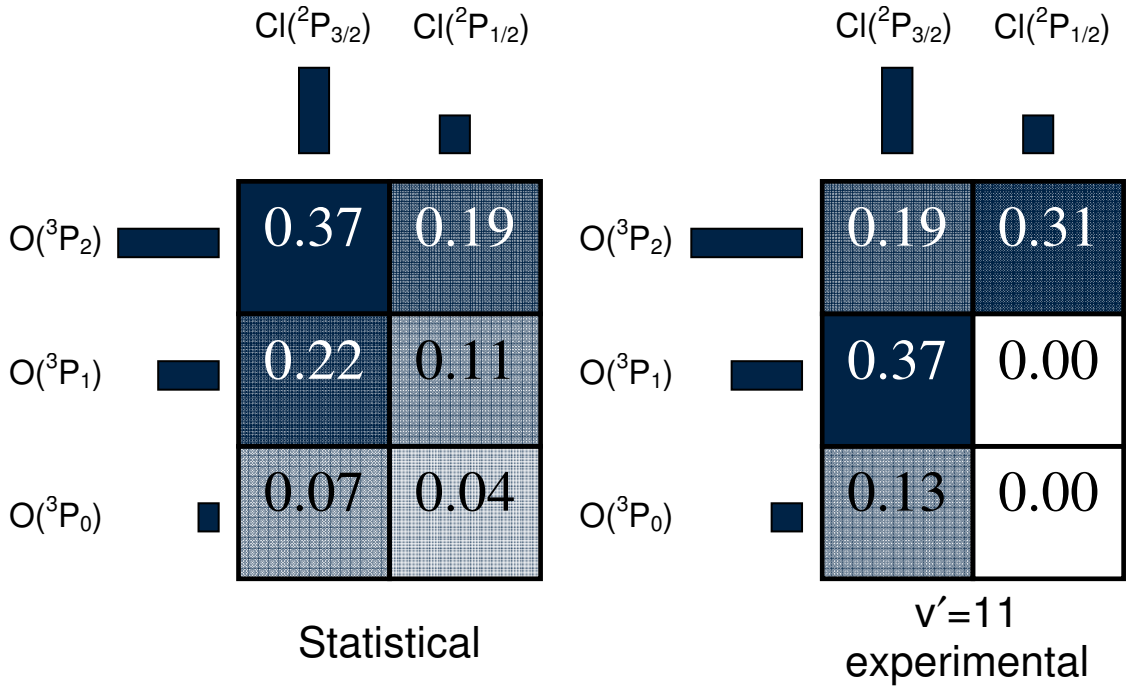

Figure 27: Illustration of the statistical and experimental correlated branching ratios of the predissociation of the v'=11 band of ClO.

Such measurements reflect not only the coupling of the $A\ ^2\Pi_{3/2}$ state to dissociative states in the Franck-Condon region (the crossing region) but also coupling between the dissociative states at longer internuclear separation (the recoupling zone). Initial analysis indicated that the fine-structure branching was more consistent with the diabatic (sudden) than the adiabatic limit using the couplings in the Franck-Condon region derived from the work of Lane *et al.*[124] However, there were significant differences between the diabatic prediction and experiment suggesting errors in the initial coupling and/or dynamical effects in the exit channel. In the present paper we extend the experimental work of Kim *et al.* to lower vibrational levels of the $A\ ^2\Pi_{3/2}$ state (v′=0-5) and expand the analysis of Lane *et al*. to include additional predissociative states. In addition, a comparison between the diabatic limit and the results of coupled channel calculations provide insight into the role of exit channel coupling in the dissociation.

B. Experimental Details

The velocity-map ion-imaging apparatus employed in the present experiments has been described in Chapter II. The photolysis beam (285-310 nm) was generated by the PDL laser system with output frequency doubling by a Spectra Physics WEX-1. The oxygen atoms [$O(^3P_{2,1,0})$] were state-selectively probed using 2+1 REMPI transitions near 226 nm[133] using the frequency doubled output of the LAS laser system. The molecular beam of ClO was formed by the method outlined in Section H of Chapter II.

C. Results and Discussion

Experimental Measurements

Figure 28 shows typical $O(^3P_{0,1,2})$ ion images (left) and reconstructions (right) arising from ClO photodissociation at 299.50 nm corresponding to the bandhead region of the v′ = 4 level of the $A\ ^2\Pi_{3/2}$ state. As previously noted, it is possible to resolve the contributions from $Cl(^2P_{3/1})$ and $Cl(^2P_{1/2})$ formed in coincidence with each probed oxygen fine-structure state. The two rings evident in the $O(^3P_2)$ image correspond to the formation of coincident $Cl(^2P_{3/2})$ and $Cl(^2P_{1/2})$ fragments. The single ring observed in the $O(^3P_1)$ and $O(^3P_0)$ images indicate that these states are only formed in coincidence with $Cl(^2P_{3/2})$. Figure 29 shows velocity distributions that correspond to the images shown in Figure 28. Forward convolution fitting (solid line) of the speed distributions permits an accurate measurement of the $Cl(^2P_{3/2})$/ $Cl(^2P_{1/2})$ branching ratio for each $O(^3P_J)$ fragment. These ratios are highly reproducible, with an estimated error of less than 3%. Once the $Cl(^2P_{3/2})$/ $Cl(^2P_{1/2})$ branching ratio has been determined for each oxygen fine-structure state the correlated fine-structure branching ratios for each vibrational level probed are obtained by including the weighting of each oxygen state based on the integrated 2+1 REMPI signals.[134] Figure 30 shows Doppler profiles of the 2 + 1 REMPI signals and their fits. Integral values shown in Figure 30 provide the $O(^3P_J)$ weighting for the v'= 4 transition. Combining the $Cl(^2P_{3/2})$/ $Cl(^2P_{1/2})$ branching ratio determined from Figure 4.4 with the $O(^3P_2)$/ $O(^3P_1)$/ $O(^3P_0)$ branching ratios from the 2 + 1 REMPI data make

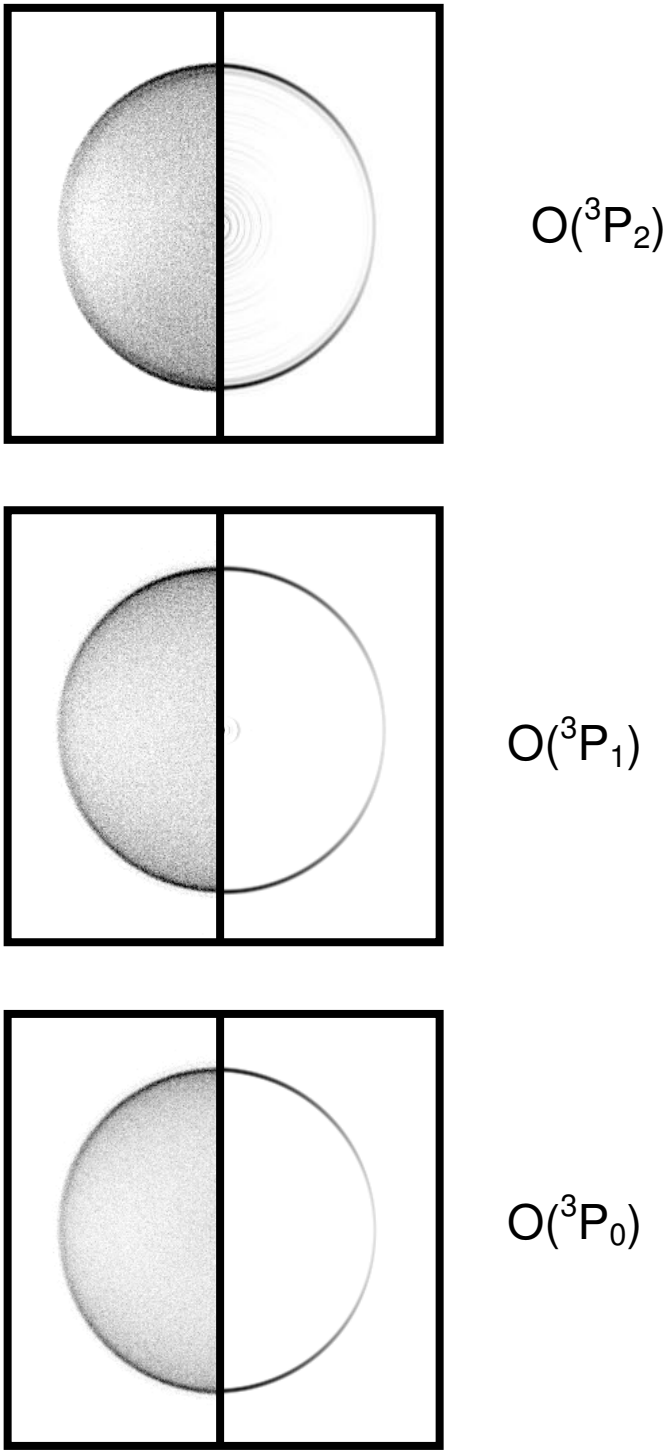

Figure 28: Raw $O(^3P_J)$ images (left panels) and reconstructed images (right panels) arising from ClO photodissociation at 299.50 nm.

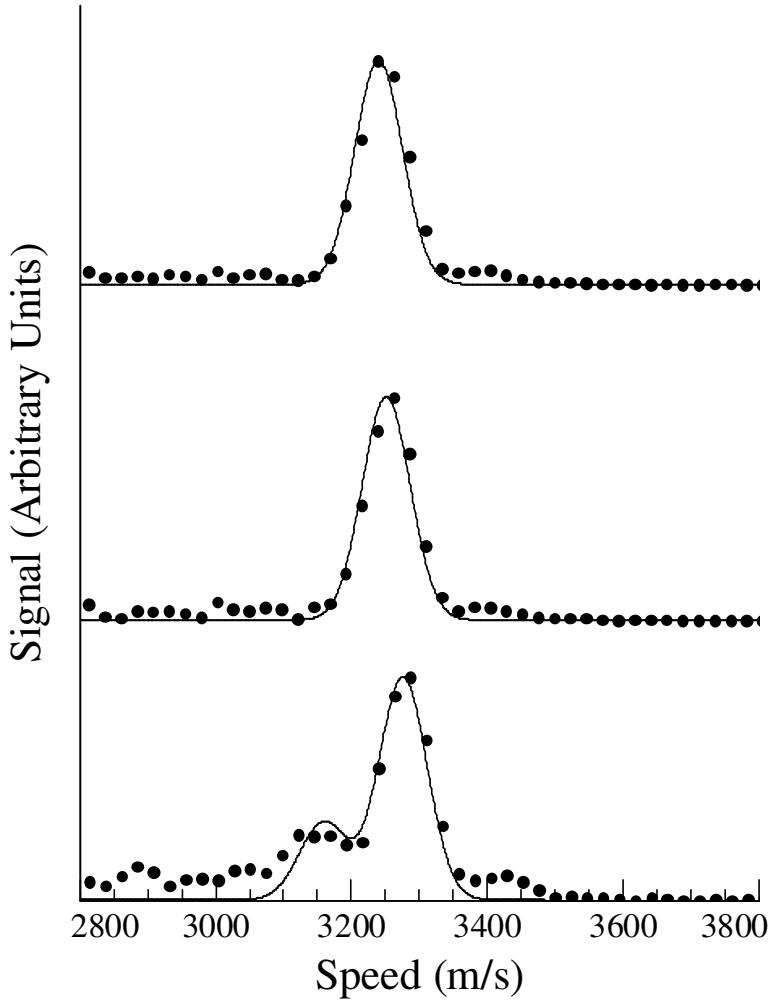

Figure 29: Speed distributions arising from the $O(^3P_J)$ images shown in Figure 28 from the photodissociation of ClO at 299.5 nm. The traces show data as symbols (●) overlaid with a forward convolution fit (solid line). Ratios of the peak areas ($Cl(^2P_{1/2})$ /$Cl(^2P_{1/2})$) are shown in the upper right corner of each panel.

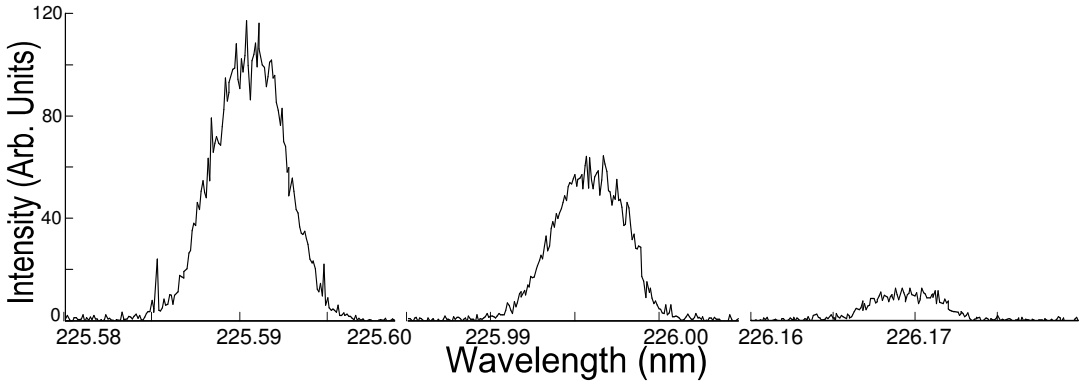

Figure 30: 2 + 1 REMPI signals for the O(^3P_J) states taken while the probe laser is scanned across the transition during the dissociation of ClO using 299.5 nm light. The traces show the data as a solid black line, and a forward convolution fit of the data as a solid red line. Integral values of the 2 + 1 REMPI signals are shown beside the traces.

possible the calculation of full state-dependent correlated branching ratios for the predissociation of each vibrational band studied. For example, the data shown in Figures 28 and 29 provide the correlated branching ratios for the v'=4 band shown as "Experimental" in Table 4.

Table 4 shows the experimental correlated branching ratios measured in this study for v′=0-5 and includes previous data from ref. 132 (bold). Uncertainty in the experimental branching ratios is dominated by determination of the oxygen fine-structure ratio. We observe that the O($^3P_2$) signal is affected by a small amount of probe laser background which was minimized by employing low probe laser power. Based on multiple measurements, we find that the O($^3P_2$)/ O($^3P_1$)/ O($^3P_0$) ratio for a given v′ state is very reproducible and we estimate that the uncertainty for this ratio is approximately 10%. In contrast, the Cl($^2P_{3/2}$)/Cl($^2P_{1/2}$) branching derived from a single oxygen state are very robust with errors of less than 3%. It should be noted that we assume that experimental branching ratios for each vibrational state are independent of J'. Howie *et al*. observed no evidence of J'-dependent predissociation indicating that the primary

interaction of the dissociative states with the A $^2\Pi_{3/2}$ state is *via* spin-orbit coupling.[123] In addition, the *J′*-dependence of the correlated state branching ratios was explicitly examined by Kim *et al.* for the v′=6 and v′=10 bands. No change in correlated state branching ratios was observed as the photolysis laser was tuned from the bandhead to higher *J′*-states.[132] There are several immediate conclusions that can be reached from even a cursory analysis of the experimental branching data. First, by inspection the results are inconsistent with a statistical (strong coupling) limit and exhibit a clear v′-dependence. Second, the results are inconsistent with adiabatic dynamics which does not predict the number of asymptotic channels that are observed in the experiment. This is in agreement with previous photodissociation experiments above the O(^{1}D) threshold. In these experiments dissociation originating from excitation to the continuum of the *A* $^2\Pi$ state, based on observed parallel anisotropy, resulted in only a minor yield of O(^3P_J) fragments suggesting little curve crossing. Finally, the Cl($^2P_{1/2}$) + O($^3P_0$) channel, despite being energetically accessible, is not observed at any wavelength.

Table 4: Correlated fine-structure branching ratios from ClO photodissociation. The bold values are from experiment and underlined values exceed the limits of the diabatic model.

Atomic States	v' = 0	v' = 1	v' = 2	v' = 3	v' = 4	v' = 5	v' = 6	v' = 7	v' = 8	v' = 9	v' = 10	v' = 11
Cl($^2P_{3/2}$) + O($^3P_2$)	**0.10**	**0.07**	**0.24**	**0.21**	**0.28**	**0.17**	**0.19**	**0.22**	**0.09**	**0.29**	**0.24**	**0.19**
Coupled channel:	0.23	0.24	0.25	0.26	0.23	0.21	0.22	0.23	0.23	0.22	0.23	0.25
Diabatic:	0.17	0.18	0.22	0.23	0.22	0.26	0.27	0.22	0.24	0.22	0.25	0.17
Cl($^2P_{1/2}$) + O($^3P_2$)	**0.37**	**0.31**	**0.37**	**0.12**	**0.08**	**0.19**	**0.18**	**0.02**	**0.10**	**0.18**	**0.26**	**0.31**
Coupled channel:	0.21	0.23	0.29	0.23	0.31	0.23	0.19	0.29	0.29	0.32	0.24	0.39
Diabatic:	0.21	0.20	0.19	0.22	0.20	0.25	0.28	0.20	0.22	0.19	0.23	0.13
Cl($^2P_{3/2}$) + O($^3P_1$)	**0.37**	**0.56**	**0.29**	**0.35**	**0.22**	**0.13**	**0.15**	**0.19**	**0.24**	**0.17**	**0.21**	**0.37**
Coupled channel:	0.41	0.38	0.22	0.28	0.20	0.21	0.23	0.16	0.15	0.16	0.21	0.12
Diabatic:	0.29	0.30	0.34	0.31	0.33	0.29	0.28	0.33	0.31	0.33	0.31	0.37
Cl($^2P_{1/2}$) + O($^3P_1$)	**0.10**	**0.00**	**0.07**	**0.00**	**0.16**	**0.23**	**0.22**	**0.34**	**0.21**	**0.30**	**0.16**	**0.00**
Coupled channel:	0.03	0.02	0.02	0.01	0.03	0.08	0.09	0.13	0.07	0.10	0.06	0.03
Diabatic:	0.21	0.19	0.09	0.10	0.09	0.07	0.07	0.10	0.08	0.09	0.08	0.12
Cl($^2P_{3/2}$) + O($^3P_0$)	**0.06**	**0.06**	**0.04**	**0.33**	**0.26**	**0.27**	**0.26**	**0.22**	**0.32**	**0.06**	**0.13**	**0.13**
Coupled channel:	0.12	0.12	0.23	0.22	0.22	0.26	0.27	0.19	0.25	0.20	0.25	0.21
Diabatic:	0.12	0.13	0.17	0.14	0.16	0.13	0.11	0.16	0.15	0.17	0.14	0.20
Cl($^2P_{1/2}$) + O($^3P_0$)	**0.00**	**0.00**	**0.00**	**0.00**	**0.00**	**0.00**	**0.00**	**0.02**	**0.03**	**0.00**	**0.00**	**0.00**
Coupled channel:	0.00	0.00	0.00	0.00	0.00	0.00	0.00	0.00	0.00	0.00	0.00	0.00
Diabatic:	0.00	0.00	0.00	0.00	0.00	0.00	0.00	0.00	0.00	0.00	0.00	0.00

The present experiments involve the $X\ ^2\Pi_{3/2}$ - $A\ ^2\Pi_{3/2}$ parallel transition ($\Delta\Omega = 0$) corresponding to an intrinsic anisotropy parameter of $\beta = 2$. We observe no differences, *i.e.* with the mutual error bounds, between the spatial anisotropies of individual $O(^3P_J)$ images at a given photolysis wavelength. This is consistent with a common origin for the products and suggests that fragment orbital alignment is not influencing the measured signals. However, we observe anisotropy parameters less than the limiting value for all ClO data collected. Since the $O(^3P_0)$ fragment has no angular momentum the measured ion images reflect only the spatial anisotropy. For the v´ = 4 image shown in Figure 28, the $O(^3P_0)$ is best fit by an anisotropy parameter of 0.65±0.10. A recent study provides a method to evaluate photofragment spatial anisotropy as a function of excitation frequency, dissociative state lifetime, and the rotational structure. [135,136] We find that the measured anisotropy parameters are well reproduced using the reported spectroscopic information.

Modeling of the Correlated Fine-Structure Distributions

In our initial study on ClO predissociation[132] we employed the 3-state model of Lane *et al*. to calculate the fine-structure branching ratios in the adiabatic and diabatic limits. The significant differences between the experiment and the diabatic limit treatment at the correlated level were attributed to two factors; 1) incorrect coupling of the dissociative potentials to the $A\ ^2\Pi_{3/2}$ state which provides initial weightings of the dissociative potentials for the diabatic analysis 2) the neglect of exit channel couplings which can alter the distribution established in the crossing region. Although both of these factors ultimately influence the fine-structure branching ratios, only errors in the coupling in the Franck-Condon region will affect the predissociation rates. Therefore, as

a first step in modeling the experimental branching ratios we have re-optimized the dissociative potentials of Lane *et al*., altering both the locations of the crossings with the $A\ ^2\Pi_{3/2}$ state and the coupling constants, using the experimental predissociation rates as the constraint.[121,123] The BCONT program[137,138] was used to calculate predissociation rates and an optimization code, based on an amoeba algorithm, iteratively adjusted coupling constants between each dissociative state and the A $^2\Pi_{3/2}$ state and floated the crossing point for each dissociative state until the best fit to the experimental rates was obtained. We have used *R*-independent coupling constants for potentials in BCONT, including the 3 $^2\Pi$ state despite the strong electrostatic coupling with the $A\ ^2\Pi_{3/2}$ state which should be *R*-dependent as noted previously.[124]

We find that only four dissociative potentials are required to obtain an acceptable fit to the experimental rates: the $2^4\Sigma^-$, $1^2\Delta$, $1^4\Delta$, and $3^2\Pi$. It should be noted that the $1^4\Delta$ and the $1^4\Sigma^+$ states both cross the $A\ ^2\Pi_{3/2}$ state near R=1.95 Å and thus the relative importance of each state is difficult to assess. We chose to fit only the $1^4\Delta$ state based on the relative $1^4\Delta$ and the $1^4\Sigma^+$ coupling constants reported by Toniolo *et al*. Our derived coupling constant for the $1\ ^4\Delta$ should, therefore, be considered as a sum of the coupling constants for both the $1^4\Delta$ and $1^4\Sigma^+$ states. The inclusion of additional dissociative states beyond the four states employed did not provide significant improvement of the fit. The results of the optimization are shown in Figures 30 and 31.

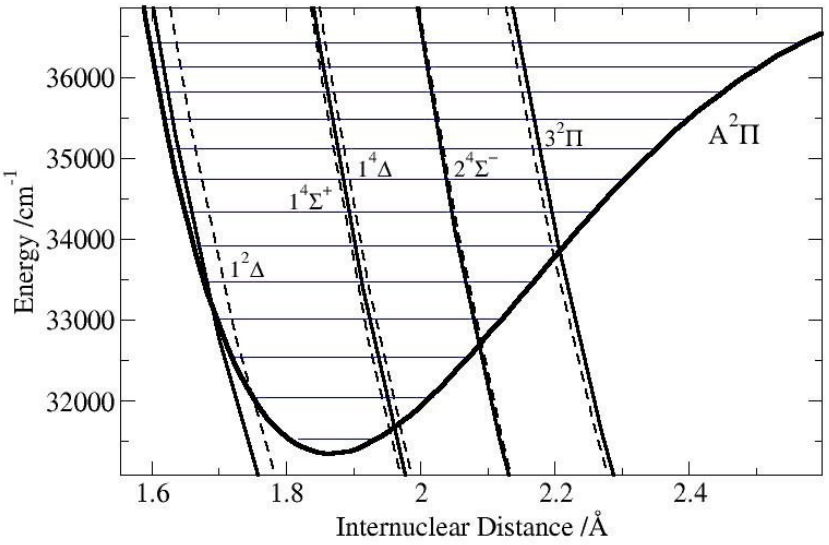

Figure 31: The A $^2\Pi_{3/2}$ excited state potentials for ClO from reference 123 and the A $^2\Pi_{3//2}$ vibrational states are indicated by the solid lines and the dashed lines represent the results of the optimization described in the text. RKR curve calculated in reference 122.

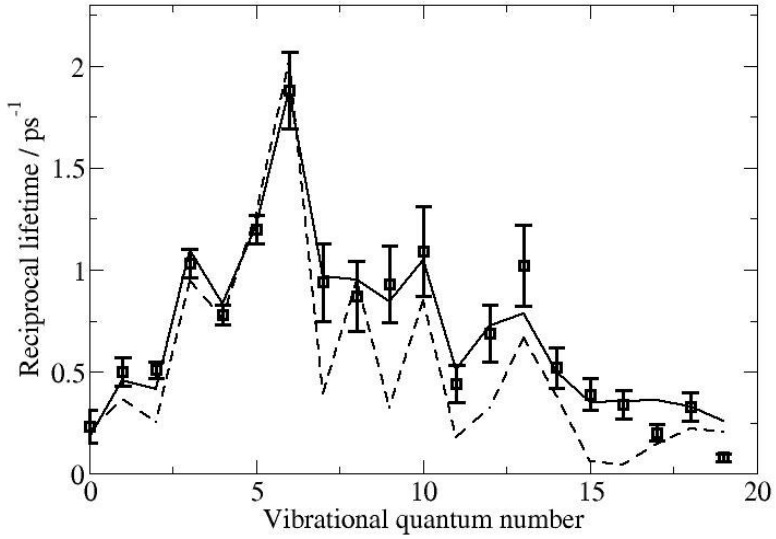

Figure 32: V'-dependent predissociation rates for ClO. Experimentally determined v'-dependent predissociation rates of the A $^2\Pi_{3/2}$ state (Reference 123). The dashed line is the model from Reference 124 and the solid line is the result of the optimization described in the text.

Figure 31 illustrates that the final potentials are very close to the initial potentials of Lane *et al*. The largest shift is found for the 1 $^2\Delta$ state which crosses the A $^2\Pi_{3/2}$ state near the inner wall. The predissociation rates predicted for this potential results in a broad, non-oscillatory, v′-dependence as discussed by Lane *et al*. We find a significant improvement to the fit of the experimental predissociation rate data (Figure 32) compared to the model of Lane *et al*. which included only the 3 $^2\Pi$, 1 $^4\Sigma^+$, and the 2 $^4\Sigma^-$ dissociative states. The local maximum in the v′-dependent rates coincides with the crossing of 3 $^2\Pi$ state.[124] The coupling constants between the dissociative states and the *A* $^2\Pi_{3/2}$ state derived from the optimization are given in Table 5. The *ab initio* coupling constants calculated by Toniolo *et al*. and the derived coupling constants of Lane *et al*. are provided in Table 5 for comparison. Overall there is excellent agreement with the optimized results of Lane *et al*. and purely *ab initio* results of Toniolo *et al*. considering the combined treatment of the $1^4\Delta$ and $1^4\Sigma^+$ states. We do find, however, a lower coupling constant for the 3 $^2\Pi$ state of approximately 20%. The lower derived coupling constant for this state, whose interaction with the *A* $^2\Pi_{3/2}$ state is dominated by electrostatic coupling, is consistent with the lack of observed perturbation in the vibronic spectrum. The decrease in the 3 $^2\Pi$ coupling is a consequence of including the broad v′-dependence contribution of the 1 $^2\Delta$ state and the constraint of matching the predissociation rate maximum at v′=6.

Table 5: Coupling constants between the A $^2\Pi_{3/2}$ state and dissociative electronic states.

	ref 40	ref 39	this work
$1^4\Sigma$+	49.7 cm^{-1}	13 cm^{-1}	N/A
$2^4\Sigma$-	82 cm^{-1}	69 cm^{-1}	71.6 cm^{-1}
$3^2\Pi$	125.4 cm^{-1}	124 cm^{-1}	99.2 cm^{-1}
$1^4\Delta$	N/A	28 cm^{-1}	46.5 cm^{-1}
$1^2\Delta$	N/A	57 cm^{-1}	59.9 cm^{-1}

The fine-structure branching ratio for each vibrational state is obtained by multiplying the normalized weighting of each dissociative state, based on the BCONT predissociation rates for each state, by the diabatic matrix (Table 6) which reflects the partial contribution of atomic states to each molecular state.[132,139,140] The adiabatic correlation diagram is shown in Figure 33. The fine-structure branching ratios calculated using this procedure are provided in Table 3. We find that the branching calculated from the optimized potentials provide an overall better fit to the experimental data than the original 3-potential model of Lane *et al*. Given the complex nature of the observables it is often more instructive to examine alternative representations, in this case summed over coincident fragment populations. The diabatic prediction of the overall v′-dependent $Cl(^2P_{1/2})$:$Cl(^2P_{3/2})$ distributions shown in the bottom panel of Figure 34 is in reasonable agreement with experiment. By comparison, the adiabatic limit

Table 6: Partial contributions of atomic fine-structure states to ClO molecular states as calculated in reference 18.

	ClO Molecular States				
Atomic States	$1\ ^4\Sigma^+$	$2\ ^4\Sigma^-$	$3\ ^2\Pi$	$1\ ^2\Delta$	$1\ ^4\Delta$
$Cl(^2P_{3/2}) + O(^3P_2)$	0.2500	0.2778	0.3333	0.1667	0.1667
$Cl(^2P_{1/2}) + O(^3P_2)$	0.3333	0.2778	0.3611	0.1111	0.2222
$Cl(^2P_{3/2}) + O(^3P_1)$	0.2500	0.2778	0.2222	0.3889	0.2778
$Cl(^2P_{1/2}) + O(^3P_1)$	0.0000	0.0556	0.0278	0.1111	0.2222
$Cl(^2P_{3/2}) + O(^3P_0)$	0.1667	0.1111	0.0556	0.2222	0.1111
$Cl(^2P_{1/2}) + O(^3P_0)$	0.0000	0.0000	0.0000	0.0000	0.0000

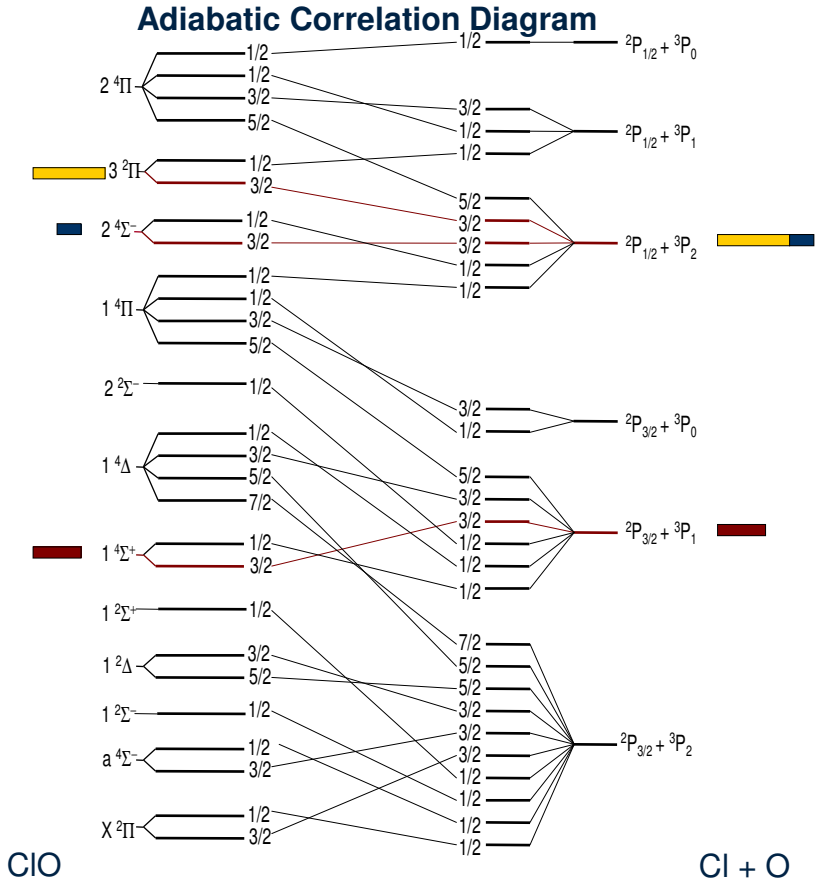

Figure 33: The adiabatic correlation diagram for the ClO A($^2\Pi_{3/2}$) predissociation. This diagram shows the asymptotic limit of each dissociative state. Color bars (left) represent the fraction of predissociation due to the repulsive state, and branching ratio (right).

predicts primarily Cl($^2P_{1/2}$) in contrast to observation. The overall Cl($^2P_{1/2}$):Cl($^2P_{3/2}$) branching is consistent with the statistical prediction despite clear evidence at the correlated level for non-statistical behavior and demonstrating the advantage of correlated measurements. Both exhibit fluctuations around a similar average value although the variation in the experimental data is considerably larger. Since the individual atomic contributions to each molecular state (Table 5) do not show significant variability, the diabatic prediction, which represents a linear combination of these

values, is not expected to exhibit large fluctuations in the product branching ratios. The v′-dependent $O(^3P_J)$ distributions are shown in Figure 35. The experimental values (top panel) again exhibit greater fluctuations than the diabatic model. Interestingly both experiment and the diabatic model on average show significantly higher yields for the $O(^3P_1)$ and $O(^3P_0)$ products than predicted by the statistical (strong coupling) limit. However, the increased yield of $O(^3P_0)$ from v′=3 to v′=8, due to an increase in the $Cl(^2P_{1/2})$ + $O(^3P_0)$ channel over this range of v′, is not well reproduced.

A better comparison between experiment and theory, both from the standpoint of experimental confidence in the values and an increased level of detail, involves the $Cl(^2P_{1/2})$:$Cl(^2P_{3/2})$ branching fractions for each $O(^3P_J)$ state and is shown in Figure 36. The absence of the $Cl(^2P_{1/2})$ formed in coincidence with $O(^3P_0)$ is consistent with the diabatic prediction. This is not surprising given the lack of contribution from this atomic channel to any of the dissociative considered in the model. The experimental data exhibit clear trends in the $Cl(^2P_{1/2})$:$Cl(^2P_{3/2})$ branching, however, which are not reproduced by the model. As discussed previously these values are derived from the relative intensities of features associated with the formation of $Cl(^2P_{1/2})$ and $Cl(^2P_{3/2})$ in a single image and are therefore relatively insensitive systematic errors. These differences, specifically the increase in the $Cl(^2P_{1/2})$ between v′=4 and v′=10 in coincidence with $O(^3P_1)$, is inconsistent with the diabatic model. We also note that several fine-structure states are observed with populations that exceed their partial contributions to any dissociative states. These values are underlined in Table 4. The fact that these observations cannot

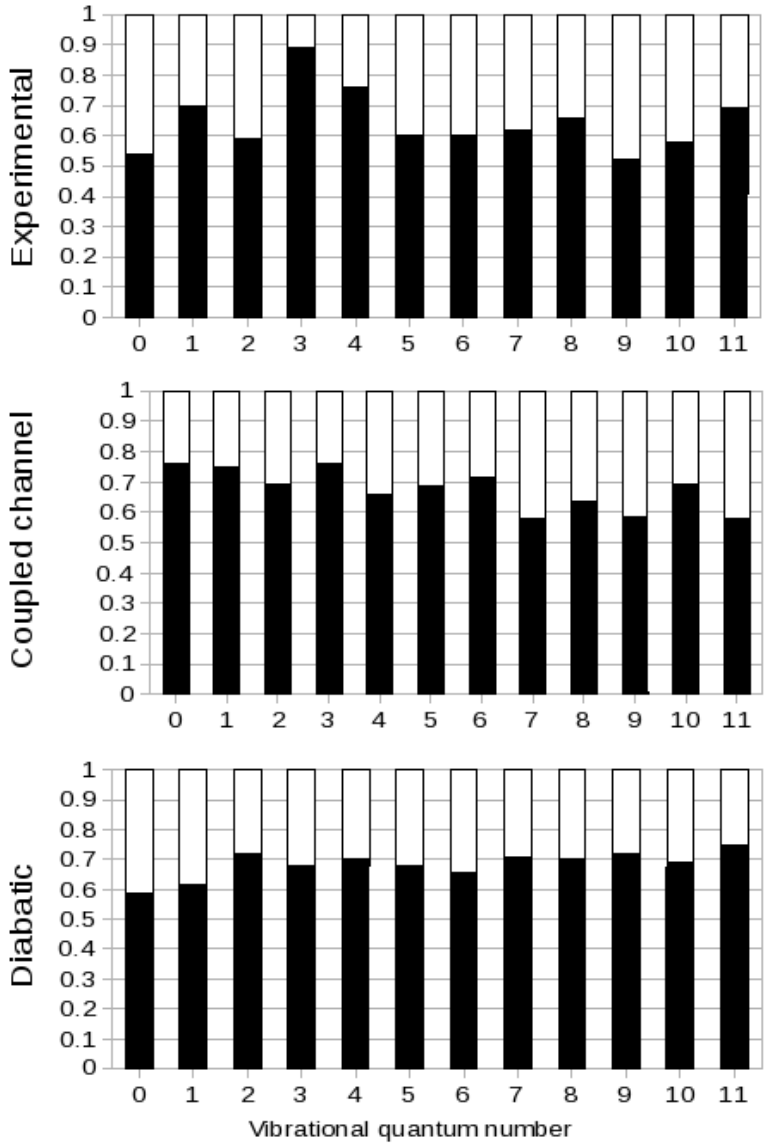

Figure 34: Overall Cl($^2P_{3/2}$) (black) and Cl($^2P_{1/2}$) (white) branching ratios as a function of A $^2\Pi_{3/2}$ vibrational level. The results from experiment, closed channel calculations, and the diabatic limit model, are shown in the top, middle and bottom panels respectively.

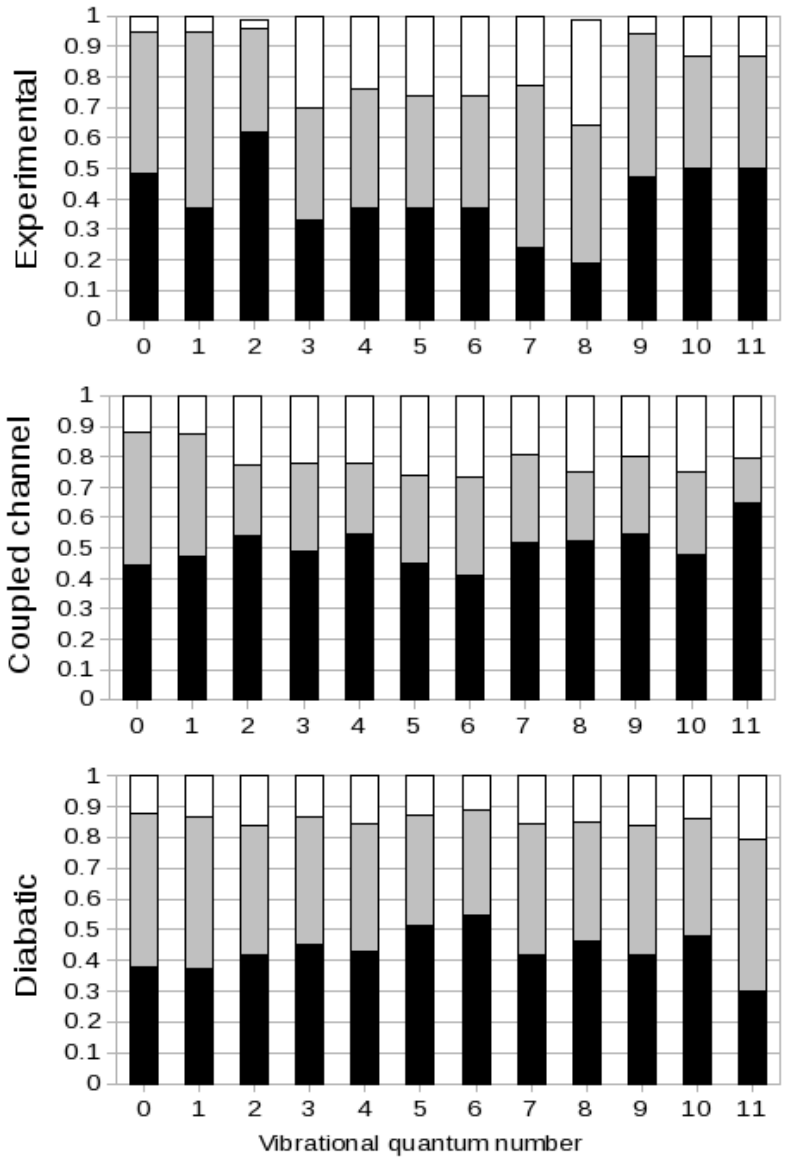

Figure 35: Overall O($^3P_2$) (black), O($^3P_1$) (grey), and O($^3P_0$) (white) populations for each as a function of A $^2\Pi_{3/2}$ vibrational level. The results from experiment, closed channel calculations, and the diabatic limit model, are shown in the top, middle and bottom panels respectively

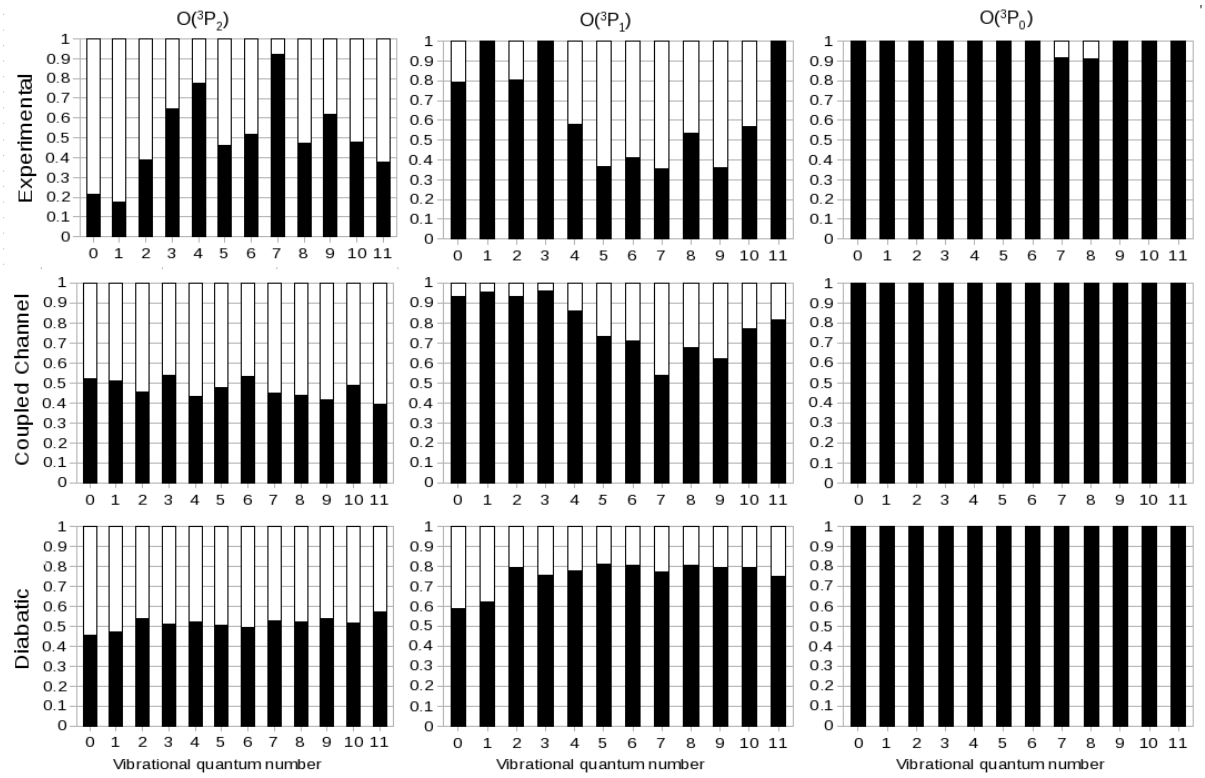

Figure 36: Cl($^2P_{3/2}$) and Cl($^2P_{1/2}$) branching ratios for each oxygen fine structure state as a function of A $^2\Pi_{3/2}$ vibrational level. The results from experiment, closed channel calculations, and the diabatic limit model, are shown in the top, middle and bottom panels respectively.

be achieved by any set of the potentials considered in the model, including the 1 $^4\Sigma^+$ state, is clear evidence that exit channel coupling must play a role.

D. Summary

In an effort to assess the role of exit channel coupling we have performed closed channel calculations using the optimized potentials. The results of the calculations are given in Table 5 and shown in Figures 32-34. The coupled channel calculations are generally in better agreement with experiment than the diabatic model predictions. In most cases where the measured branching ratio for a specific final state exceeded the diabatic prediction the closed channel calculation approaches the experimental value. In

particular, the $Cl(^2P_{1/2})$:$Cl(^2P_{3/2})$ branching for the $O(^3P_1)$ from the closed channel calculation captures the distinctive trend observed in the experiment (Figure 34). In summary, progress towards a detailed understanding the dissociative dynamics of ClO is encouraging but differences between experiment and theory, outside the estimated experimental error bounds, remain. Further work to resolve these outstanding issues is warranted.

CHAPTER V

PHOTODISSOCIATION DYNAMICS OF BrO

A. Introduction

The absorption spectroscopy of BrO has been well studied.[141, 142, 143, 144, 145, 146, 147, 148, 149] The spectrum consists of a vibrational progression from 380 nm to 285 nm, near the A $^2\Pi_{3/2}$ dissociation limit. Figure 37 shows the absorption spectrum of BrO as recorded by Wilmouth *et al.*[149] Most of the states are broadened due to the speed of the predissociation, although some bands (v'= 4, 7, and 12) are somewhat rotationally resolved. Recent studies by Wilmouth *et al.* and Orr-Ewing and coworkers have characterized the predissociation lifetimes of the v'= 7, and 12 vibrational bands by fitting the rotational structure of the band.[148,149]

The results are somewhat contradictory as Orr-Ewing and coworkers found the lifetime across the band to be a constant value while Wilmouth *et al.* found that the

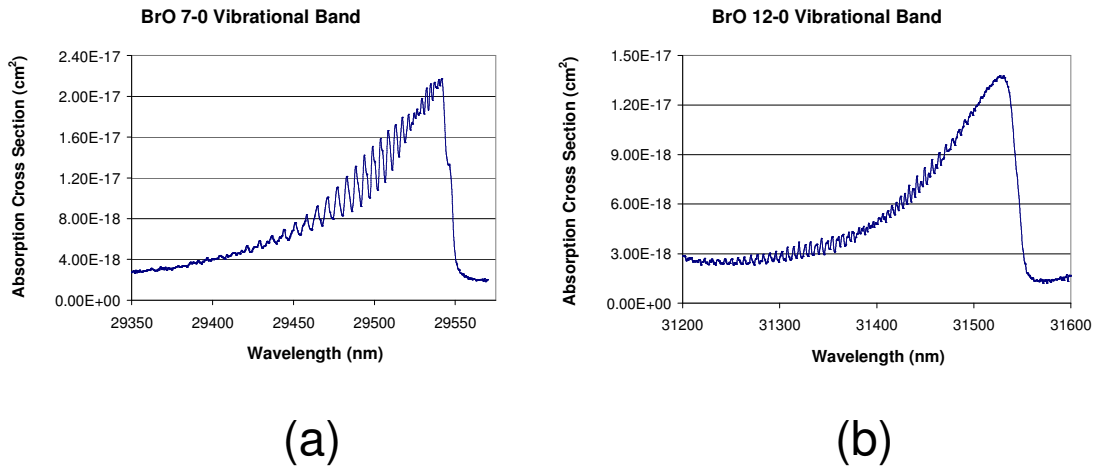

Figure 37: Absorption spectra of the 7-0 (a) and 12-0 (b) vibrational bands measured and modeled by Reference 149.

lifetime varied across the bands. Orr-Ewing and coworkers employed cavity ring-down spectroscopy to study the rotationally resolved 7-0 and 12-0 transitions and determined predissociation lifetimes for these transitions of 1.7±0.2 ps for the 7-0 band and 1.3±0.2 ps for the 12-0 band based on the spectral linewidths.[148] In contrast, Wilmouth *et al.* observed J'-dependent linewidths for the 7-0 and 12-0 bands indicating predissociation induced by molecular rotation as well as spin-orbit coupling, in contrast to the case for ClO.[149]

The BrO radical has been studied through ab initio studies as well, although the difficulty of this system due to the large spin orbit coupling of bromine has caused this task to be attempted in only a few studies.[150, 151, 152] The optimized geometry of the BrO radical and cation was determined through high level ab initio calculations by Francisco *et al.*[150] In this study, they also determined the adiabatic electron affinity and ionization potentials of BrO. In a subsequent study, Li *et al.* used high level calculations to investigate the unbound states that predissociate the A $^2\Pi_{3/2}$ state of BrO as well as the vertical excitation energies for the excited states of BrO.[151] K. Peterson has recently done extensive ab initio work on the BrO system, providing electronic energy potentials including the ground (X $^2\Pi_{3/2}$) and excited ($A^2\Pi_{3/2}$) bound states, as well as numerous unbound excited states. He also determined coupling constants for the predissociation of the $A^2\Pi_{3/2}$ state by the calculated unbound states.[152] We are extremely grateful to him for sharing his unpublished work with us, as it is an important foundation for the work shown here. The potentials look very similar to the ones shown in Figure 26.

Similar to the case of IO, accurate thermodynamic measurements of BrO are important to the atmospheric modeling community as there are reactions that depend strongly on the accuracy of these constants. A fundamental physical constant of much importance is the bond dissociation energy of BrO. Nevertheless, in the past, studies that determine this value rely on spectroscopic measurements to determine the bond dissociation energy of the molecule based on the positions of the vibrational band origins. These methods require some estimation from the use of a graphical

extrapolation method such as that of Birge-Sponer or Berstein-Leroy extrapolation. Unfortunately, the intensities of the absorption of the low vibrational levels is very low in the case of BrO as can be seen in Figure 37 causing large errors in the derived bond dissociation energy from the extrapolation methods. Recently, Wilmouth et al. determined the bond dissociation energy of BrO using a graphical Birge-Sponer method resulting in a value of 55.2±0.4 kcal/mol.[149] In a time of flight mass spectrometry (TOFMS) study, Zou *et al.* estimated the BrO bond dissociation energy to be 55.8±1.0 kcal/mol based on the derived speed distribution at 355 nm.[153] We recently measured the bond dissociation energy of BrO using the velocity map ion imaging technique that has been shown recently to provide accurate direct measurement of bond dissociation energies of diatomic molecules.[154, 155, 156] In this investigation, measurements of low velocity photofragments resulting from photodissociation just above the O $^1D_2$ threshold provide an accurate and direct determination of the A $^2\Pi_{3/2}$ state dissociation threshold of 35418 ± 35 cm^{-1}, leading to a ground state bond energy of D_0^0 (BrO) = 55.9 ± 0.1 kcal/mol.

To date, the photodissociation of BrO has received less attention than the analogous ClO system. To our knowledge, there have been only two experimental studies of BrO photodissociation that has measured the nascent products.[153, 157] Zou et al. studied the photodissociation of BrO in a molecular beam produced by electric discharge through a mixture of Br_2 + O_2 using state-selected time-of-flight mass spectroscopy (TOFMS).[153] In this study, Zou *et al.* measured a relative Br($^2P_{3/2}$)/Br($^2P_{1/2}$) branching ratio of 1.5 in coincidence with O($^3P_2$) at 355 nm. Kim *et al.* presented a more detailed examination of the photodissociation dynamics of BrO at 355 nm and at wavelengths between 278 and 281.5 nm. This study focused on the relative electronic product branching ratio and photofragment angular distributions at 355 nm to address the role of predissociation dynamics. Kim *et al.* also presented an investigation of the Br(^2P_J)+O($^1D_2$) channel just above the O($^1D_2$) dissociation threshold.

Correlated fine structure branching ratios of the predissociation of BrO are measured in the current study. Similar to that of ClO which were presented in Chapter

IV, these measurements facilitate the comparison of experimental measurements to ab initio calculations. The previous study by Kim *et al.* introduced above provides a measurement of the correlated branching ratios for the v'=4 band at 355 nm. The current study measures the branching ratios for predissociation of v'= 18-5. Below v'=4, the absorption coefficient is inadequately low to make further measurements feasible.

The current work also provides another direct measurement of the bond dissociation energy of BrO which complements the determination of Kim *et al.*[157] Although the current measurement has a much larger error associated with the bond dissociation energy, it is in agreement with the measurement of Kim *et al.* We also use the software BCONT to explore the ab initio results of K. Peterson. The potentials and coupling constants calculated in that study are shifted and adjusted to provide insight into the predissociation of the A $^2\Pi_{3/2}$ state of BrO.

B. Experimental Details

The velocity-map ion-imaging apparatus employed in the present experiments has been described in Chapter II. The photolysis beam (285-310 nm) was generated by the PDL laser system with output frequency doubling by a Spectra Physics WEX-1. The oxygen atoms [O($^3P_{2,1,0}$)] were state-selectively probed using 2+1 REMPI transitions near 226 nm[158] using the frequency doubled output of the LAS laser system. The molecular beam of BrO was formed by the method outlined in Section I of Chapter II. Ion optic voltages used for this experiment are 3000 V for the repeller, 2662 V for Lens 1, and 2370 V for Lens 2.

C. Results and Discussion

Experimental Branching Ratio Results

Figure 38 shows typical O($^3P_{0,1,2}$) ion images (left) and pBASEX reconstructions (right) arising from BrO photodissociation at 329.6 nm corresponding to the bandhead region of the v′ = 9 level of the *A* $^2\Pi_{3/2}$ state. The images were reconstructed using the

commercially available software BASEX for speed distributions. Figure 39 shows the velocity distributions derived from the images shown in Figure 38. The velocity distribution data is shown with a forward convolution fit overlay. Similar to the case of ClO explained in Chapter IV, the full state-dependent correlated branching ratios can be determined by weighting the information from the forward convolution fit with the $O(^3P_J)$ state fractions derived from the numerical integration of the intensities 2 + 1 REMPI transitions near 266 nm.[159] For integration purposes, the Doppler profiles of the 2 + 1 REMPI transitions of the $O(^3P_J)$ states are modeled using a forward convolution fit as shown in Figure 40. As can be seen from the top panel in Figure 38, both $Br(^2P_{3/2})$ and $Br(^2P_{1/2})$ are formed in coincidence with $O(^3P_2)$ as is evident from the two rings seen in that panel. The single ring observed in the $O(^3P_1)$ and $O(^3P_0)$ images indicate that these states are only formed in coincidence with $Br(^2P_{3/2})$. These ratios are highly reproducible, with an estimated error of less than 3%. Similar to the ClO branching ratio data given in Chapter IV, the uncertainty in the experimental branching ratios is dominated by determination of the oxygen fine-structure ratio which we estimate to be less than 10%. To ensure that the 2 + 1 REMPI intensity collected for the $O(^3P_2)$/ $O(^3P_1)$/ $O(^3P_0)$ ratios in the measurement are as accurate as possible, we use low probe beam powers to minimize signal intensity from probe laser background. Nevertheless, in a few cases when measuring the low vibrational levels (v' = 5-9), background signal from the probe laser was corrected for as it could not be effectively minimized while retaining reasonable signal to noise of the 2-laser BrO signal. In these cases, 2 + 1 REMPI Doppler profiles were collected while the dissociation laser was blocked to allow for the subtraction of background signal from the intensities of the 2 + 1 REMPI profiles collected while both lasers were on. This is especially useful as the background tends to be larger for the $O(^3P_2)$ fragment than the $O(^3P_1)$ or $O(^3P_0)$ fragments which would skew the branching ratios to favor the $O(^3P_2)$ channels. Final Correlated branching ratios for the v'= 4-18 are given in Table 7.

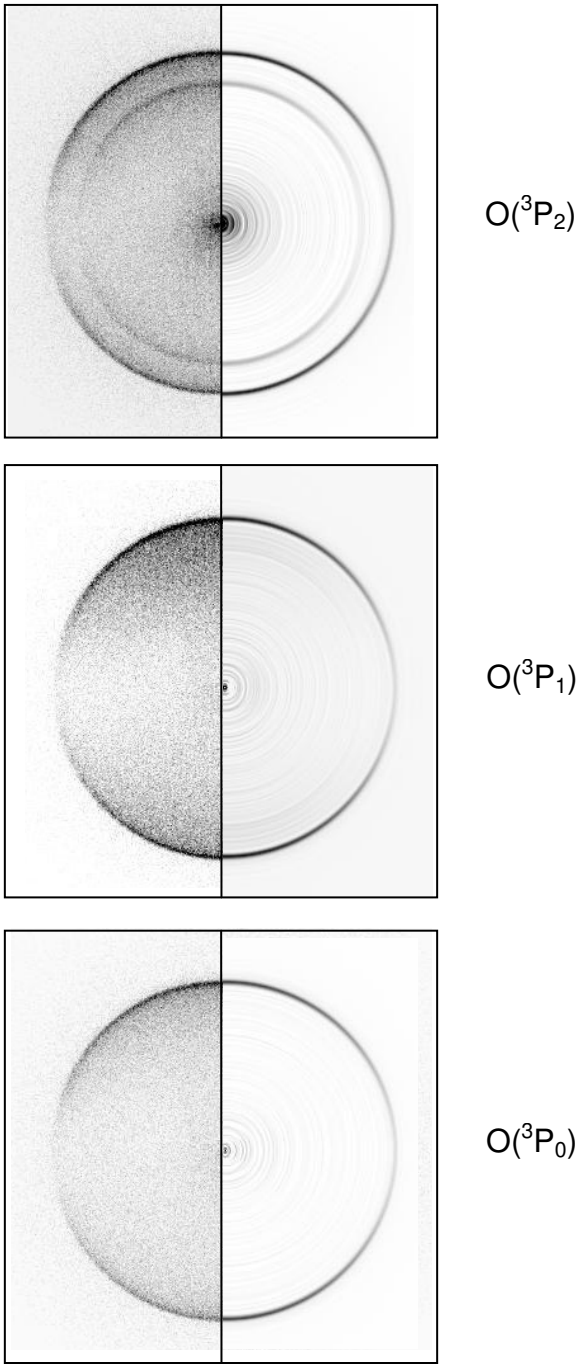

Figure 38: Images of $O(^3P_J)$ fragments from BrO photodissociation at 329.6 nm.

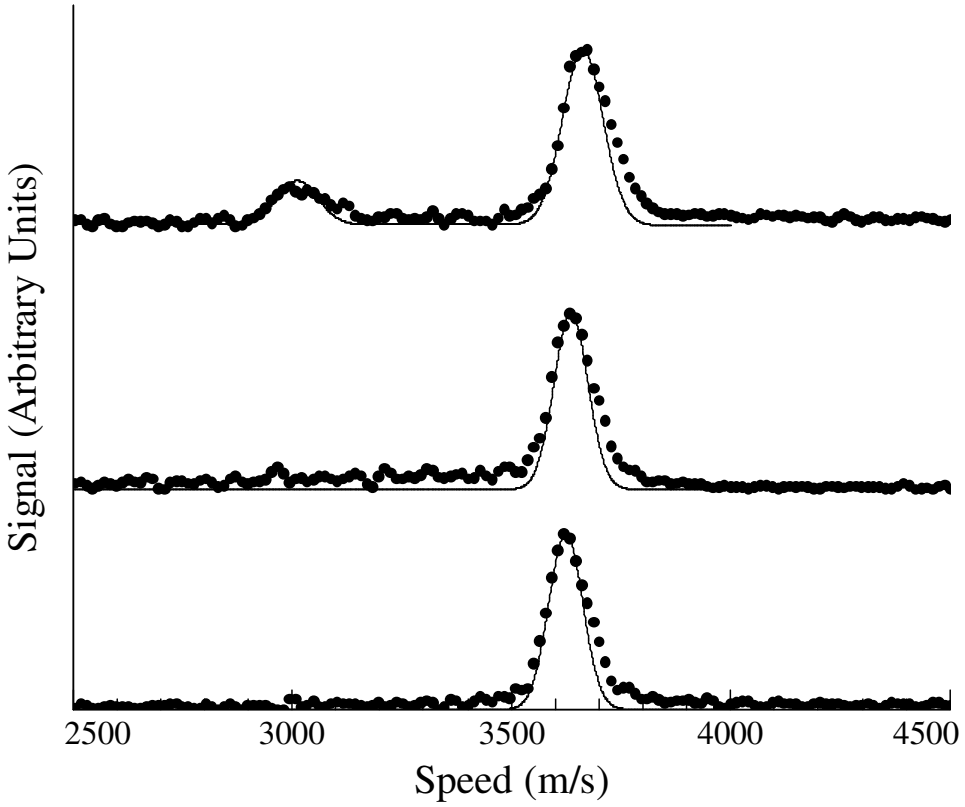

Figure 39: Velocity distributions of the $O(^3P_J)$ fragment images shown in Figure 38 for the v'=9 band.

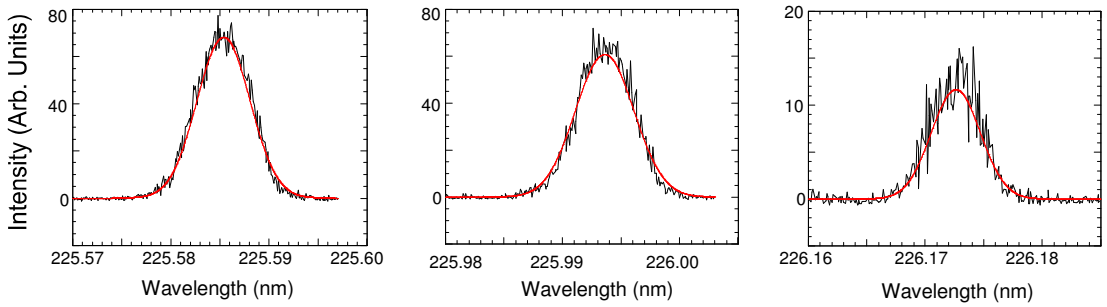

Figure 40: 2+1 REMPI transitions providing the $O(^3P_2)/O(^3P_1)/O(^3P_0)$ branching ratios for the v'=9 band. Data is shown (black) overlaid with a Gaussian fit (red).

Table 7: Experimental correlated final state branching ratios for v'=4-18.

	v' Level														
Asymptotic States	**18**	**17**	**16**	**15**	**14**	**13**	**11**	**12**	**10**	**9**	**8**	**7**	**6**	**5**	**4**
$O(^3P_2) + Cl(^2P_{3/2})$	0.12	0.30	0.49	0.21	0.26	0.23	0.14	0.29	0.27	0.23	0.20	0.35	0.21	0.22	0.38
$O(^3P_2) + Cl(^2P_{1/2})$	0.13	0.10	0.07	0.08	0.20	0.26	0.29	0.27	0.16	0.04	0.37	0.25	0.31	0.09	0.12
$O(^3P_1) + Cl(^2P_{3/2})$	0.50	0.51	0.36	0.55	0.45	0.42	0.24	0.37	0.42	0.55	0.36	0.29	0.45	0.60	0.39
$O(^3P_1) + Cl(^2P_{1/2})$	0.14	0.01	0.00	0.06	0.00	0.05	0.18	0.00	0.06	0.00	0.04	0.04	0.00	0.00	0.00
$O(^3P_0) + Cl(^2P_{3/2})$	0.11	0.08	0.07	0.10	0.09	0.05	0.14	0.07	0.09	0.18	0.03	0.07	0.02	0.09	0.10
$O(^3P_0) + Cl(^2P_{1/2})$	0.00	0.00	0.00	0.00	0.00	0.00	0.00	0.00	0.00	0.00	0.00	0.00	0.00	0.00	0.00

Based on the experimental branching data, there are some conclusions about the dynamics that can be made. First, it is immediately clear that, similar to the ClO system, the branching ratios are non-statistical. It is obvious by inspection that there is a strong v'-dependence in the branching ratios. Also, the $Br(^2P_{1/2}) + O(^3P_0)$ channel is not observed in any of the v'-levels measured although it is energetically accessible. In the ClO case, it was seen through previous photodissociation experiments above the $O(^1D)$ threshold that originated from excitation to the continuum of the $A\ ^2\Pi$ state, resulted in only a minor yield of $O(^3P_J)$ fragments suggesting little curve crossing.[129] The BrO system is assumed to be more adiabatic than the ClO due to the larger spin-orbit coupling and the slower moving fragments resulting from the BrO dissociation. The absence of the $Br(^2P_{1/2}) + O(^3P_1)$ channel until $v' \geq 7$ is a very interesting feature of the data and provides insight into the coupling of the $A(^2\Pi_{3/2})$ to the dissociative $3\ ^2\Pi$ and $2\ ^4\Sigma^-$, the states that correlate to this channel.

Above the v'=6 level, the $Br(^2P_{1/2}) + O(^3P_1)$ channel appears which is a very interesting difference between the ClO and BrO. In the ClO system, $O(^3P_1)$ is formed in coincidence with only the $Cl(^2P_{3/2})$ state, however, in the BrO system, we see $O(^3P_1)$ formed in coincidence with both $Br(^2P_{3/2})$ and $Br(^2P_{1/2})$ at some of the higher vibrational levels. The $O(^3P_1)$ images for the BrO system are shown in Figure 41. As you can see

from the images, the $O(^3P_1) + Br(^2P_{1/2})$ channel (inner ring) is present in some of the images based on the vibrational level being accessed. This oscillation suggests that there is a dissociative state crosses through the $A(^2\Pi_{3/2})$ state that is in a position that makes the wavefunction of the dissociative state add constructively and destructively with the wavefunctions of the different vibrational levels of the bound $A(^2\Pi_{3/2})$, making the predissociation of BrO to $Br(^2P_{1/2}) + O(^3P_1)$ come and go.

In the case of ClO, we assume that the branching ratios for each vibrational state to be independent of J' based on the observations of Howie *et al.* who observed no J' – dependent predissociation which indicated that the interaction of the dissociative states with the A $^2\Pi_{3/2}$ state is *via* spin-orbit coupling.[39] This was further backed up by the measurement of correlated state branching ratios for the v′=6 and v′=10 bands of ClO as the photolysis laser was tuned from the bandhead to higher *J′*-states, which produced no observation of *J′*-dependence in the branching ratio measurements.[132] However, unlike ClO, Wilmouth *et al.* observed a J'-dependence in the lifetime in the measured in the v' = 7 and v' = 12 transitions of BrO.[149] In contrast, the same measurement by Orr-Ewing and coworkers showed no J'-dependence in the measurement of the predissociation lifetime in the measured v' = 7 and v' = 12 transitions of BrO.[148] In our study, we have measured the correlated branching ratio for the v' = 12 level of BrO, and have seen some evidence of J'-dependence in the branching ratios measured along this band. Further measurements are currently being made to fully characterize the branching ratios across this band.

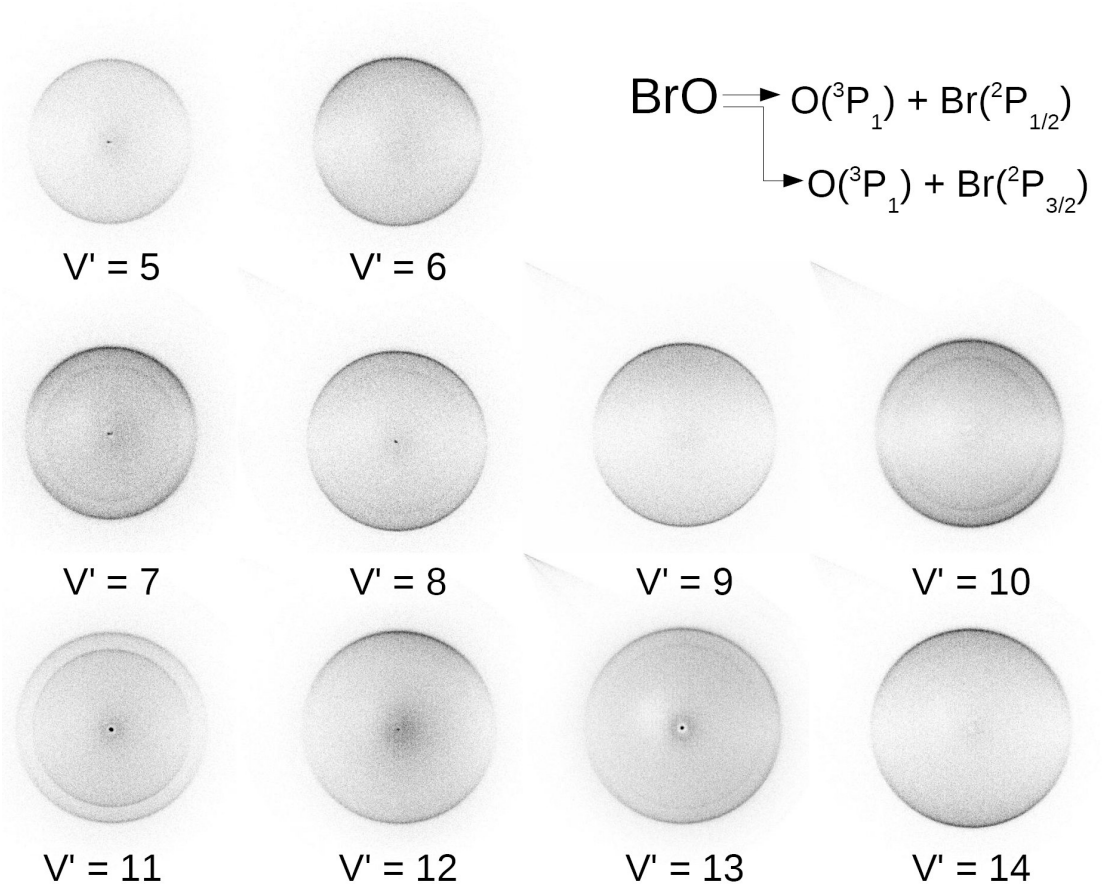

Figure 41: BrO O($^3P_1$) images for the vibrational bands listed below each image.

Bond Dissociation Energy

As was mentioned in the introduction of this chapter, previous measurements of the bond dissociation energy of BrO were obtained through extrapolating spectroscopic measurements of the bound A $^2\Pi \leftarrow$ X $^2\Pi$ transitions resulting in a bond dissociation energy value of 55.3±0.6 kcal/mol.[157] Spectroscopic extrapolation using the linear Birge-Sponer method or the exponential LeRoy-Berstein methods are particularly challenging in the case of BrO where lifetime broadening does not afford rotational resolution of single isotopomers, and rotational resolution is only seen in a few bands. Consequently, previous analysis has relied on the peak position of vibronic bands rather

than accurate band origins. One reason that extrapolating is not a valid method for the determining accurate bond dissociation energy for BrO is that it is well known that some molecules, particularly excited states of diatomic radicals, exhibit positive curvature on a Birge-Sponer plot. A linear Birge-Sponer extrapolation is consistent with a Morse potential function, but this potential provides a poor description near threshold where long range interactions are important. LeRoy and Bernstein have advocated an alternative extrapolation based on the $-1/r^n$ form of the long-range interaction. Wilmouth et al. reported a $D_0^0(BrO)$ value of 55.6 kcal/mol based on such analysis applied to their recent absorption spectrum measured at 10 cm−1 resolution. [149] Our own analysis using the peak positions of the 10 cm−1 spectra of Wilmouth et al. yields values ranging from 55.2 to 56.1 kcal/mol depending on the number of vibrational bands included in the extrapolation.

A more recent extrapolation by Fleischmann et al. based on Fourier transform spectroscopy measurements resulted in a bond dissociation energy value for BrO of 55.4±0.5 kcal/mol although this value reflects a compromise between Birge-Sponer and LeRoy-Bernstein derived values.[160] The results of their LeRoy-Berstein analysis on band origins was 55.8 kcal/mol, much closer to the value directly measured by Kim *et al*. of 55.9 ± 0.1 kcal/mol using velocity map ion imaging.

In the study by Kim *et al.*, Br($^2P_{3/2}$) fragments were imaged from the dissociation of BrO at wavelengths just above the O(^1D) threshold. These images were treated using two complementary methods. The first approach relied on extracting the total fragment translational energy at each wavelength independently. The translational energies associated with J'=0, v'=0 BrO were obtained using forward-convolution fits of the speed distributions. A single value for the bond dissociation energy to provide the best forward convolution fit to all the speed distributions associated with the Br($^2P_{3/2}$) +O($^1D_2$) channel above the A $^2\Pi$ threshold. A value of 55.9 kcal/mol for the BrO bond dissociation energy provides consistent fits to the data.

In the second method, A plot of measured translational energy versus photon energy should yield a straight line for each asymptotic electronic channel with the

intercept of each line corresponding to the threshold of the respective channel based on the conservation of energy of the system given by Equation 5.1:

$$h\nu - D_0^0(BrO) + E_{e,v,r}^{BrO} = E_{avail} = E_{trans} + E_e^{Br} + E_e^O \qquad 5.1$$

where hν is the energy of the dissociation photon, $D_0^0(BrO)$ is the bond energy of BrO, E_e^{Br} and E_e^O are the spin-orbit energies of Br and O, respectively, and $E_{e,v,J}^{BrO}$ is the internal energy of the BrO prior to dissociation. Re-writing Equation 5.1 and assuming that $E_{e,v,J}^{BrO}$ is zero the equation becomes:

$$h\nu = E_{trans} + E_e^{Br} + E_e^O + D_0^0(BrO) \qquad 5.2$$

Using the images to determine E_{trans}, a linear fit of the E_{trans} vs. $h\nu$ produces an intercept equal to the bond dissociation energy plus the spin orbit energies of the Br and O fragments. Using wavelengths near the O(^{1}D) threshold, the velocities of the Br($^2P_{3/2}$) state will be very small, reducing the error in the measurement. The data presented by Kim *et al.* provides an A $^2\Pi_{3/2}$ dissociation threshold, corresponding to the threshold for formation of Br($^2P_{3/2}$) and O(^{1}D) fragments, of 35 418±35 cm^{-1}. Given the oxygen term value of 15 867.7 cm−1[161] corresponding to a ground state bond dissociation of 19551±35 cm^{-1} or 55.9±0.1 kcal/mol.

In the current study, we use the same method described above to provide another measurement of the bond dissociation energy of BrO. Because our data corresponds to the O(^3P_J) + Br(^2P_J) channels, the measurement was less precise due to the larger speeds of the O(^3P_J) fragments. Nevertheless, the bond dissociation energy derived from this data is 55.8 ± .4 kcal/mol which is within the error bounds of the previous measurement. Because the speed to pixel calibration can change from day to day based on ion optic voltage fluctuations, pixels were used instead of velocity calculate a value that is proportional to E_{trans}. This became the independent variable while the photon energy minus the spin orbit energies of the oxygen and bromine fragments became the independent variable. In this way, the intercept of a linear fit will still produce the bond dissociation energy of BrO. The plots of these data points, their linear fits, and the equation of best fit are shown in Figure 42.

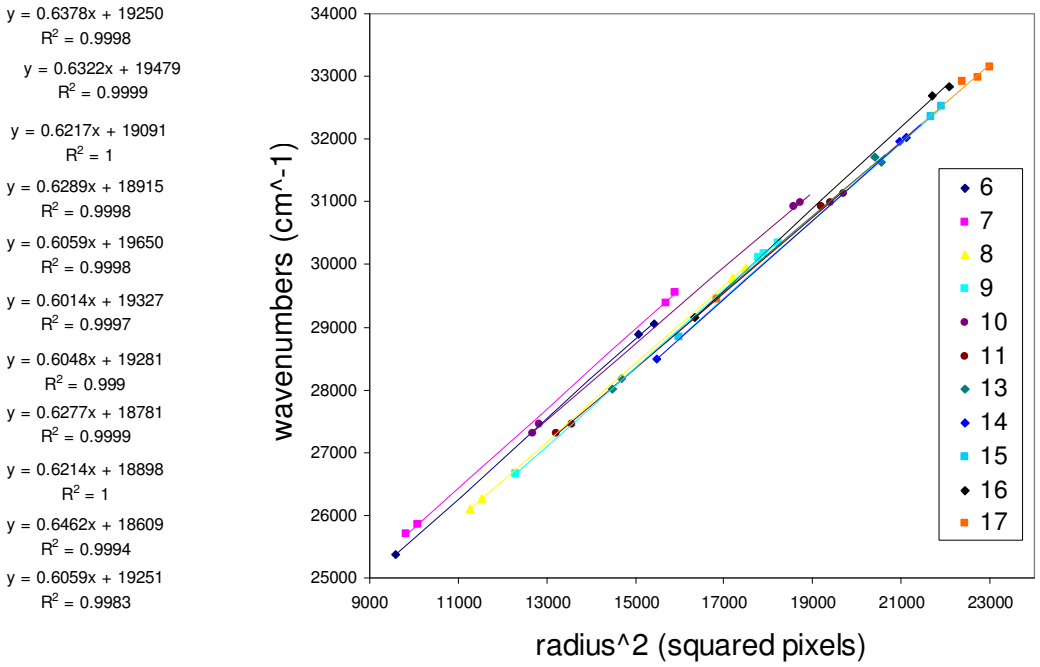

Figure 42: Plot providing measurements of the bond dissociation energy of BrO. The legend gives the v' level of each data point. The linear regressions on the left are in order, starting at the top, for v'=6-17.

Theoretical Treatment

The theoretical treatment of the BrO is very similar to the treatment described in Chapter IV for the ClO system. BCONT, developed by LeRoy[137] and described in more detail in Chapter IV, was used to calculate the v'-dependent predissociation lifetimes based on the coupling constants and the potential energy curves calculated by K. Peterson.[152] These were then used to calculate the final state correlated branching ratios for each vibrational level using the diabatic and adiabatic limits.

In the ClO case, the potentials and coupling constants were adjusted to achieve a best fit of the experimental v'-dependent predissociation lifetime data using an amoeba program described in Chapter IV. This provided us with the assurance that the potentials and coupling constants used correctly predicted the Franck-Condon region before extending our predictions to the exit channel. Fitting the well-established lifetime data

enables us to more confidently use the calculated potentials and coupling constants when using them to predict the branching ratios allowing us to comment on the effects of exit-channel coupling on the system. Unfortunately, the adjustment procedure used on the potentials and coupling constants for the ClO case is not useful for the BrO system as there are only two bands (v'= 7 and 12) that have published lifetime measurements due to the extremely short predissociation lifetime of the other vibrational bands which causes a lack of rotational resolution. The published lifetimes of these bands are 2.65, and 0.66 ps for the v' = 7 and 12 bands, respectively.[149] It was noted in Reference 148 that the v' = 4 level has some rotational structure, so we can assume that the lifetime of this band is somewhat long allowing us to assume that it also is a minimum predissociation rate. The predissociation rates of these bands have been used to constrain the potentials, but do not provide the level of confidence achieved in the ClO case where the lifetimes of numerous vibrational bands are accurately measured. Instead of using the amoeba program used to adjust the ClO potentials and coupling constants, the potentials have been adjusted by hand. The coupling constants used by the BCONT program to calculate the predissociation rates for each repulsive potential that crosses the A $^2\Pi_{3/2}$ state were calculated by K. Peterson.[152] These coupling constants are used as reported by K. Peterson with no adjustment, and are listed in Table 8.

Table 8: BrO potentials and coupling constants (cm^{-1}) used to calculate the v'-dependent correlated branching ratios. Calculated coupling constants are from Reference 108. These values were used to calculate the predissociation rates for each vibrational level using BCONT.

BrO Repulsive Potential	Calculated Coupling Constant
$1\,^2\Delta$	80
$1\,^4\Delta$	400
$1\,^4\Sigma^+$	200
$1\,^4\Sigma^-$	650
$1\,^4\Pi$	40
$2\,^4\Pi$	70
$3\,^2\Pi$	220

The fitting process for the potentials is quite rudimentary, and a description of the process follows. Because the 4, 7, and 12 vibrational bands are the only ones with measurable rates, we deduce that they must be minima in the predissociation rates for the bands. Because we have no further constraints on the model, the potentials were adjusted slightly so that the minima of the rates calculated using BCONT fell on the v' = 4, 7, and 12 levels. First, the ab initio bound A $^2\Pi_{3/2}$ state was shifted up in energy by 1600 cm^{-1}. Then, the unbound 1 $^4\Sigma^-$ state was shifted .01 Å to the left, toward shorter bond distances. These slight adjustments caused the calculated predissociation rates to have the correct minima. The predissociation rates calculated using BCONT are shown in Figures 43 and 44. Figure 43 shows the calculated rates using the original potentials, and Figure 44 plots the rates resulting from the slight shifts of the A $^2\Pi_{3/2}$ and the 1 $^4\Sigma^-$ states. This plot illustrates that although the minimum predissociation lifetimes are easily shifted to their appropriate positions with only slight adjustments made to the A $^2\Pi_{3/2}$ state and the coupling constants, more predissociation lifetimes are needed in order to fully constrain the overall shape of the calculated lifetimes.

The "Overall" vibrational level dependent rate is influenced mostly by the 1 $^4\Sigma^-$ state due to its very large coupling constant. As is evident from the "Overall" trace in Figure 43, the calculated lifetimes are much larger than the previously reported spectroscopic values. This is due to the calculated coupling constants being too large. However, because the actual values of the vibrational level dependent predissociation rates is not known over more bands, the shape of the calculated "overall" rate cannot be constrained. The shape of the overall rate is extremely important to the adjustment of the coupling constant. Therefore, to lower the overall rate to better fit the rates of the 4, 7, and 12 vibrational bands, it is suggested that the coupling constants all be lowered by a common factor such that the weighting established by the original ab initio calculation is not changed. Because this method does not change the weighting of the various repulsive states, the branching ratios that are calculated using the adiabatic and diabatic limits will not change.

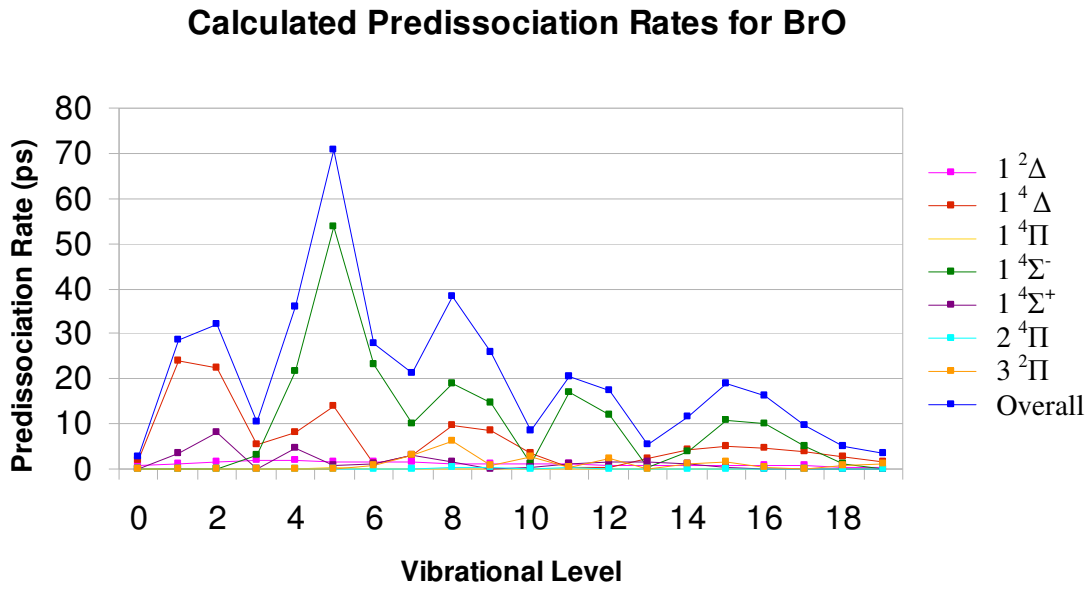

Figure 43: BCONT calculated v'-dependent predissociaiton rates for the A $^2\Pi_{3/2}$ state of BrO. These rates are calculated using the original potentials as calculated by Peterson in reference 152. Each repulsive state's individual contribution to the overall predissociation rate of each vibrational level is shown. "Overall" denotes the sum of all of the repulsive potential contributions.

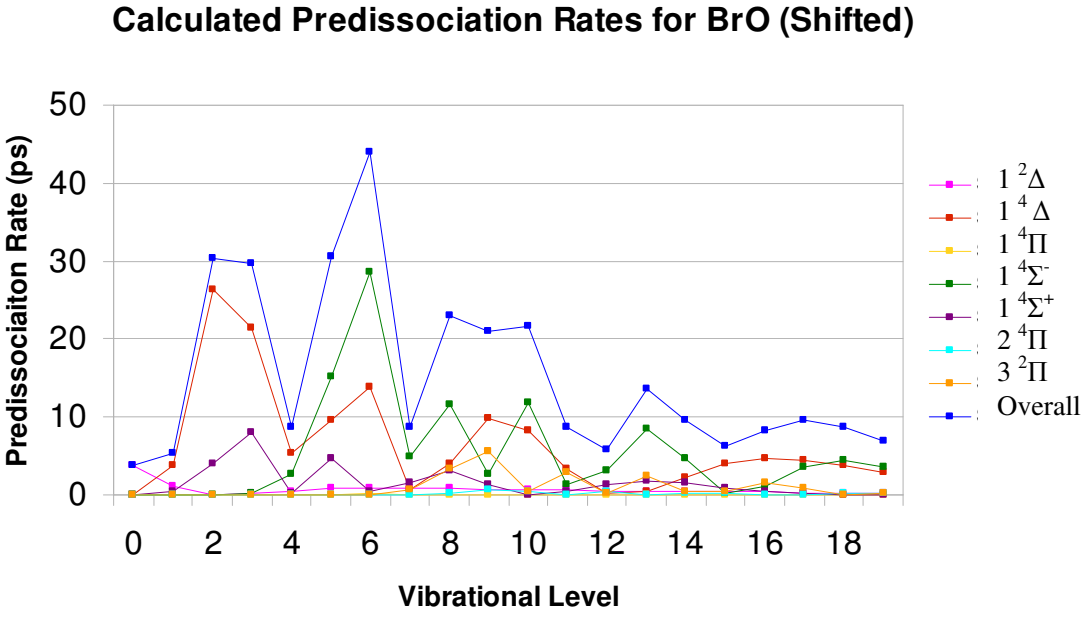

Figure 44: BCONT calculated vibrational level dependent predissociation rates using shifted potentials. Potentials are shifted as described in the text.

Vibrational level dependent final state branching ratios were calculated using the same diabatic matrix of state weightings as listed previously in Table 5. The adiabatic correlation diagram lists the states in order of increasing energy in the Franck-Condon region. Therefore, if the potentials shift, this diagram will change which could change the calculated branching ratios in this limit significantly. The results of the adiabatic and diabatic limits are provided in Tables 9 and 10.

Table 9: Calculated vibrational level dependent branching ratios for the predissociation of the A $^2\Pi_{3/2}$ of BrO using the adiabatic limit.

	$Cl(^2P_{3/2}) + O(^3P_2)$	$Cl(^2P_{1/2}) + O(^3P_2)$	$Cl(^2P_{3/2}) + O(^3P_1)$	$Cl(^2P_{1/2}) + O(^3P_1)$	$Cl(^2P_{3/2}) + O(^3P_0)$	$Cl(^2P_{1/2}) + O(^3P_0)$
0	0.0187	0.9801	0.0000	0.0000	0.0011	0.0000
1	0.7174	0.2181	0.0000	0.0000	0.0645	0.0000
2	0.8681	0.0029	0.0000	0.0000	0.1290	0.0000
3	0.7207	0.0111	0.0000	0.0000	0.2683	0.0000
4	0.6058	0.3791	0.0000	0.0000	0.0151	0.0000
5	0.3140	0.5297	0.0000	0.0001	0.1563	0.0000
6	0.3137	0.6758	0.0000	0.0010	0.0095	0.0000
7	0.0788	0.6758	0.0000	0.0665	0.1768	0.0000
8	0.1733	0.5396	0.0000	0.1455	0.1340	0.0000
9	0.4737	0.1653	0.0000	0.2688	0.0614	0.0000
10	0.3801	0.5800	0.0000	0.0171	0.0015	0.0000
11	0.3800	0.2327	0.0000	0.3340	0.0483	0.0000
12	0.0477	0.6296	0.0000	0.0251	0.2375	0.0000
13	0.0311	0.6579	0.0000	0.1763	0.1294	0.0000
14	0.2457	0.5328	0.0000	0.0461	0.1618	0.0000
15	0.6424	0.0940	0.0000	0.0802	0.1487	0.0000
16	0.5820	0.1774	0.0000	0.1869	0.0513	0.0000
17	0.4809	0.4148	0.0000	0.0872	0.0124	0.0000
18	0.4329	0.5445	0.0000	0.0062	0.0008	0.0000
19	0.4092	0.5543	0.0000	0.0179	0.0020	0.0000

Although the branching ratios calculated in the adiabatic limit are significantly different from those measured in this study, there are some general statements that can be made about this model. First, the $Cl(^2P_{1/2}) + O(^3P_0)$ state is not present in the

calculated results which is consistent with our experimental results. Second, the $Cl(^2P_{3/2}) + O(^3P_1)$ channel is absent in the modeled results for all vibrational levels. This is very inconsistent with our findings as this channel is present at every band we measured. In contrast, the $Cl(^2P_{1/2}) + O(^3P_1)$ channel shows a trend which is seen in our data (Figure 41). This channel is absent in both the model and our data at low vibrational levels ($v' \leq 6$). Although the adiabatic model does not predict that this channel should completely disappear at any level above $v' = 6$, it does predict fluctuations in the branching that are very near zero at some levels. From the images in Figure 41, and the values in Table 7, it can be seen that we observe similar fluctuations in the branching of this channel, and the actual vibrational levels where the branching ratio minima exist are correct or very close in all cases although the magnitude of the maxima are predicted to be much higher than is actually observed.

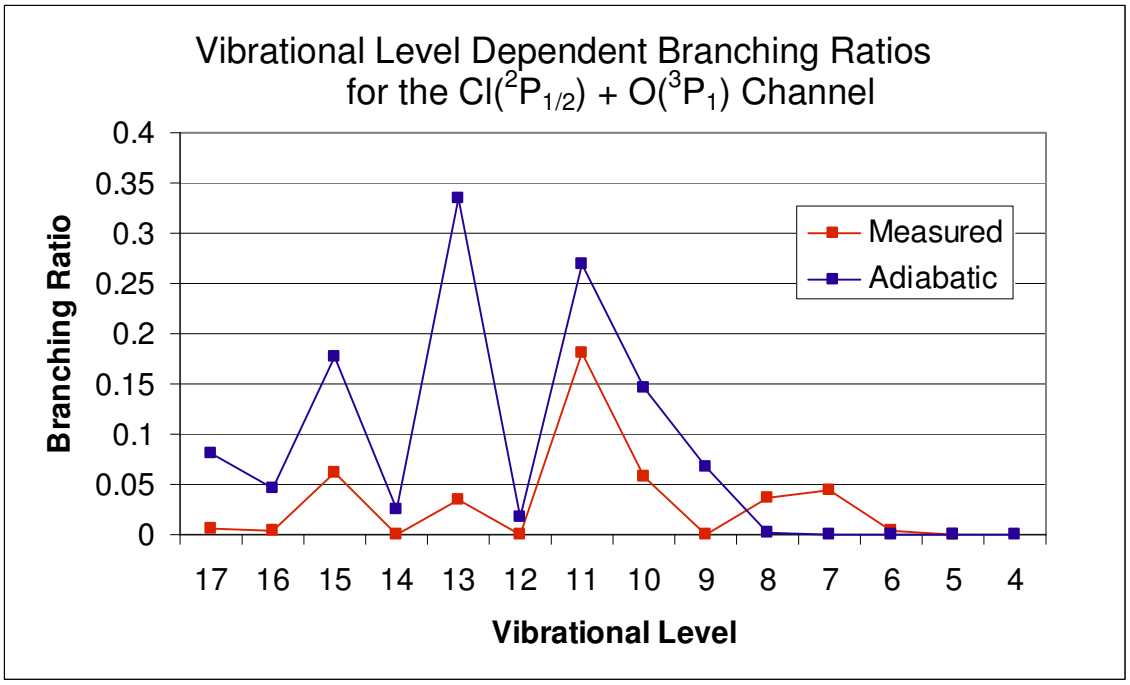

Figure 45: Vibrational level dependent branching ratios for the $Cl(^2P_{1/2}) + O(^3P_2)$ channel. This plot shows both the measured branching ratios as well as the modeled branching ratios using the adiabatic limit.

Table 10 shows the results of the vibrational level dependent correlated branching ratios as modeled in the diabatic limit. Similar to the case of ClO, this model predicts that all channels are present except for the $Cl(^2P_{1/2}) + O(^3P_0)$ channel which is consistent with most of the data that we have collected for this system. However, in some cases we see that the $Cl(^2P_{1/2}) + O(^3P_1)$ channel is absent which is not predicted by the diabatic limit. This observation is better predicted by the adiabatic limit.

Table 10: Calculated vibrational level dependent branching ratios for the predissociation of the A $^2\Pi_{3/2}$ of BrO using the diabatic limit.

	$Cl(^2P_{3/2}) + O(^3P_2)$	$Cl(^2P_{1/2}) + O(^3P_2)$	$Cl(^2P_{3/2}) + O(^3P_1)$	$Cl(^2P_{1/2}) + O(^3P_1)$	$Cl(^2P_{3/2}) + O(^3P_0)$	$Cl(^2P_{1/2}) + O(^3P_0)$
0	0.1668	0.1134	0.3867	0.1131	0.2201	0.0000
1	0.1721	0.2051	0.3002	0.1836	0.1389	0.0000
2	0.1775	0.2362	0.2745	0.1932	0.1186	0.0000
3	0.1899	0.2520	0.2708	0.1610	0.1264	0.0000
4	0.2035	0.2349	0.2841	0.1589	0.1187	0.0000
5	0.2358	0.2645	0.2764	0.1005	0.1228	0.0000
6	0.2409	0.2575	0.2796	0.1082	0.1139	0.0000
7	0.2580	0.2717	0.2795	0.0625	0.1283	0.0000
8	0.2617	0.2803	0.2678	0.0760	0.1143	0.0000
9	0.2442	0.2649	0.2571	0.1305	0.1033	0.0000
10	0.2401	0.2486	0.2746	0.1233	0.1135	0.0000
11	0.2470	0.2750	0.2640	0.1114	0.1026	0.0000
12	0.2758	0.2615	0.2650	0.0645	0.1333	0.0000
13	0.2787	0.2908	0.2669	0.0513	0.1125	0.0000
14	0.2478	0.2661	0.2725	0.0910	0.1228	0.0000
15	0.2104	0.2389	0.2675	0.1614	0.1219	0.0000
16	0.2182	0.2562	0.2701	0.1472	0.1083	0.0000
17	0.2270	0.2526	0.2749	0.1350	0.1105	0.0000
18	0.2318	0.2457	0.2768	0.1316	0.1142	0.0000
19	0.2350	0.2475	0.2761	0.1275	0.1139	0.0000

D. Summary

The final correlated state branching ratios have been experimentally measured for the predissociation of the v'=4-18 levels of the BrO A $^2\Pi_{3/2}$ state. Similar to the case of ClO, the branching ratios are seen to be non-statistical. However, the branching ratios are much different than that of ClO. In particular the O($^3P_1$) fragment observed across the BrO vibrational states is much different than that state observed along the ClO vibrational states. In ClO, the O($^3P_1$) + Cl($^2P_{1/2}$) channel is never observed. This channel is observed for BrO, and it is seen to appear and disappear as a function of vibrational level which provides insight into the positions and coupling of the excited state potentials.

CHAPTER VI

CONCLUSIONS AND FUTURE DIRECTIONS

This dissertation focused on molecular beam studies of the photodissociation dynamics of halogen monoxide radicals using velocity map ion imaging. Velocity map ion imaging is a powerful tool for the study of molecular dynamics allowing the collection of the entire Newton sphere, which provides simultaneous angular and speed information in a single measurement. Great detail about a reaction can be learned through this technique. Through velocity map ion imaging, information about the energetics of a reaction or molecule can be determined. For instance, the internal energy of the reactant and product species can be measured, or in the case of the reactant, even prepared, and using 2+1 REMPI detection, the measurements made are specific to a particular electronic state. Accurate bond dissociation energies of diatomic species can also be determined. In the studies reported here, velocity map ion imaging has been used to provide a direct measurement of the bond dissociation energy of IO. One of the greatest advantages of velocity map ion imaging is that it provides information about the unseen fragment allowing one to measure correlated scalar distributions. In the studies described in this dissertation, the potential of the correlated measurement has been exploited to measure the correlated fine structure branching ratios for the predissociation of ClO and BrO.

A description of the instrumentation and commentary about recent modifications are the focus of Chapter II. Modifications have been made in the data collection and analysis methods as well as the focusing ion optics. These modifications have provided several advantages. The ion optic assembly allows DC-slicing capability which requires no reconstruction, allowing images without cylindrical symmetry to be analyzed. It also circumvents the added noise to the data attributed to reconstruction methods. Other modifications include data collection software that calculates a megapixel image in real time, improving on the centroiding, the conventional method of event counting. The

purpose of these modifications is to increase velocity resolution in the images collected by the instrument. Unfortunately, the data shown in Chapters III-V do not take full advantage of these modifications. We are optimistic that the full potential of these modifications will be exploited in future endeavors.

Chapter III discusses the direct measurement of the bond dissociation energy of the IO radical species. This was the first instance of IO being seeded into a molecular beam which was possible through a late-mixing dual pulsed valve photolytic nozzle. The production of a molecular beam of IO was non-trivial. It required ideal conditions and introduces a myriad of potential challenges from the timing of three lasers to multiple pulsed valve delays and opening times. We are able to not only form molecular beams of these transient species, but we are able to make accurate and relevant measurements of IO photochemistry. The bond dissociation energy measurement is one of the most fundamental physical measurements that can be made of a diatomic species. However, until now, the best measurements of the IO bond dissociation energy relied on combining kinetic data with the thermodynamic constants of other species such as BrO. The error bounds associated with these calculations are large, causing the error bounds on the recommended value of the bond dissociation energy of IO to be at best about ±1 kcal/mol. Acquiring accurate thermodynamic parameters are critical for atmospherically relevant reactions involving IO which are near thermoneutral. One example of this is the IO + BrO reaction that could proceed via several pathways, most of these pathways are near thermoneutral and have large errors associated with their enthalpies of reaction which makes it difficult to determine which pathways are actually favorable. For this reason, the bond dissociation energy of IO is very important to the atmospheric modeling community –especially for modeling in the marine boundary layer where up to 50% of the average daily ozone loss has been attributed to iodine and bromine, or in the stratosphere after certain weather events such as typhoons.[162, 22]

Chapters IV and V outline the measurement of correlated final state branching ratios for ClO and BrO. These measurements are valuable to the molecular dynamics community as they provide a rigorous assessment of the validity of the current state of

theoretical calculations. A review by Butler notes that most of the work in the field of molecular dynamics is theoretical and that there is a need for detailed experimental data in order to gauge the state of the field and improve the current modeling. This is particularly true for systems that exhibit non-Born-Oppenheimer dynamics.[163] This parity of information results from the lack of techniques that allow for the measurement of detailed information of both the reactants and the products. Velocity map ion imaging is a novel technique that provides detailed, internal state correlated information.

ClO and BrO are perfect molecules to study as benchmarks for comparison to theory. They are small, making theoretical calculations from first principles possible, yet, due to the spin orbit coupling of the large halogen atom, full calculations of the potential energy surfaces and coupling constants remain challenging. Studying the dynamics, especially the final correlated state branching ratios of the predissociation of the A $^2\Pi_{3/2}$ state of ClO and BrO, provides insight into the potential energy surfaces and the coupling between the bound A $^2\Pi_{3/2}$ state and the many unbound electronic states that cross it. The results of these experiments on a qualitative level support the idea that the ClO predissociation should be more diabatic, while the BrO predissociation is better described in the adiabatic limit. However, our measurements show that there are differences between the limiting models and the experimental results. This is likely the result of exit-channel coupling in the predissociating potentials. The measurements highlight the need for a better model to describe the predissociation of these systems.

Because velocity map ion imaging is a versatile technique, there are many possibilities for future directions. The work described in this dissertation provides a foundation for numerous new studies which fall under two broad categories based on their relevance: those that are atmospheric in nature, and those that focus on understanding fundamental chemical physics.

One possibility of an atmospherically relevant study would concentrate on understanding the photodissociation dynamics of the ClO dimer. This species is known to play a role in the springtime destruction of Antarctic ozone.[164, 165] The photolysis of the ClO dimer has been implicated in significant ozone loss through the mechanism:

$$ClO + ClO + M \rightarrow Cl_2O_2 + M \quad (6.1)$$

$$Cl_2O_2 + h\nu \rightarrow Cl + ClOO \quad (6.2)$$

$$ClOO + M \rightarrow Cl + O_2 + M \quad (6.3)$$

$$2(Cl + O_3 \rightarrow O_2 + ClO) \quad (6.4)$$

Overall: $2O_3 \rightarrow 3\ O_2$ (6.5)

where M is any other molecule.[166] Understanding the wavelength dependent branching ratio of the photolysis of Cl_2O_2 would be very useful for modeling the chemistry during these ozone destruction events. Cl_2O_2 can dissociate via the following pathways:

$$Cl_2O_2 + hv \rightarrow ClO + ClO \quad (6.6)$$

$$Cl + ClOO \quad (6.7)$$

$$2Cl + O2 \quad (6.8)$$

$$Cl + O + ClO \quad (6.9)$$

Since ClO is inert to ozone, the wavelength dependent relative branching of Cl/ClO is critical in ozone destruction. It was recently reported that channel 6.8 is the major channel for photolysis of Cl_2O_2 at 248 nm and 303 nm.[167] Knowing how often the photolysis result given in Equation 6.2 occurs would be very useful in knowing the importance of the mechanism proposed. This is an especially relevant topic currently as Cl_2O_2 has been the center of much debate in the past year concerning its absorption spectrum which is an integral piece of data that dictates the way that the ozone destruction events are understood.[168] A major experimental concern is the difficulty of producing a Cl_2O_2 molecular beam. It is possible that either a pyrolytic or photolytic assembly similar to the ones described in this text could be used to produce ClO which would then be passed through a cold portion of the nozzle to cause the ClO to form the dimer species.

Another future experiment that would have atmospheric relevance would be to study the photodissociation of OBrO. The concentration of OBrO in the midlatitude stratosphere was spectroscopically measured to be as high as 20 pptv at night.[169] This

measurement makes OBrO the major nighttime bromine reservoir. The absorption spectrum of OBrO is shown in Figure 46, below.

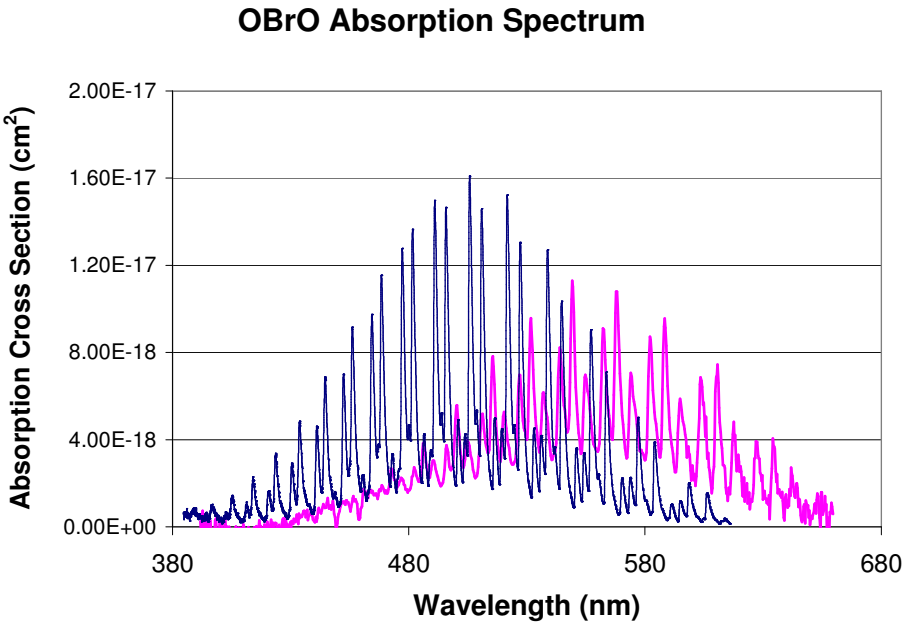

Figure 46: Absorption spectra of OBrO (blue trace) and OIO (pink trace) species. OBrO spectrum adapted from Reference 170. OIO spectrum is adapted from 171.

OBrO dissociates by the following mechanism:

$$OBrO + h\nu \rightarrow Br + O_2 \qquad (6.10)$$

$$\rightarrow O + BrO \qquad (6.11)$$

The channel shown in 6.10 would initiate ozone destruction by releasing a bromine atom. The channel shown in 6.11 would actually form ozone through the reaction of the odd oxygen with an oxygen atom. Understanding the branching ratios of these two channels and their wavelength dependence is important to the accuracy of current

atmospheric modeling. In a recent theoretical study, it was reported that the O + BrO channel has a threshold of near 485 nm.[172] At wavelengths below this, the O + BrO channel is believed to be dominant.

Similar investigations of OIO would also be interesting. The long wavelength threshold for photodissociation to form O + IO is near 435 nm, below the observed absorption spectrum for OIO (Figure 46). For this reason, the OIO species is believed to be a stable reservoir for iodine with a slow photolysis rate in the visible region.[173] Understanding the dynamics of the photolysis of OIO would be extremely useful to modeling iodine chemistry as other iodine reservoir species are highly unstable.

From a fundamental standpoint, investigation of orbital alignment effects of ClO and BrO would be intriguing. The dissociation of ClO or BrO will produce fragments with their angular momenta aligned either perpendicular or parallel to the recoil axis. The alignment gives insight into the nature of the dissociation and provides a much more detailed probe of the photodissociation dynamics. For example, ion imaging has been used to study the alignment effects of the $O(^1D)$ fragment from the photodissociation of O_2 by Eppink *et al.* [174] Also, the v-J correlations of Cl_2 photodissociation were examined using the ion imaging technique by Bracker *et al.*[175] The fragment atoms had angular momenta aligned perpendicular to the fragment recoil axis predicting an adiabatic transition.

Another experiment that is interesting on a fundamental level is the determination of the predissociation lifetimes of BrO through an anisotropy measurement. The predissociation lifetimes of most of the v' levels of BrO are unable to be determined by spectroscopy due to the lack of rotational structure. Therefore, the estimation of the lifetimes is possible through the measurement of the J'-dependent anisotropy parameter for the vibrational bands.

The measured anisotropy parameter is related to the lifetime by the following expression based on the semi-classical model by Jonah who calculated for a parallel transition[176]:

$$I(\theta) = \frac{\cos^2(\theta)(\tau\omega + 1/\tau\omega) + \tau\omega}{4\tau\omega + 1/\tau\omega} \qquad (6.12)$$

where τ is the lifetime of the molecule and ω is the classical angular frequency of the molecule. This expression assumes that the P, Q and R branches of the transition are excited equally, and thus provides only an estimation of the lifetime in cases where only single or subsets of rotational transitions are excited. Using this expression, it can be seen that as the lifetime goes to zero, the anisotropy parameter goes to the limiting value of 2.0, and as it becomes large, the anisotropy parameter drops to a lower limit of 0.5.

Houston and coworkers recently developed a program that calculates the anisotropy parameter as a function of wavelength for a given transition based on spectroscopic data used as input.[103] More details about the betaofnu program can be found in Chapter IV. It was seen in that paper that the anisotropy parameter of a parallel transition decreases as you move across the J' states of a transition and is highly dependent on the lifetime. Therefore, by using measured anisotropy parameters from across the vibrational band, it is possible to approximate the predissociation lifetime of the vibrational level by fitting the anisotropy data as a function of wavelength with calculated anisotropy parameters from betaofnu.

These are just a few of the many exciting experiments that velocity map ion imaging is capable of performing. As is evident, this method can be used to study many systems which are interesting to a variety of fields. Velocity map ion imaging can reach into many fields due to the numerous types of data, and the state-correlated nature of the data, that can be obtained by this method.

REFERENCES

[1] M. Pidwirny, *et al.*, (2008). Atmosphere layers. Retrieved 2009 from Encyclopedia of Earth (Eds. C. J. Cleveland) website: http://www.eoearth.org/article/Atmosphere_layers.

[2] S. Chapman, Mem. Roy. Meteorol. Soc. **3**, 103 (1930)

[3] J. P. Burrows, A. Richter, A. Dehn, B. Deters, S. Himmelmann, S. Voigt, and J. Orphal, J. Quant. Spectrosc. Radiat. Transfer, **61**, 509-517, (1999).

[4] W. N. Hartley, J. Chem. Soc., Trans., **39**, 111, (1881).

[5] W. N. Hartley, J. Chem. Soc., Trans., **39**, 57, (1881).

[6] W. Huggins and Mrs. Huggins , Proc. R. Soc. London, **48**, 216 (1890).

[7] J. Chappuis, Comptes Rendus Hebdomadaires des Seances de l'Academie des Sciences, **94**, 858, (1882).

[8] P. J. Crutzen, Q. J. R. Meteorol. Soc., **96**, 320, (1970).

[9] R. A. Rohde (2007). Solar Spectrum. Retrieved 2009 from Global Warming Art website: globalwarmingart.com

[10] D. R. Bates, and P. B. Hays, Planet. Space Sci.,**15**, 189, (1967).

[11] G. D. Greenblatt, A. R. Ravishankara, J. Geophys. Res., **95**, 3539, (1990).

[12] M. B. McElroy, and J. C. McMonnell, J. Atmos. Sci., **28**, 1095, (1971).

[13] C. A. Cantrell, R. E. Shetter, and J. G. Calvert, J. Geophys. Res., **99**, 3739, (1994).

[14] H. Johnston, Science, **173**, 517, (1971).

[15] R. J. Cicerone, and R. S. Stolarski, Can. J. Chem., **52**, 1610, (1974).

[16] World Meteorological Organization (WMO), "Scientific Assesment of Ozone Depletion: 1994," Global Ozone Research and Monitoring Project, Report No. 37, Feb. 1995; update, Report No. 44, Feb. 1999.

[17] J. A. Kaye, S. A. Penkett, and F. M. Ormund, NASA Reference Publication No. 1339 (1994).

[18] S. A. Montzka, J. H. Butler, R. C. Myers, T. M. Thompson, T. H. Swanson, A. D. Clarke, L. T. Lock, and J. W. Elkins, Science, **272**, 1318 (1996).

[19] S. A. Montzka, R. C. Myers, J. H. Butler, J. W. Elkins, L. T. Lock, A. D. Clarke, and A. H. Goldstein, Geophys. Res. Lett. **23**, 169 (1996).

[20] D. J. Lary, J. Geophys. Res. **101**, 1505 (1996).

[21] P. O. Wennberg, J. W. Brault, T. F. Hanisco, R. J. Salawitch, G. H. Mount, J. Geophys. Res., **102**, 8887, (1997).

[22] S. Solomon, R. R. Garcia, and A. R. Ravishankara, J. Geophys. Res., **99**, 20491, (1994).

[23] I. Pundt, J.-P. Pommereau, C. Phillips, and E. Lateltin, J. Atmos. Chem., **30**, 173, (1998).

[24] D. Davis, J. Crawford, S. Liu, S. McKeen, A. Bandy, D. Thornton, F. Rowland, and D. Blank, J. Geophys. Res., **101**, 2135, (1996).

[25] B. Alicke, K. Hebestreit, J. Stutz, and U. Platt, Nature, **397**, 572, (1999).

[26] R. Schinke, *Photodissociaiton Dynamics*. (Cambridge University Press, Cambridge 1993).

[27] P. P. Sorokin and J. R. Lankard, Stimulated emission, IBM J. Res. Develop., **10**, 162, (1966).

[28] F. P. Schäfer, W. Schmidt, J. Volze, Appl. Phys. Lett., **9**, 306, (1966).

[29] L. J. Butler, D. M. Neumark, J. Phys. Chem., **100**, 12801, (1996).

[30] G. E. Hall, and Houston, Annu. Rev. Phys. Chem., **40**, 375, (1989).

[31] A. J. R. Heck, D. W. Chandler, Annu. Rev. Phys. Chem., **46**, 335, (1995).

[32] M. Shapiro, and R. Bersohn, Annu. Rev. Phys. Chem., **33**, 409, (1982).

[33] A. R. Ravishankara, G. Hancock, M. Kawasaki, and Y. Matsumi, Science, **280,** 5360, 60, (1998).

[34] S. P. Sander and R. R. Friedl, J. Phys. Chem. **93**, 4764, (1989).

[35] D. M. Wilmouth, T. F. Hanisco, N. M. Donahue, and J. G. Anerson, J. Phys. Chem. A **103**, 8935, (1999).

[36] P. Spietz, J. C. Gomez Martin, and J. P. Burrows, J. Photochem. Photobiol. A: Chem. **176**, 50, (2005).

[37] R. T. Birge and H. Sponer, Phys. Rev., **28**, 259, (1926).

[38] G. E. Busch, and K. R. Wilson, J. Chem. Phys., **56**, 3626, (1972).

[39] W. H. Howie, I. C. Lane, S. M. Newman, D. A. Johnson and A. J. Orr-Ewing, Phys. Chem. Chem. Phys., **1**, 3079, (1999).

[40] A. Toniolo, M. Persico and D. Pitea, J. Chem. Phys., **112**, 2790, (2000).

[41] D. W. Chandler, and P. L. Houston, J. Chem. Phys., **87**, 1445, (1987).

[42] A. T. J. B. Eppink and D. H. Parker, Rev. Sci. Instrum., **68**, 3477, (1997).

[43] H. Kim, "Imaging Studies of the Photochemistry of Stratospheric Bromine and Chlorine Compounds" Diss. Texas A&M University, 2006.

[44] A. Eppink, and D. H. Parker, Rev. Sci. Instrum., **68**, 3477, (1997).

[45] B. Whitaker, ed., *Imaging in Molecular Dynamics: Technology and Applications*, (Cambridge University Press, New York, NY, 2003).

[46] L. J. Butler, and D. M. Neumark, J. Phys. Chem., **1996**, 100, 12801.

[47] G. E. Hall, P. L. Houston, Annu. Rev. Phys. Chem., **40**, 375, (1989).

[48] R. N. Zare, Mol. Photochem. **4**, 1, (1972).

[49] W. Li, S. D. Chambreau, S. A. Lahankar, and A. Suits, Rev. Sci. Instrum., **76**, 063106, (2005).

[50] V. Dribinski, A. Ossadtchi, V. Mandelshtam, and H. Reisler, Rev. Sci. Instrum.

[51] pBasex

[52] D. J. Bamford, M. J. Dyke, and W. K. Bishel, Phys. Rev. A. **36**, 3497, (1987).

[53] S. Arepalli, N. Presser, D. Robie, and R. J. Gordon, Chem. Phys. Lett. **118**, 88, (1985).

[54] S. Arepalli, N. Presser, D. Robie, and R. J. Gordon, Chem. Phys. Lett. **117**, 64 (1985).

[55] C.E. Moore, Atomic Energy Levels, Natl. Stand. Ref. Data Ser., Natl. Bur. Stand. U.S. Circ 35, vol. 3, U. S. Government Printing Office, Washington, DC, 1971;
Y.J. Jung, Y.S. Kim, W.K. Kang, K.H. Jung, J. Chem. Phys. **107**, 7187 (1997).

[56] D. W. Chandler and P. L. Houston, J. Chem. Phys. **87**, 1445 (1987).

[57] A. T. Eppink and D. H. Parker, Rev. Sci. Instrum. **68**, 3447 (1997).

[58] D. Townsend, M. P. Minitti, and A. G. Suits, Rev. Sci. Instrum., **74**, 2530, (2003).

[59] K. Tonokura, T. Suzuki, Chem. Phys. Lett., **224**, 1, (1994).

[60] C. R. Gebhardt, T. P. Rakitzis, P. C. Samartzis, V. Ladopoulos, and T. N. Kitstopoulos, Rev. Sci. Instrum., **72**, 3848, (2001).

[61] D. A. Chestakov, S. M. Wu, G. R. Wu, D. H. Parker, A. T. J. B. Eppink, and T. N. Kitstopoulos, J. Phys. Chem., **108**, 8100, (2005).

[62] J. J. Lin, J. Zhou, W. Shiu, and K. Liu, Rev. Sci. Instrum., **74**, 2495, (2003).

[63] Simion 7 is a commercially available software that can be purchased at www.simion.com.

[64] B. Chang, R. C. Hoetzlein, J. A. Mueller, J. D. Geiser, P. L. Houston, Rev. Sci. Instrum, **70**, 3265, (1999).

[65] ImageJ is available at http://rsb.info.nih.gov/ij/

[66] V. Dribinski, A. Ossadtchi, V. Mandelshtam, and H. Reisler, Rev. Sci. Instrum.

[67] G. A. Garcia, L. Nahon, and I. Powis, Rec. Sci. Instrum., **75**, 4989, (2004).

[68] Contact information for Lionel Poisson who graciously made available the pBASEX code used in these studies: Laboratoire Francis Perrin, CEA, IRAMIS, Service des photons atomes et molécules—CNRS URA 2453, 91191 Gif-sur-Yvette Cedex, France.

[69] G. H. Cady, Inorg. Synth. **5**, 156 (1957).

[70] J. P. Camden, H. A. Bechtel, and R. N. Zare, Rev. Sci. Instrum. **75**, 556 (2004).

[71] L. Feng, X. Huang, H. Reisler. J. Chem. Phys. **117**, 4820 (2002).

[72] H. Kim, K. S. Dooley, E. R. Johnson, S. W. North, Rev. Sci. Instrum., **76,** 124101, (2005).

[73] T. A. Watson, M. Addison, C. Wittig, J. Chem. Phys., **78,** 57, (1983).

[74] T. L. Andreeva, S. V. Kuznetsova, A. I. Maslov, I. I. Sobel'man, V. N. Sorokin, High Energy Chem., **6**, 368, (1972).

[75] S. L. Dobychin, V. I. Mashendzhinov, V. I. Mishin, V. N. Semenov, V. S. Shpak, V, Dokl. Phys. Chem. (Engl. Transl.), **312**, 494, (1990).

[76] M. E. Tucceri, T. J. Dillon, J. N. Crowley, Phys. Chem. Chem. Phys., **7**, 1657, (2005).

[77]R. Atkinson, D. L. Baulch, R. A. Cox, J. N. Crowley, R. F. Hampson, R. G. Hynes, M. E. Jenkin, M. J. Rossi, J. Troe, Atmos. Chem. Phys.,**7**, 981, (2007).

[78] A. Vipond, C. E. Canosa-Mas, M. L. Flugge, D. J. Gray, D. E. Shallcross, D. Shah, R. P. Wayne, Phys. Chem. Chem. Phys., **4**, 3648 (2002).

[79] M. H. Harwood, J. B. Burkholder, M. Hunter, R. W. Fox, A. R. Ravishankara, J. Phys. Chem. A, **101**, 853, (1997).

[80] I. K. Larin, D. V. Nevozhai, A. I. Spasskii, E. M. Trofimova, L. E. Turkin, Kinet. Catal. (Engl. Transl.), **40**, 435 (1999).

[81] R. J. Donovan, D. Husain, Nature, 206, 171, (1965).

[82] Y. Bedjanian, G. Le Bras, G. Poulet, J. Phys. Chem. A., **102** (1998) 10501.

[83] R. T. Birge and H. Sponer, Phys. Rev. **28** (1926) 259.

[84] R. A. Durrie and D. A. Ramsay, Can. J. Phys. **36** (1958) 35.

[85] S. Roszak, M. Krauss, A. B. Alekseyev, H.-P. Liebermann, and R. J. Buenker, J. Phys. Chem. A. **104** (2000) 2999.

[86] E. H. Coleman, A. G. Gaydon, and W. M. Vaidya, Nature (London), **162** (1948) 108.

[87] R. B. Singh and D. K. Rai, Can. J. Phys. 43 (1965) 1985.

[88] V. M. Trivedi and V. B. Gohel, J. Phys. B. 5 (1972) L38.

[89] L. F. Phillips, and T. M. Sugden, Trans. Faraday Soc., **57**, (1961), 914.

[90] D. S. A. G. Radlein, J. C. Whitehead, and R. Grice, Nature, **253** (1975) 37.

[91] R. J. Buss, S. J. Sibener, and Y. T. Lee, J. Phys. Chem. **87** (1983) 4840.

[92] It should be noted that the value attributed to ref. 91 is based on a footnote within the manuscript based on unpublished data from the $O(^3P)$ + ICl reaction.

[93] K. A. Peterson, B. C. Shepler, D. Figggen, H. Stoll, J. Phys. Chem. A, **110** (2006) 13877.

[94] Y. Bedjanian, G. LeBras, G. Poulet, J. Phys. Chem. A **101** (1997) 4088.

[95] H. F. Davis and Y. T. Lee, J. Chem. Phys. **105** (1996) 8142.

[96] N. Kaltsoyannis, J. M. C. Plane, Phys. Chem. Chem. Phys., **10** (2008) 1723.

[97] N. Taniguchi, K. Takahashi, Y. Matsumi, S. Dylewski, J. Geiser, and P. L Houston, J. Chem. Phys. **111** (1999) 6350.

[98] A. V. Komissarov, M. P. Minitti, A. G. Suits and G. E. Hall, J. Chem. Phys. **124**, (2005) 014303.

[99] E. Wrede, S. Laubach, S. Sculenburg, A.J. Orr-Ewing and M.N.R. Ashfold, Chem. Phys. Lett. **326** (2000) 22.

[100] H. Kim, K. S. Dooley, E. R. Johnson, and S. W. North, J. Chem. Phys. **124** (2006) 134304.

[101] C. E. Moore, Atomic Energy Levels, Natl. Stand. Ref. Data Ser., Natl. Bur. Stand. U.S. Circ. 35 (U. S. Government Printing Office, Washington, D. C., 1971) Vol. III; Y. J. Jung, Y. S. Kim, W. K. Kang, K. H. Jung, J. Chem. Phys., **107** (1997) 7187.

[102] S.M. Newman, W.H. Howie, I.C. Lane, M.R. Upson, A.J. Orr-Ewing, J. Chem. Faraday Trans., **94,** 2681, (1998).

[103] H. Kim, K. S. Dooley, S. W. North, G. E. Hall, and P. L. Houston, J. Chem. Phys. **125** (2006) 133316.

[104] H. J. Hwang and M. A. El-Sayed, J. Phys. Chem., **95** (1991) 8044.

[105] D. A. Chestokov, D. H. Parker, K. V. Vidna, T. P. Rakitzis, J. Chem. Phys. **124** (2006) 024315.

[106] The very minor I($^2P_{3/2}$) + I ($^2P_{3/2}$) from dissociation at 304.67 nm can also be observed at higher extraction voltages.

[107] R. Atkinson, D. L. Baulch, R. A. Cox, R. F. Hampson, J. A. Kerr, M. J. Rossi, J. Troe, J. Phys. Chem. Ref. Data, **29** (2000) 167.

[108] K. A. Peterson (2008) Unpublished data.

[109] R. N. Zare, Mol. Photochem. **4** (1972) 1.

[110] S. Mukamel and J. Jortner, J. Chem. Phys. **61** (1974) 5348.

[111] M. W. Chase, Jr., C. A. Davies, J. R. Downey, Jr., D. J. Frurip, R. A. McDonald, A. N. Syverud, J. Phys. Chem. Ref. Data, **14**, (1985), Suppl. No. 1.

[112] Y. Bedjanian, G. Le Bras, and G. Poulet, Chem. Phys. Lett., **266**, 233 (1997).

[113]Y. Bedjanian, G. Le Bras, and G. Poulet, J. Phys. Chem. A **, 102**, 10501 (1998).

[114] M. J. Molina and F. S Rowland, Nature, 1974, **249**, 810.

[115] R. R. Garcia and S. Solomon, J. Geophys. Res., 1994, **99**, 12937.

[116] S. Solomon, R. R. Garcia, F. S. Rowland, and D. J. Wuebbles, Nature, 1996, **321**, 755.

[117] W. Zhou, Y. Yuan, and J. Zhang, J. Chem. Phys., 2003, **119**, 9989.

[118] G. Parlent and D. R. Yarkony, J. Chem. Phys., 1999, **110**, 363.

[119] R. A. Durie and D. A. Ramsay, Can. J. Phys., 1958, **36**, 35.

[120] J. A. Coxon and D. A. Ramsay, Can. J. Phys., 1976, **54**, 1034.

[121] P. W. McLoughlin, C. R. Park, and J. R. Weisenfeld, J. Mol. Spectrosc., 1993, **162**, 307.

[122] M. Trollier, R. L. Mauldin III, and A. R. Ravishankara, J. Phys. Chem., 1990, **94**, 4896.

[123] W. H. Howie, I. C. Lane, S. M. Newman, D. A. Johnson, and A. J. Orr-Ewing, Phys. Chem. Chem. Phys., 1999, **1**, 3079.

[124] I. C. Lane, W. H. Howie, and A. J. Orr-Ewing, Phys. Chem. Chem. Phys., 1999, **1**, 3087.

[125] A. Toniolo, M. Persico, and D. Pitea, J. Chem. Phys., 2000, **112**, 2790.

[126] Lane, I. C., Howie, W. H., and Orr-Ewing, A. J., Phys. Chem. Chem. Phys., **1**, 3087, (1999).

[127] H. F. Davis and Y. T. Lee, J. Phys. Chem., 1996, **100**, 30.

[128] P. Zou, H. Kim, and S. W. North, J. Chem. Phys., 2002, **116**, 4176.

[129] H. Kim, J. Park, T. C. Niday, and S. W. North, J. Chem. Phys., 2005, **123**, 174303.

[130] S. Schmidt, Th. Benter, and R. N. Schindler, Chem. Phys. Lett., 1998, **282**, 292.

[131] R. Flesch, J. Plenge, S. Kühl, M. Klusmann, and E. Rühl, J. Chem. Phys., 2002, **117**, 9663

[132] H. Kim, K. S. Dooley, G. C. Groenenboom, and S. W. North, Phys. Chem. Chem. Phys., 2006, **8**, 2964.

[133] D. J. Banford, L. E. Jusinsk, and W. K. Bischel, Phys. Rev. A, **34**, 185, (1986).

[134] D. J. Bamford, L. E. Jusinski, W. K. Bischel, Phys. Rev. A, 1986, **34**, 185.

[135] P. L. Houston, G. E. Hall, H. Kim, K. S. Dooley, and S. W. North, Phys. Chem. Chem. Phys., **125**, 133316, (2007).

[136] The 'betaofnu.exe' program is a result from Ref. 28 and is available for download from http://www.cosbkup.gatech.edu/group/Betaofnu.htm

[137] R. J. LeRoy, Comput. Phys. Commun. 1989, **52**, 383.

[138] R. J. LeRoy, University of Waterloo Chemical Physics Report CP-650R, 2004.

[139] M. C. G. N. Vroonhoven and G. C. Groenenboom, J. Chem. Phys. 2002, **116**, 1954.

[140] M. C. G. N. Vroonhoven and G. C. Groenenboom, J. Chem. Phys. 2002, **116**, 1965.

[141] R. A. Cox, D. W. Sheppard, and M. P. Stevens, J. Photochem., 19, **189**, (1982).

[142] W. M. Vaidya, Proc. Indian Acad. Sci., Sect. A, **7**, 321 (1938).

[143] E. H. Coleman and A. G. Gaydon, Discuss. Faraday Soc., **2**, 166, (1947).

[144] R. A. Durrie and D. A. Ramsay, Can. J. Phys., **36**, 35, (1958).

[145] M. Barnett, E. A. Cohen, and D. A. Ramsay, Can. J. Phys., **59**, 1908, (1981).

[146] A. Wahner, A. R. Ravishankara, S. P. Sander, and R. R. Friedel, Chem. Phys. Lett., **152**, 507, (1988).

[147] M. K. Gilles, A. A. Turnipseed, J. B. Burkholder, A. R. Ravishankara, and S. Solomon, J. Phys. Chem. A, **101**, 5526, (1997).

[148] M. D. Wheeler, S. M. Newman, T. Ishiwata, M. Kawasaki, and A. J. Orr-Ewing, Chem. Phys. Lett. **285**, 346 (1998).

[149] D. M. Wilmouth, T. F. Hanisco, N. M. Donahue, and J. G. Anerson, J. Phys. Chem. A **103**, 8935, (1999).

[150] J. S. Francisco, S. Parthiban, and T. J. Lee, J. Chem. Phys., **109**, 10818, (1998).

[151] Y. Li, J. S. Francisco, and K. A. Peterson, J. Chem. Phys., **113**, 8556, (2000).

[152] K. Peterson, unpublished study.

[153] P. Zou, H. Kim, and S. W. North, J. Chem. Phys., **116**, 4176, (2002).

[154] N. Taniguchi, K. Takahashi, Y. Matsumi, S. Dylewski, J. Geiser, and P. L. Houston, J. Chem. Phys., **111**, 6350, (1999).

[155] A. V. Komissarov, M. P. Minitti, A. G. Suits, and G. E. Hall, J. Chem. Phys., **124**, 014303, (2005).

[156] E. Wrede, S. Laubach, S. Sculenburg, A. J. Orr-Ewing, and M. N. R. Ashfold, Chem. Phys. Lett., **326**, 22, (2000).

[157] H. Kim, K. S. Dooley, E. R. Johnson, S. W. North, J. Chem. Phys., **124**, 134304, (2006).

[158] D. J. Banford, L. E. Jusinsk, and W. K. Bischel, Phys. Rev. A, **34**, 185, (1986).

[159] D. J. Bamford, L. E. Jusinski, W. K. Bischel, Phys. Rev. A, 1986, **34**, 185.

[160] O. C. Fleischmann, M. Hartmann, J. P. Burrows, and J. Orphal, J. Photochem. Photobiol., A, **168**, 117 (2004).

[161] W. G. Brown, Phys. Rev., **42**, 355, (1932).

[162] R. von Glasow, Nature, **453**, 1195, (2008).

[163] L. Butler, Annu. Rev. Phys. Chem, **49**, 125, (1998).

[164] R. L. deZafra, M. Jaramillo, A. Parrish, P. Solomon, B. Connor, and J. Barrett, Nature, **328**, 408 (1987).

[165] P. M. Solomon, B. Connor, R. L. deZafra, A. Parrish, J. Barrett, and M. Jaramillo, Nature, **328**, 411 (1987).

[166] L. T. Molina, M. J. Molina, J. Phys. Chem., **91**, 433 (1987).

[167] T. A. Moore, M. Okumura, J. W. Seale, and T. K. Minton, J. Phys. Chem. A, **103,** 1691 (1999).

[168] F. D. Pope, J. C. Hansen, K. D. Bayes, R. R. Friedl, and S. P. Sander, J. Phys. Chem. A, **111**, 4322, (2007).

[169] J.-B. Renard, M. Pirre, C. Robert, and D. Huguenin, C. R. Acad. Sci. Paris, Sci. Terre Planet., **325,** 921 (1997).

[170] O. C. Fleishman, J. Meyer-Arnek, J. P. Burrows, and J. Orphal, J. Phys. Chem. A., **109**, 5093 (2005).

[171] P. Spietz, J. C. Gomez Martin, and J. P. Burrows, J. Photochem. Photobiol. A: Chem., **176**, 50 (2005).

[172] R. Vetter, T. Ritschel, L. Zulicke, K. Peterson, J. Phys. Chem. A, **107**, 1405 (2003).

[173] T. Ingham, M. Cameron, and J. N. Crowley, J. Phys. Chem. A, **104**, 8001 (2000).

[174] A. Y. J. B. Eppink, D. H. Parker, M. H. M. Janssen, B. Buijsse, and W. J. van der Zande, J. Chem. Phys., **108**, 1305 (1998).

[175] A. S. Bracker, E. R. Wouters, A. G. Suits, Y. T. Lee, O. S. Vasyutinskii, Phys. Rev. Letts., **80**, 1626 (1998).

[176] C. Jonah, J. Chem. Phys. **55**, 1915, (1971).

VITA

Kristin S. Dooley received her Bachelor of Science degree in chemistry and applied mathematics from the University of Central Arkansas in 2004. She entered the chemistry program at Texas A&M University in August 2004 and graduated in May 2009.

Kristin Dooley may be reached at Chemistry Department, c/o Dr. Simon S. North, TAMU, College Station, TX, 77843-3255. Her email is kdooley@mail.chem.tamu.edu.